


MAX PLANCK INSTITUTE
FOR POLYMER RESEARCH

JOHANNES GUTENBERG
UNIVERSITÄT MAINZ

Polymer-Based Biomaterials with Specific Surface Features *for Antibiofouling, Blood-Repelling Dressing, and Nerve Tissue Engineering*

Dissertation

zur Erlangung des Grades
"Doktor der Naturwissenschaften"
im Promotionsfach Chemie

am Fachbereich Chemie, Pharmazie,
Geographie und Geowissenschaften
der Johannes Gutenberg-Universität Mainz

vorgelegt von

Lijun Ye
geboren in Lishui (China)

Mainz, 2021

Die vorliegende Arbeit wurde im Zeitraum von Juni 2017 bis Mai 2021 am Max-Planck-Institut für Polymerforschung in Mainz unter der Anleitung von Herrn Prof. Dr. [redacted], Herrn Dr. [redacted] und Herrn Prof. Dr. [redacted] angefertigt.

1. Berichterstatter: Prof. Dr. [redacted]
2. Berichterstatter: Prof. Dr. [redacted]
3. Berichterstatter: Prof. Dr. [redacted]

Tag der mündlichen Prüfung: 28.07.2021

Declaration

I hereby declare that I wrote the dissertation submitted without any unauthorized external assistance and used only sources acknowledged in the work. All textual passages which are appropriated verbatim or paraphrased from published and unpublished texts as well as all information obtained from oral sources are duly indicated and listed in accordance with bibliographical rules. In carrying out this research, I complied with the rules of standard scientific practice as formulated in the statutes of the Johannes Gutenberg University Mainz to ensure standard scientific practice.

…….

(Lijun Ye)

Abstract

In the biological and medical fields, surfaces/interfaces are critical for the application of materials in, *e.g.*, wound dressing, medical devices and implants, that interact with microorganisms, blood and proteins, cells and tissues. Therefore, the surface properties of biomaterials are of utmost importance and should be carefully designed for specific bio-/medical applications. This thesis describes the preparation and characterization of three different polymer-based biomaterials with specific surface features for potential applications in antibiofouling, blood repellency, and promoting neuronal differentiation.

First, I describe a new type of ionogel with a responsive, self-replenishing surface for combating biofouling. The ionogels are prepared by infiltrating solid/liquid mixtures of ionic liquids into a semicrystalline polymer skeleton. The specific surface features are derived from the spontaneous migration of the ionic liquid mixtures from the gel matrix, forming a surface layer. The surface layer serves as a 'firewall', killing bacteria on contact and inhibiting biofilm development at early stages. Upon heating, the solid surface of the ionogel transforms into the liquid-infused state, induced by the phase transition of the surface layer. The biofilms developed on the surface are easily removed. The antimicrobial efficiency is restored after biofilm detachment.

Next, I describe an elastic, superhydrophobic and photocatalytically active coating designed for wound dressing. The coating is prepared from the assembly of titanium dioxide (TiO_2) nanoparticles crosslinked with polydimethylsiloxane (PDMS). The PDMS/TiO_2-coated surfaces exhibit superior repellency to blood due to their superhydrophobicity. The elastic coatings show excellent stability under mechanical deformation. The superhydrophobicity of the surfaces can be restored by UV illumination even after fouled with the organic contaminant due to photocatalytic

activity. Besides, the PDMS/TiO_2 coatings enhance the antibacterial efficiency under UV light illumination.

Finally, I describe a novel and versatile method of preparing composites comprised of carbon nanotubes and poly(ethylene glycol) hydrogel for potential application in nerve tissue engineering. The effect of the composites on neuronal differentiation and network excitability is investigated. The differentiation and survival of neurons are promoted when cultured on the composites with the enhanced surface microstructures and protein adsorption. Furthermore, no significant change in the excitability of network activity is observed in primary cultures of hippocampal neurons. The results suggest that the composites are novel versatile substrates with several advantages for neuronal differentiation while maintaining homeostatic properties of neuronal network excitability.

The projects highlighted the significant role of surface characteristics of biomaterials that interact with biological systems.

Zusammenfassung

Im biologischen und medizinischen Bereich ist die Oberfläche/Grenzfläche kritisch für die Materialien, die beispielsweise in Wundauflagen, medizinischen Geräten und Implantaten angewendet werden und mit Mikroorganismen, Blut und Proteinen, Zellen und Geweben interagieren. Daher sind die Oberflächeneigenschaften von Biomaterialien von größter Bedeutung und sollten sorgfältig entworfen und auf bestimmte bio-/medizinische Anwendungen zugeschnitten werden. Diese Arbeit beschreibt die Herstellung und Charakterisierung von drei verschiedenen Biomaterialien auf Polymerbasis mit spezifischen Oberflächenmerkmalen für Antibiofouling, Blutabweisung und Förderung der neuronalen Differenzierung.

Zunächst beschreibe ich eine neue Art von Ionogelen mit einer sich selbst nachfüllenden Oberfläche zur Bekämpfung von Biofouling. Die Ionogele werden hergestellt, indem feste/flüssige Gemische ionischer Flüssigkeiten in ein teilkristallines Polymergerüst infiltriert werden. Die spezifischen Oberflächenmerkmale ergeben sich aus der spontanen Migration der ionischen Flüssigkeitsgemische aus der Gelmatrix, die eine Oberflächenschicht bilden. Die Oberflächenschicht dient als „Firewall“, tötet Bakterien bei Kontakt ab und hemmt frühzeitig die Entwicklung von Biofilmen. Beim Erhitzen wird die feste Oberfläche des Ionogels flüssig. Die auf der Oberfläche entwickelten Biofilme lassen sich leicht entfernen. Die antimikrobielle Wirksamkeit wird nach dem Ablösen die Biofilme wiederhergestellt.

Danach beschreibe ich eine elastische, superhydrophobe und photokatalytisch aktive Beschichtung für den Wundverband. Die Beschichtung wird aus dem Zusammenbau von Titandioxid (TiO_2)-Nanopartikeln hergestellt, die mit Polydimethylsiloxan (PDMS) vernetzt sind. Die PDMS/TiO_2-beschichteten Oberflächen weisen aufgrund ihrer Superhydrophobie Blut ab. Die elastischen

Beschichtungen zeigen eine ausgezeichnete Stabilität bei mechanischer Verformung. Die Superhydrophobie der Oberflächen kann durch UV-Beleuchtung auch nach Verschmutzung mit der organischen Verunreinigung aufgrund der photokatalytischen Aktivität wiederhergestellt werden. Außerdem verbessern die PDMS/TiO_2-Beschichtungen die antibakterielle Wirksamkeit unter UV-Lichtbeleuchtung.

Schließlich beschreibe ich eine neuartige und vielseitige Methode zur Herstellung von Verbundwerkstoffen aus Kohlenstoffnanoröhren und Polyethylenglykol-Hydrogel für eine mögliche Anwendung in der Nervengewebezüchtung. Der Einfluss der Verbundwerkstoffe auf die neuronale Differenzierung und die Erregbarkeit des Netzwerks wird untersucht. Die Differenzierung und das Überleben von Neuronen werden gefördert, wenn sie auf den Kompositen mit den verbesserten Oberflächenmikrostrukturen und Proteinadsorption kultiviert werden. Darüber hinaus wird in Primärkulturen von Hippocampus-Neuronen keine signifikante Änderung der Erregbarkeit der Netzwerkaktivität beobachtet. Die Ergebnisse legen nahe, dass die Verbundwerkstoffe neuartige vielseitige Substrate mit mehreren Vorteilen für die neuronale Differenzierung sind, während die homöostatischen Eigenschaften der Erregbarkeit des neuronalen Netzwerks erhalten bleiben.

Die Projekte hoben die bedeutende Rolle der Oberflächeneigenschaften von Biomaterialien hervor, die mit biologischen Systemen interagieren.

Contents

Chapter 1

Introduction

Polymers are natural or synthetic macromolecules composed of multiple repeating subunits.[1] The high molecular mass and tunable dispersity, and the possibility for complex molecular architectures provide unique physicochemical properties of polymers.[2-9] The range of polymers is vast, from synthetic plastics such as polyethylene used in everyday life to natural biopolymers such as DNA and proteins fundamental to biological structures and functions. Due to their broad spectrum of properties, polymers play essential and ubiquitous roles, from traditional household to complex electronics and advanced biomedical fields.[10-15]

Biomaterials usually containing multiple components have been often exploited as augmentations or replacements of a natural function, tissue, or even organs in medical applications.[16] Due to their tailorable structures and properties, polymers have been extensively adopted into biomaterials for applying in, *e.g.*, antibiofouling, drug delivery, wound healing, biosensors, and tissue engineering.[17-21] As interacting with biological systems, biomaterials are normally exposed to microorganisms, blood and proteins, cells and tissues. Thus, the surface properties are of utmost significance and should be carefully designed. This thesis focuses on preparing polymer-based biomaterials with specific surface characteristics for their potential applications in antibiofouling, wound dressing, and nerve tissue engineering, as discussed below.

Biofouling is the accumulation of microorganisms, or even small animals on surfaces, which poses risks of causing severe negative consequences to a wide variety of objects, *e.g.*, boat hulls and equipment, medical devices, distillation membranes, and underwater plants.[22, 23] Bacterial adhesion and biofilm formation on the surface are essential in many cases for the settling of microorganisms. To combat

biofouling, the surfaces have been engineered with microstructures and/or functionalized with specific moieties to inhibit biofilm development.[24-28] For instance, bifunctional surfaces modified with zwitterionic or responsive moieties were reported to switch surface properties, where bacteria can be killed on contact and then released by external stimuli, *i.e.*, changing temperature, pH, *etc*.[25, 26] However, non-specific adsorption and accumulation of proteins and surfactants secreted by microbes on the surface are not trivial, which leads to the irreversible loss of antimicrobial efficacy and the failure of long-term antibiofouling applications. Liquid-infused surfaces where the microstructures are impregnated with a liquid layer can resist biocontamination by minimizing the contact of the solid surface with microbes.[28] However, the depletion of the liquid layer on the surface results in the loss of antibiofouling function. It is still challenging to efficiently remove biofilms and restore antimicrobial functions of the surface after long-term exposure to microbes.

Wound dressing serves as a physical barrier preventing the human body from excessive blood loss and potential infections. The surface wettability of a wound dressing plays a vital role in stopping bleeding.[29-33] For instance, the cotton gauze is inherently superhydrophilic, making it extremely favorable for wetting and quickly absorb water from the blood to accelerate the coagulation process.[29, 32] In contrast, superhydrophobic surfaces can resist blood permeation due to the superior non-wetting features, helping reduce blood loss and bacteria adhesion.[30] Janus superhydrophobic/superhydrophilic fabrics serve as a combination, where the superhydrophilic side promotes blood coagulation by rapid water adsorption while the superhydrophobic backside prevents excessive blood loss.[29, 31] However, when the bleeding wound is normally treated with the superhydrophilic gauze, the adsorption of blood in gauze will form concrete clot-gauze composite, which makes it difficult to

replace and remove dressings without causing additional pain, secondary bleeding, and potential infection. On the other hand, the fragility of superhydrophobic structures makes them easily destroyed when the bleeding is usually treated with gauzes by mechanical pressure, producing free microparticles, which poses a risk of causing micro-thrombosis when the particles enter the vascular system.[34, 35]

Nerve tissue engineering refers to repairing nerve damage or promoting nerve regeneration by developing biocompatible artificial grafts or scaffolds.[36] Nerve guidance conduits (NGCs) normally with tubular structures are promising scaffold materials for repairing large nerve defects.[37, 38] NGCs can support bridging the gap of an injured nerve and serve as a protective microenvironment that is significant for regenerating axons and preventing scar invasion.[39] As a cell/tissue interfacing material, the surface characteristics of NGCs play a crucial role in promoting cell migration, survival, adhesion and differentiation. In addition to surface chemistry, stiffness and topography, the electrical conductivity of NGCs is often assumed as vital in stimulating neuronal develpments.[40, 41] For instance, polymer nanocomposites comprised of biocompatible hydrogels and carbon nanotubes (CNTs) and/or their analogs are reported to serve as potential NGCs promoting neuronal differentiation.[42, 43] Although CNTs (usually coated on substrates) have been reported to stimulate neuronal activity,[44, 45] whether and how it would work when CNTs are embedded in the composites remains elusive.

The past decades have seen intensive devotions to preparing biomaterials with specific surface characteristics and functions. Nevertheless, challenges and open questions have been emerging on the road to explore novel biomaterials. This thesis aims to tackle the challenges and the open questions mentioned above with new strategies to develop advanced functional biomaterials. Many current strategies for

antibiofouling suffer from the gradual loss of efficiency due to the accumulation of the secretions from microbes on the surface or the degradation/depletion of the surface. To attain renewable antibiofouling properties, a new type of responsive ionogel from polyvinylidene difluoride and organic salts integrating the antimicrobial property of the ionogel with the dynamic surface property of the liquid-infused surface has been developed (**Chapter 3**). The new strategy provides the chance to restore antimicrobial efficiency by on-demand activation of the solid surface into a liquid.

Wound dressings with superhydrophobic surfaces show great potential to reduce the formation of clot-gauze composites, thereby helping alleviate pains and reduce secondary bleeding during the removal/replacement of the old dressings. However, the poor mechanical properties of superhydrophobic surfaces pose risks to the blood circulation system. Therefore, a mechanically elastic superhydrophobic coating with photocatalytic activity based on biocompatible polydimethylsiloxane and titanium dioxide nanoparticles has been designed for wound dressings to attain robust blood repellency (**Chapter 4**). The assembly of photocatalytically active titanium dioxide nanoparticles with elastic polymers provides a path to develop wound dressing materials capable of reducing blood loss and potential infections.

The CNT-hydrogel composites have become of interest as electrically conductive scaffold materials in nerve tissue engineering. However, whether the CNTs embedded within the hydrogel matrix could affect neuronal differentiation and how they do so have remained elusive, as mentioned above. Therefore, the CNT-poly(ethylene glycol) hydrogel nanocomposites have been prepared in a new and versatile method without pre-functionalization of CNTs (**Chapter 5**). The effect of CNT-poly(ethylene glycol) hydrogel composites on neuronal developments has been systematically investigated. The results provide the new insight that electrical conductivity itself is not fundamental

for CNT-hydrogel composites as artificial nerve grafts. In the meantime, other physicochemical properties, such as surface topography, should also be considered to design functional scaffolds for nerve regeneration.

Chapter 2

Fundamentals & Methods

2.1 Wetting on Solid Surfaces

2.1.1 Classical Models

When putting a droplet on a solid surface, a three-phase contact line forms where the liquid-air interface meets the solid-liquid interface. The surface wettability is generally characterized by measuring the contact angle at the three-phase contact line (**Figure 2.1**a). For the surface that is perfectly flat, rigid and chemically homogeneous, the equilibrium contact angle (Θ) was defined by **Young's equation** as follows:[46]

$$\cos\Theta = \frac{\gamma_{SA} - \gamma_{SL}}{\gamma_{LA}}$$

Here, γ_{SA}, γ_{SL}, and γ_{LA} are the solid-air, solid-liquid, and liquid-air interfacial tensions. The Θ will increase when the surface becomes more repellent. For water (oil), the surface is generally termed hydrophilic (oleophilic) when Θ < 90°. On the contrast, the surface is termed hydrophobic (oleophobic).

The roughness plays an essential role in amplifying surface wettability.[47] The impact of surface roughness can be described by the **Wenzel model**,[48] and **Cassie-Baxter model**.[49] In the Wenzel state (**Figure 2.1**b), the liquid will penetrate into the space between the protrusions on the surface. In this state, the equilibrium contact angle (Θ_w) has been described as follows:[48]

$$\cos\Theta_w = r\cos\Theta$$

Here, Θ is Young's contact angle, and r is a roughness parameter from the total surface area divided by the projected area of the solid surface. For a simplified, rough surface with an array of square posts (**Figure 2.1**b), $r = 1 + 4dh/(d + w)^2$. In the

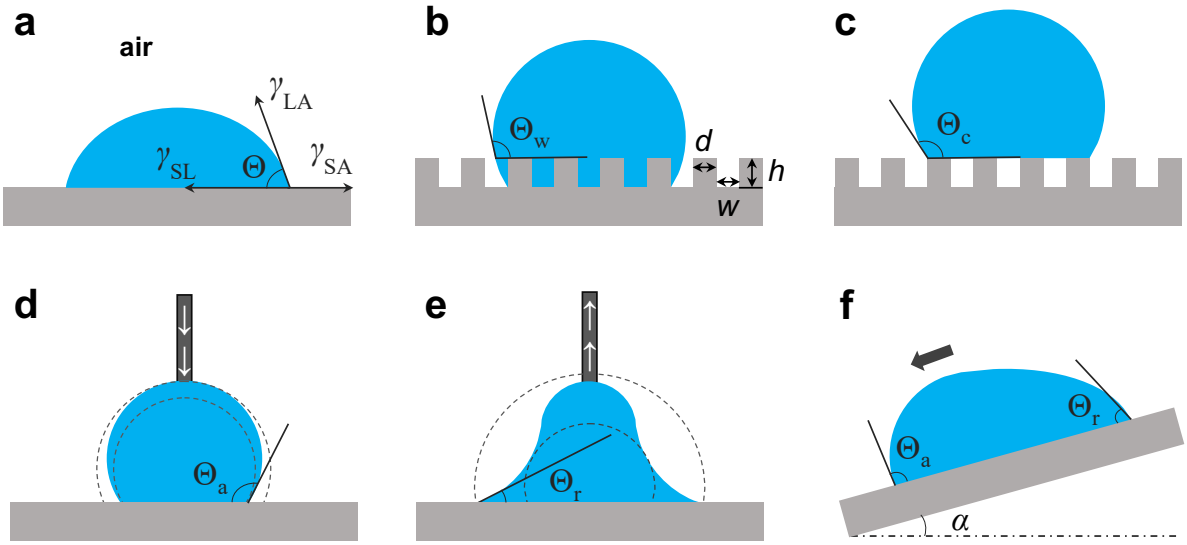

Figure 2.1 Schematic diagrams. a) The contact angles at the three-phase contact line on a flat surface, and on a rough (porous) surface with b) the Wenzel state, c) the Cassie-Baxter state. d) The advancing and e) receding contact angles when adding liquid to the droplet (or retracting liquid from the droplet) on the surface, and f) dynamic contact angles and sliding angle/rolling-off angle of a sliding droplet on a tilted surface.

Wenzel state, Θ_w will increase when $\Theta > 90°$ and decease when $\Theta < 90°$. Note that the Wenzel equation is reverted to Young's equation when $r = 1$, a sign of a surface with perfect flatness.

When the liquid does not penetrate the gap between the protrusions on the surface (**Figure 2.1**c), it results in a composite interface comprised of the liquid-air interface and the solid-liquid interface, termed Cassie-Baxter state. The Cassie-Boxer model was derived from Cassie's equation,[50] describing the wetting on a flat surface with chemical heterogeneity, by defining the contact angle between liquid (water) and air to be 180° for rough (porous) surfaces.[51] The equilibrium contact angle (Θ_c) in the Cassie-Baxter state has been described as follows:

$$\cos\Theta_c = \varphi_s(1 + \cos\Theta) - 1$$

Here, φ_s is the solid fraction of the projected area of the surface. $\varphi_s = d^2/(d + w)^2$ for a simplified rough surface. In the Cassie-Baxter state, Θ_c increases with increasing

the fraction of liquid-air interface ($1 - \varphi_s$). For an extremely tiny solid fraction ($\varphi_s \rightarrow 0$), Θ_c approaches 180°. The Cassie state with the significantly reduced contact line pinning is essential for attaining super repellent surfaces. However, the impalement transition to the Wenzel state from the Cassie-Baxter state may occur during droplet evaporation, impacting, *etc*.[52, 53]

2.1.2 Contact Angle Hysteresis

When the liquid is carefully added to the droplet (or withdrawn from the droplet) on a surface with a syringe (**Figure 2.1**d, e), the droplet increases (or decreases) in volume and contact angle while maintaining a constant contact area with the surface until the contact line begins to advance (recede).[54-57] The contact line advances (or recedes) with a constant contact angle, reflecting the surface characteristics such as surface roughness and chemical heterogeneity. The advancing (Θ_{ACA}) and receding (Θ_{RCA}) contact angles are normally measured during contact line moving. The Θ_{ACA} is defined as the maximum stable contact angle before the moving of the contact line and Θ_{RCA} is defined as the minimum stable contact angle.[56] Therefore, a static, metastable contact angle measured from a pinned contact line locates somewhere between Θ_{ACA} and Θ_{RCA}. The Θ_{ACA} is regarded as the reflection of surface wettability, and Θ_{RCA} serves as a characteristic of surface adhesion.[57] The difference between Θ_{ACA} and Θ_{RCA} is defined as contact angle hysteresis (Θ_{CAH}).[56] A droplet can simultaneously advance and recede on a tilted or moving surface (**Figure 2.1**f).[58, 59] In a sliding scenario, the tilting angle of the surface where the static droplet starts moving is termed sliding angle (or rolling-off angle, α), a characteristic of the low adhesion of the super repellent surfaces.[60, 61] The moving velocity of the contact line has been reported to affect the Θ_{ACA} and Θ_{RCA} of a moving droplet.[62]

2.2 Superhydrophobic Surfaces

Superhydrophobic surfaces are normally defined as a surface with an apparent water contact angle larger than 150°.[63, 64] Superhydrophobic surfaces with self-cleaning properties (characterized by low sliding angles or a low contact angle hysteresis) are fairly desirable for various applications, *e.g.*, microfluidics, solar energy panels, electronic devices, exterior architectural windows, *etc*.[65] The best known self-cleaning superhydrophobic surface is the lotus leaves. The lotus leaves show hierarchical surface structures with microscale protrusions covered by nanoscale crystalloids of epicuticular wax.[66] The combination of micro- and nanoscale roughness has been adopted in numerous studies for preparing superhydrophobic surfaces with self-cleaning properties.[67, 68]

2.2.1 Preparing of Superhydrophobic Surfaces

Various methods have been developed for preparing superhydrophobic surfaces in the past decades.[65] The micro- and/or nanostructures of superhydrophobic surfaces are normally regarded as vital in entrapping air beneath the water drops (the Cassie-Baxter state), resulting in large macroscopic contact angles with a low contact angle hysteresis.[69-71] Lithography is a versatile method for making superhydrophobic surfaces with patterned micro- and nanostructures.[72-75] Photolithography is the practice of transferring a geometric pattern by light from a photomask to the substrates coated with a photoresist. The micropatterned substrates can be further applied as a template creating inversed microstructures on other materials (known as soft photolithography[76]). *Öner et al*. prepared a series of superhydrophobic surfaces with patterned micropillars created by photolithography.[72] Electron-beam lithography (abbreviated as e-beam lithography), which applies focused electron beam to draw custom patterns on a substrate covered with an electron-sensitive material, has been

utilized as a maskless method to produce superhydrophobic surfaces where the well-defined microstructures are decorated with nanostructures.[74] Besides, laser has been applied in direct writing and interference patterning to make complex surface structures.[75] The silanization chemistry is normally combined with the micropatterned structures for attaining superhydrophobicity.[72, 74]

The etching techniques, including chemical etching, reactive ion and plasma etching, laser etching, *etc*., are straightforward and effective for creating random surface microstructures.[77-81] *Qian et al.* prepared a variety of superhydrophobic surfaces by introducing hierarchical structures on polycrystalline aluminum, copper and zinc using dislocation-selective chemical etching followed by silanization.[77] The etching is often combined with other techniques such as lithography, especially for producing complex surface microstructures.[72, 81, 82] *Liu et al*. fabricated doubly re-entrant micro-posts containing nanoscale vertical overhangs on silica surfaces by combining photolithography with several etching steps. The surfaces alone with the re-entrant structures exhibit super-repellent for liquids with low surface tension.[81]

Chemical vapor deposition (CVD) is a versatile method of preparing superhydrophobic surfaces with fractal-like structures.[83-87] The CVD method can be used for either producing rough surfaces or making a thin layer on a rough surface. *Artus et al*. reported a method of growing silicone nanofilaments (typically with a diameter of 50 nm) onto various substrates by the CVD method. The nanofilament-coated surfaces exhibit high water contact angles with a low sliding angle.[84] *Deng et al*. reported a method using candle soot as a template to produce fractal-like surface microstructures of silica by the CVD method.[86] Flame spraying deposition serves as a ultrafast and versatile CVD method to generate and deposit nanosized (less than 100 nm) metal and metal oxide particles, forming hierarchical superhydrophobic

nanotextures on large area substrates.[85, 87] Combining with surface fluorination, super-repellent surfaces with ultralow contact angle hysteresis for a liquid with very low surface tension can be attained.[87]

There are many other methods. *Erbil et al*. reported a simple and inexpensive way to produce isotactic polypropylene (*i*-PP) superhydrophobic coatings on various substrates by controlling the evaporation of the *i*-PP solution with the addition of nonsolvent. The highly porous superhydrophobic surfaces exhibit water contact angles up to 160°.[88] Besides, many other techniques, including sol-gel processing,[89] colloidal and layer-by-layer assembling,[90, 91] electrospinning,[92] and electrochemical processes[93] have been applied in preparing superhydrophobic surfaces.

2.2.2 Superhydrophobic Surfaces for Wound Dressing

Superhydrophobic surfaces are promising wound dressing materials helping reduce blood loss and bacteria adhesion due to their non-wetting features. Reduced bacteria adhesion has been reported on superhydrophobic surfaces, although it remains controversial.[24, 94-98] *Privett et al.* reported that the superhydrophobic coatings comprised of fluorinated silica can resist the adhesion of bacteria with highly pathogenic properties such as *S. aureus* and *P. aeruginosa*.[96] In contrast, *Fadeeva et al*. founded that the superhydrophobic titanium surface exhibits a dependence the bacterial resistance of on intrinsic bacterial properties. It is claimed that *S. aureus* is able to colonize on the superhydrophobic titanium surface, whereas no *P. aeruginosa* can attach the surfaces.[95] *Hwang et al.* suggested that the resistance to bacterial adhesion of superhydrophobic surfaces is short-lived, and the hierarchical surface microstructures even promote bacterial adhesion after losing the entrapped air.[98]

On the other hand, superhydrophobic surfaces exhibit superior resistance to the adhesion of proteins and platelets.[99-102] The platelet activation on the surface of

medical implants and blood-contacting medical devices pose the risks of causing thrombosis. *Sun et al.* reported that the superhydrophobic surfaces comprised of aligned carbon nanotube films modified with fluorinated poly(carbonate urethane) significantly suppress the adhesion and activation of platelets.[100] Moreover, the reduced blood adhesion resulted from the hierarchical superhydrophobic structures is fairly desirable for avoiding clot-gauze composites. Recently, *Li et al*. fabricated a hemostatic superhydrophobic surface with immobilized carbon nanofibers, promoting rapid clotting with minimal blood adhesion.[103]

The resistance of superhydrophobic surfaces to the adhesion of bacteria, blood and platelets significantly relies on the hierarchical surface microstructures. But the hierarchical structures of superhydrophobic surfaces are normally susceptible to damage under mechanical stresses. The break of surface microstructures leads to the failure of the non-wetting properties of superhydrophobic surfaces. The unexpected leakage of micro- and/or nanoparticles from the blood-contacting surface poses the risks of causing thrombosis and activating inflammation and immune responses.[104, 105] In addition to the design of surface microstructures, the cytotoxicity of substances used in preparation and/or surface modification should be carefully considered. Although it is reported that the perfluorocarbons often used in surface modifications can be phagocytosed by macrophages without impacting the metabolism and be expelled out by exhaling, the cytotoxicity remains controversial.[106, 107]

2.3 Liquid-Infused Surfaces

Liquid-infused surfaces are (porous) microstructured substrates impregnated with a liquid (lubricant).[108-110] The capillary wicking causes the spreading of lubricants on the substrates, forming a liquid layer against the sticking and spreading of most immiscible

liquids. A natural liquid-infused surface is observed in the Nepenthes pitcher plant. The peristome of pitcher plants entraps a thin layer of water by the microstructures, creating a slippery surface that is difficult for insects to stay.[111, 112] In 2011, *Wong et al*. reported the first example of liquid-infused surface with omniphobic properties by perfusing nanofibrous Teflon membranes with Fluorinert (FC70), termed slippery liquid-infused porous surfaces (SLIPSs).[108] The general criteria for successful preparing of liquid-infused surfaces have been outlined by *Wong et al.*,[108] and *Lafuma et al.*:[109] 1) the lubricant must be immiscible with the probe liquids, 2) the lubricant must wick into the solid substrates, and 3) the solid substrates must preferentially favor the wetting of the lubricant rather than the probe liquid.

2.3.1 Wetting on Liquid-Infused Surfaces

When putting a droplet on the liquid-infused surface, the situation of this four-phase system becomes more complex than the traditional three-phase system. The cloaking layer and the wetting ridge are two key features identified by *Smith et al*., when a droplet comes into contact with the liquid-infused surface.[113] The wetting ridge results from the balance of the surface tension at the contact line, where the out-of-plane component pulled the lubricant up, forming an annular ridge around the droplet (**Figure 2.2**a, c). The wetting ridge may end in a line, where the droplet, lubricant and air meet, forming a liquid three-phase contact line.[114] *Semprebon et al.* showed that the apparent contact angles, as well as contact angle hysteresis, are not only defined by material properties but also related to the relative size of the droplet and the wetting ridge (**Figure 2.2**c).[115]

The cloaking layer is dependent of the spreading parameter of the lubricant on the droplet, $S = \gamma_{DA} - \gamma_{LA} - \gamma_{DL}$, where γ_{DA}, γ_{LA} and γ_{DL} are the droplet-air, lubricant-air, and droplet-lubricant interfacial tensions. When $S > 0$, a thin lubricant layer

spontaneously cloak the droplet and reduce the overall energy of the system (**Figure 2.2**b, d).[113] *Schellenberger et al*. have directly observed the cloaking layer using confocal microscopy. The thickness of the cloaking layer is estimated around 20 nm for water on Fluorinert (FC70)-infused surfaces.[114]

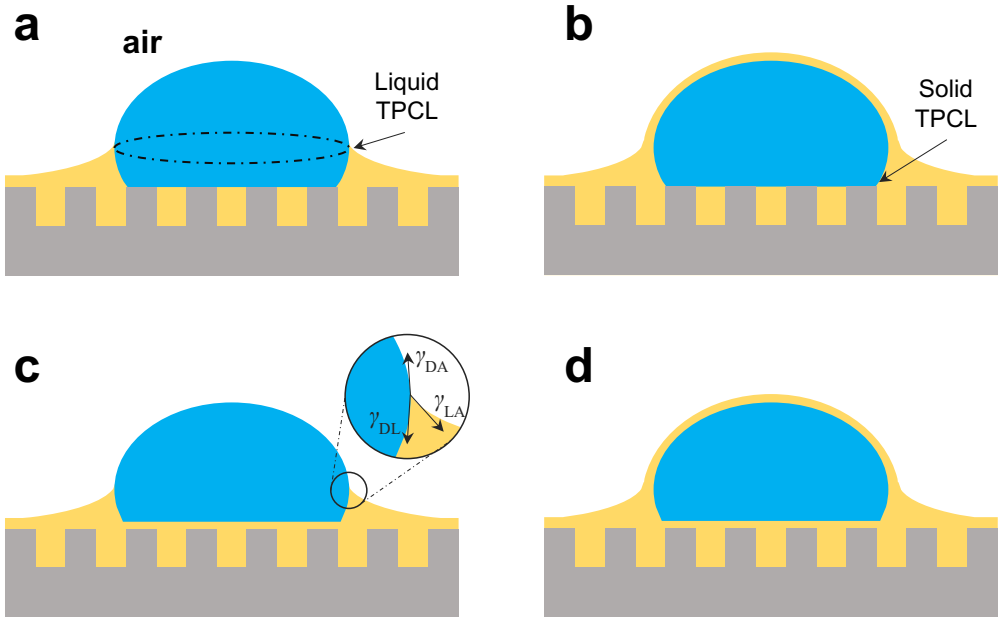

Figure 2.2 Schematic diagrams of wetting configurations on a liquid-infused surface. a, b) The droplet is sitting on the top of microstructures and an annular wetting ridge is formed around the droplet. c, d) The droplet is floating on the top of the lubricant. The cloaking layer of lubricant can form (b and d), or does not form (a and c), depending on the spread parameter of lubricant on the droplet. The droplets on the liquid-infused surface can have two (a), one (b and c), or zero (d) three phase contact lines (TPLC).

When interacting with the liquid-infused surface, the droplet can penetrate into microstructures and replace the lubricant, or sink and contact with the top of microstructures (**Figure 2.2**a, b), or float on the top of the lubricant layer (**Figure 2.2**c, d).[113, 114] *Smith et al.* theoretically described a comprehensive thermodynamic framework for predicting twelve different configurations with the interface tension, roughness and solid fraction.[113] The lubricant will be impaled by the droplet when the spreading parameter of the lubricant on the solid surface in the present of the droplet,

$S_{LS(D)} < -\gamma_{DL}(r-1)/(r-\varphi)$, where γ_{DL} is the interface tension between droplet and lubricant, r is the parameter of roughness from the Wenzel model, and φ is the solid fraction defined by the Cassie-Baxter model. In this case, the contact line is pinned on the solid surface, making the droplet difficult to slide or roll-off from the surface. When $-\gamma_{DL}(r-1)/(r-\varphi) < S_{LS(D)} < 0$, The solid substrate is favorable for the wetting of the lubricant rather than the droplet. The microstructures are impregnated with emergent features (**Figure 2.2**a, b). In this case, the droplet sinks into the oil and rests on the on top of the protrusions, forming the solid three-phase contact line.[114] Therefore, the rolling-off/sliding angles are dependent of φ, similar to the Cassie-Baxter state on the superhydrophobic surface. The droplet will sit on the top of the lubricant layer only when $S_{LS(D)} \geq 0$. The microstructures are impregnated with submerged features (**Figure 2.2**c, d). In this case, the droplet mobility is significantly enhanced, characterized by extremely low rolling-off/sliding angles.[113, 116]

2.3.2 Preparing of Liquid-Infused Surfaces

The past decade has seen rapid developments in the design and preparation of liquid-infused surfaces.[65, 110] Unlike entrapping air plastron in superhydrophobic structures, liquid-infused surfaces achieve their super liquid repellency by a liquid layer perfused within the solid substrates. Thus, the compatibility between the substrates and the lubricant is of utmost significance for producing liquid-infused surfaces,[117] while a textured surface is favorable for promoting lubricant retention.[118] *Leslie et al.* fabricated a liquid-infused flat surface where the thin liquid film of medical-grade perfluorodecalin was maintained by a flexible molecular perfluorocarbon layer covalently grafted on the smooth surface.[117] Nevertheless, SLIPSs (also termed liquid-infused textured surfaces) where the lubricant is infused into microstructures of the solid substrates are the most popular form of liquid-infused surfaces.[110, 119]

Kim et al. prepared an icephobic surface by impregnating aluminum fins and sheets with a fluorinated oil. The aluminum surface was modified by electrochemical deposition of polypyrrole to create microstructures and fluorinated with a CVD process to improve the affinity between the lubricant and the surface.[120] *Sunny et al*. prepared a liquid-infused surface by infusing a fluorinated oil into a rough surface derived from the layer-by-layer assembly.[121] *Dong et al*. fabricated doubly re-entrant micropillars, the top of which was decorated with nanostructures, by 3D direct laser writing.[122] The surface showed excellent omniphobic properties with large contact angles (> 150°) and significantly reduced adhesion when the nanostructures on pillars were infused with a lubricant layer.

The micro- and/or nanostructures of superhydrophobic surfaces can be easily adopted into liquid-infused surfaces with the careful design of the lubricant-substrate combinations.[65, 123] Surface modification serves as a versatile strategy against the mismatch of inherent properties between the lubricant and the substrate.[65, 120, 121] The lubricants used in practice can be divided into 1) fluorinated lubricants including Krytox oils, Fluorinert (FC70), perfluorodecalin, and ionic liquids, and 2) nonfluorinated lubricants, including silicone oils, hydrocarbon oils, *etc*.[110, 119] The proper choice of lubricant for different substrates is the most essential when designing a liquid-infused surface. *Wong et al*. described a stable infused state by interfacial energy. They proposed two conditions for ensuring the wetting of the lubricant on the solid substrates is energetically favorable than the probe liquid.[108]

The thermodynamic framework (proposed by *Smith et al.*) describes a theoretical comprehensive guidance for designing liquid-infused surfaces by interfacial energy, roughness and sold fraction.[113] However, this thermodynamic framework fails to explain some wetting phenomena observed on liquid-infused surfaces.[124, 125] *Preston*

et al. proposed a model for predicting lubricant-substrate combinations with 90% accuracy. Based on their model, they designed a liquid-infused surface using unmodified high-surface-energy solids and polar lubricants for repelling discrete droplets of butane ($\gamma \approx 13$ mN m^{-1}).[126]

2.3.3 Liquid-Infused Surfaces for Antibiofouling

Liquid-infused surfaces have been applied in marine and medical fields to improve material functionality and lifespan by reducing biofouling.[127-129] *Epstein et al*. reported that the porous polytetrafluoroethylene substrate infused with a perfluorinated lubricant resists 96 − 99% of bacterial adhesion even after 7 days, achieving a significantly higher efficiency than the polyethylene glycol-modified surfaces.[28] *Xiao et al.* reported that the fluorocarbon-infused microporous substates of butyl methacrylate-ethylene dimethacrylate can prevent the adhesion of algae and barnacle.[130] *Leslie et al.* reported that a flat surface impregnated with a liquid layer is capable of repelling full blood and helping reduce platelet adsorption.[117] *Sunny et al.* reported that the endoscope lens modified with a transparent, liquid-infused coating can reduce biofouling against vision loss even after more than 100 repeated cycles of submersions in blood and mucus.[131] Recently, *Amini et al*. reported that the polydimethylsiloxane network infused with silicone oil can effectively prevent mussel adhesion under seawater.[132]

Liquid-infused surfaces are often advocated to have more robust super liquid-repellency, essential for reducing fouling by bacteria, blood, algae, *etc*., than superhydrophobic surfaces. The lubricant infused within the microstructures appears to be more stable than air plastron, especially under the conditions with high temperatures or pressures. However, the depletion of lubricant by drainage and/or evaporation is not negligible.[133-136] Self-lubricating organogels where the lubricant is

dispersed or adsorbed within a polymer network and spontaneously released to the surface have been developed against the depletion of the lubricant.[137-141] *Cui et al.* reported a supramolecular polymer gel with self-lubricating liquid-infused surface.[140] The self-replenishing properties are realized by dynamic exchange of the liquid between the surface and gel matrix. Nevertheless, it is still challenging to have active control over the depletion of lubricant.

2.4 Ionogels

Ionogels, also termed ion gels or ionic liquid gels, are composite materials comprised of ionic liquids immobilized by an inorganic or a polymer matrix.[142-144]

2.4.1 Ionic Liquids

Ionic liquids refer to organic salts with a low melting temperature below 100 °C, which are composed of organic cations and inorganic/organic anions.[145-148] Typical cations include quaternary ammonium, imidazolium, pyrrolidinium cations, *etc.*; the common anions include bromide, chloride, tetrafluoroborate, trifluoromethane sulfonate, hexafluorophosphate (PF_6), bis(trifluoromethyl sulfonyl)imide (NTf_2), *etc*.[147, 149] Ionic liquids are known as 'green solvents' because of their negligible vapor pressure, nonflammability, and tunable physicochemical properties.[146] therefore, ionic liquids are widely applied as the media (or catalysts) for chemical reactions and biomass processing,[150-153] extracting agents for pharmaceutical, nutritional and cosmetic applications,[154, 155] and electrolytes for electrochemical processes and devices.[149, 156] Furthermore, ionic liquid-grafted surfaces and poly(ionic liquids) are reported to have superior antimicrobial efficiency.[157-159] Besides, ionic liquids are proved as a promising medium for the exfoliation and dispersion of carbon nanomaterials, *e.g.*, carbon nanotubes (CNTs), graphene, *etc*.[160-164]

2.4.2 Preparation of Ionogels

Maintaining high ionic conductivity in a solid yet flexible state, ionogels have gained much attention for various applications, *e.g.*, membranes for gas separations, solid-state electrolytes for electrochemical devices, *etc*.[143, 165] Polymer-based ionogels can be synthesized from the in situ polymerization of monomers and crosslinkers (or crosslinking of polymer chains) in ionic liquids.[166, 167] Supramolecular ionogels with dynamic crosslinks, *e.g.*, hydrogen bonding, host-guest interaction, metal-ligand coordination *etc*., have attracted lots of interest.[168-172] *Sinawang et al*. reported a type of supramolecular ionogels by polymerization of host-guest complex comprised of peracetylated 2-ethyl-2-adamantane and γ-cyclodextrin in acrylate followed by impregnation of 1-ethyl-3-methylimidazolium bis(trifluoromethyl sulfonyl)imide ($[C_2C_1im][NTf_2]$).[168]

On the other hand, the self-assembly of ABA or ABC triblock copolymers where the A (and C) and B segments are respectively insoluble and soluble in an ionic liquid serves as a versatile method for preparing physically crosslinked ionogels.[173-175] *He et al*. prepared such ionogels from the self-assembly of poly(styrene-b-ethylene oxide-b-styrene) in $[C_4C_1im][PF_6]$ with the weight fraction of the copolymer as low as 5 %.[173] Besides, some (hetero)polymers where the segments undergo microphase separation in an ionic liquid can be used for preparing ionogels.[176-178]

In addition to the polymer matrix, ionogels can be prepared by impregnating ionic liquids into inorganic networks by sol-gel reactions of metal alkoxides,[142, 179] or colloidal assembly of nanoparticles.[180, 181] Colloid gels and glasses (or even colloid crystals[182]) can be attained by the colloidal assembly of nanoparticles in ionic liquids, depending on the interparticle interactions (attractive vs. repulsive forces).[183, 184] *Ueno et al*. reported that the gelation of $[C_4C_1im][NTf_2]$ is realized by adding ≥ 2 wt% (1.5

vol%) of fumed silica (with radius of ~ 6 nm).[183] A higher concentration of nanoparticles is required for preparing colloidal glass. The concentration of poly(methyl methacrylate)-grafted silica nanoparticles (M_n = 132 kDa) required for the quasi-solidification was 6 wt% (~ 70 − 74 vol%).[184]

2.5 Nanocomposite Hydrogels

2.5.1 Hydrogels

Hydrogels are a three-dimensional, physically or chemically crosslinked polymer network containing a large amount of water.[185] Due to their good biocompatibility and tunable physicochemical properties, including viscoelasticity, stiffness, permeability, hydrophilicity, *etc*., hydrogels are particularly promising biomaterials for applications in drug delivery, wound healing, biosensing, bioimaging, and tissue engineering, *etc*.[186-189] Hydrogels can be prepared either from natural polymers, *e.g*., agarose, collagen, alginate, *etc*., or synthetic polymers and their derivatives, *e.g*., poly(hydroxyethyl methacrylate), poly(ethylene glycol), polyacrylamide (PAA), poly(vinyl alcohol) (PVA), *etc*.[190, 191] Compared to natural polymers, synthetic polymers have their advantages of active control over the mesh size, architecture, properties and functionality of hydrogels.[188, 192]

A typical class of hydrogels is prepared by cross-linking hydrophilic polymer chains or polymerization of water-soluble monomers with crosslinkers.[190] In addition to chemical crosslinks, supramolecular interactions have been adopted as dynamic crosslinks to prepare hydrogels with self-healing properties.[187-189] Alternatively, physical hydrogels can be prepared from the self-assembly of ABA or ABC triblock copolymers with hydrophilic midblocks and hydrophobic end blocks, where the hydrophobic micelles serve as crosslinks.[193-195] Furthermore, polymer crystallites can

work as the physical crosslink.[196-200] Physical PVA hydrogels can be prepared from the solution by freeze-thaw cyclic processing, and the PVA crystallites can be arranged by combing with mechanical training.[196, 200]

2.5.2 Preparation of Nanocomposite Hydrogels

The combination of polymer hydrogels with nanoparticles (NPs), including metals, metal oxides, polymeric moieties, *etc.*, gives the composites synergistically improved physical, chemical, electrical, and biological properties.[201-204] Various methods have been reported to incorporate NPs into the bulk hydrogel networks. The simplest way to prepare nanocomposite hydrogels is to incorporate NPs during hydrogel formation. The nanocomposite hydrogels with well-dispersed NPs can be prepared from crosslinking polymer chains, or polymerization of monomers with crosslinkers, in particle suspensions.[201] Alternatively, nanocomposite hydrogels can be prepared by the incorporation of NPs precursors during hydrogel formation.[205-209] The NPs are formed within the hydrogel matrix afterward. A typical example is the hydrogel network from free-radical crosslinking copolymerization of N-isopropylacrylamide and comonomers containing thiol groups allowing to form complexes with Au^{3+} ions.[205] The Au NPs are then synthesized within the hydrogel matrix by chemical reduction.

On the other hand, NPs have been adopted as crosslinkers for hydrogel network formation. The NPs can be turned into crosslinkers after modification with the reactive groups.[210, 211] Moreover, the reversible Au-thiol interaction makes Au NPs multivalent crosslinkers for preparing dynamic NP-hydrogel composites.[212] In addition, the adsorption (self-assembly) of polymer chains onto the surface of NPs make them promising physical crosslinkers.[213-218] *Wang et al.* developed a nanocomposite hydrogel by means of the supramolecular interactions between clay nanosheets and dendritic polymers.[215] Furthermore, a ‘breathing in’ method has been developed for

incorporating NPs after hydrogel formation.[219-221] *Yissar et al.* prepared Au NP-PAA hydrogel composites by repeated cycling of collapsing the hydrogel in acetone and swelling in aqueous suspension of gold nanoparticles.[219]

2.5.3 Nanocomposite Hydrogels for Nerve Tissue Engineering

Due to the electrical properties of neural cells and their positive regenerative response to electrical stimulation, electrically conductive scaffolds that mimic electroactive tissue have attracted rapid attention in nerve tissue engineering.[40, 41, 222] Nanocomposite hydrogels embedded with electrically conductive NPs, *e.g.*, CNTs, graphene, reduced graphene oxides (rGO), *etc*., have been reported as potential materials promoting nerve regeneration after injuries. *Cho et al*. reported that the CNT-collagen composites facilitate the neurite extension of pheochromocytoma (PC12) cells with the significantly improved formation of micro-spikes and filopodia at growth cones under exogeneous electrical stimulation.[223] The enhanced neurite growth and neurite orientation of PC12 cells along the exogenous electrical fields have been observed in some other electroactive nanocomposite hydrogels.[224-227] On the other hand*, Lee et al*. reported the enhanced expression of neural markers and secretion of neurotrophic factors for mesenchymal stem cells cultured within a 3D CNT-collagen hydrogel matrix without electrical stimulation.[228] Similar results have been reported in induced pluripotent stem cells cultured on the silk fibroin-graphene composite films by *Niu et al*.[229] Furthermore, *Shin et al.* reported that the expression of calcium channel was upregulated in human neural stem/progenitor cells differentiated within 3D hyaluronic acid hydrogels dopped with CNTs and polypyrrole.[230]

Recently, increasing number of reports claimed that the differentiation of PC12 cells and dorsal root ganglia cells, and proliferation of Schwann cells, on the electroactive nanocomposite hydrogels containing CNTs and their analogs are

significantly enhanced without electrical stimulation.[42, 43, 231-233] The electrical conductivity of these nanocomposite hydrogels is often emphasized as a vital cue stimulating neuronal differentiation. *Liu et al*. prepared an electrically conductive oligo(poly(ethylene glycol) fumarate) hydrogel by introducing positive surface charges together with embedding CNTs and rGO.[42] It is claimed that the combination of surface charges and conductive fillers synergistically improves the cellular behaviors and activity including intercellular communication. Although CNTs and graphene (usually coated on substrates) are reported to stimulate neuronal electrical activity,[44, 45, 234] it is unclear how CNTs (and graphene) would work when embedded within the hydrogel matrix. Moreover, the incorporation of conductive NPs normally contributes not only to the enhanced electrical conductivity of nanocomposite hydrogels, but also to the increased surface chemistry, roughness, and mechanics (stiffness, viscoelasticity), *etc*. It is not easy to distinguish the role in stimulating neuronal differentiation and activity between electrical conductivity and other external cues.

2.6 Confocal Microscopy

Confocal microscopy, frequently referred to confocal laser scanning microscopy (CLSM), has emerged as one of the most important techniques of fluorescence imaging in recent decades and become an indispensable tool in scientific research. The basic concept of CLSM was initiated by *Minsky* in the 1950s, for overcoming the limitations of the conventional widefield epifluorescence microscopy.[235] The most important feature of CLSM is optical sectioning capable of capturing multiple 2D images at different depths within a thick specimen and enabling the reconstruction of 3D structures of the specimen.[236]

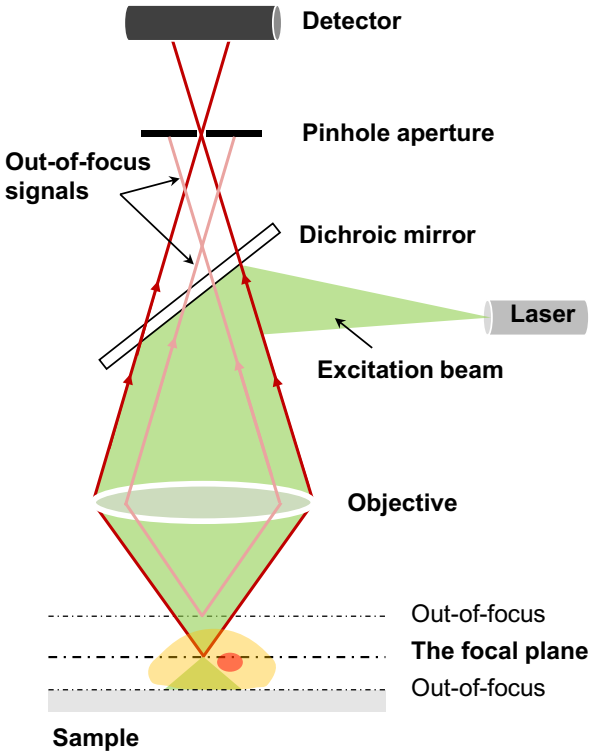

Figure 2.3 Schematic illustration of confocal laser scanning microscopy. For light illumination (excitation), a laser beam is reflected by a dichroic mirror and focused on the studied specimen by an objective lens. The excited fluorescence signals are collected through the same objective lens and directed to a photodetector after passing the dichroic mirror. A pinhole is placed in front of the detector to block the out-of-focus signals. By scanning the focus across the specimen, 2D and 3D images are acquired.

In a widefield epifluorescence microscopy, the specimen is illuminated evenly with a light from a light source. The problem is that the emitted background fluorescence above and below the focal plane will severely obscure the information from the focal plane. In contrast, the CLSM images are captured by a pointwise scanning under localized laser excitation. The use of a pinhole aligned in an optically conjugate plane in front of the detector permits spatial fluorescence filtering to eliminate the out-of-focus signals during imaging (**Figure 2.3**).[237] Only the light emitted very close to the focal spot are detected. Therefore, the optical resolution and contrast of an image, particularly in the axial (the sample depth) direction, are improved compared to the widefield fluorescence microscopy. The depth of the in-focus area in the specimen is

defined by the size of the pinhole – the smaller the pinhole, the narrower the depth of the in-focus area. However, a decrease of pinhole size might decrease signal-to-noise ratio due to the greatly reduced amount of light.[238]

The CLSM, as a fluorescence microscopy method, is essentially based on using of fluorophores for sample labeling to attain an image. There are several techniques for sample labeling. Immunofluorescence is a versatile technique for visualizing a protein of interest in the cellular context. It is based on staining cells with (primary) antibodies against a target protein, which are used together with fluorophore-conjugated secondary antibodies or directly conjugated with a fluorophore. Immunofluorescence has been used in this thesis (**Chapter 5**) for cell staining. Gene transcription serves as versatile technique to incorporate fluorescence proteins into cells. It is based on the process of copying a segment of DNA into a messenger RNA (mRNA) capable of encoding proteins. The mRNA after transcription is transported to the ribosome and directs protein synthesis with the help of transfer RNA. The green fluorescent proteins on the membrane of *E. coli* (**Chapter 3 & 4**) and neurons (**Chapter 5**) are incorporated by gene transcription.

Nowadays, CLSM has been widely used in many disciplines, not only in biology and medicine but in chemistry, physics, and material sciences. Besides, CLSM has been combined with other techniques, such as fluorescence correlation spectroscopy.[239]

2.7 Atomic Force Microscopy

Atomic force microscopy (AFM) is an advanced technique of scanning probe microscopy for investigating surface properties of materials with a resolution of subnanometer.[240] The information is collected by a mechanical probe mounted at the

front of a cantilever with a raster scanning motion close to the surface. The interaction between the specimen and the probe tip causes the cantilever to deflect. A laser beam impinging on the backside of the cantilever and reflected towards a position-sensitive photodetector is exploited to monitor the deflection of the cantilever (**Figure 2.4**).[241] The feedback system adjusts the distance between the specimen and the probe tip to keep a constant deflection of the cantilever as it moves over the specimen.

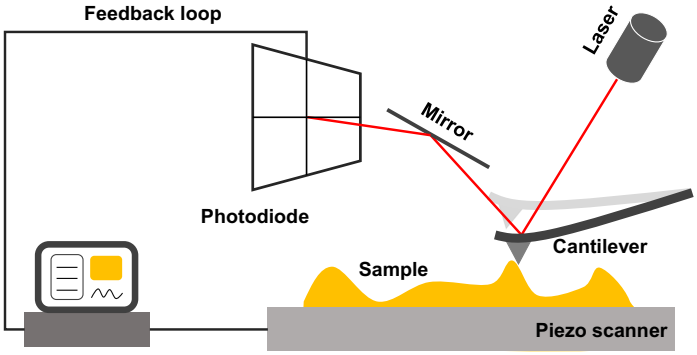

Figure 2.4 Schematic illustration of atomic force microscopy. The cantilever with a probe tip at the front scans in a raster motion over the surface. The deflection of the cantilever is used as the feedback signal, which is monitored by a laser beam reflected from the cantilever towards the position-sensitive photodetector. The feedback system keeps the deflection (oscillation amplitude or frequency in dynamic mode) of the cantilever constant.

The AFM can operate either in static or dynamic modes.[240] The static mode is also termed the **contact mode**, where the probe tip in contact with the specimen during imaging. The interaction forces between the specimen and the tip in the contact mode are repulsive and drive the cantilever to bend. The force (deflection) is used as the feedback signals. Therefore, the feedback system acts to maintain a constant deflection of the cantilever by adjusting the distance (force) between the specimen and the probe tip. As the probe tip contacts the specimen, the lateral forces can also drive the cantilever to torsion. The torsion can be monitored in the lateral force mode, providing information on the friction (or adhesion) of the surface.

In contrast, the cantilever in the dynamic mode, including the **non-contact** and the **tapping** mode, is vibrated close to its resonant frequency.[240] The amplitude-modulation (AM) and frequency-modulation (FM) are two main approaches in the dynamic operation mode. In the AM approach, the oscillation amplitude and phase shift are used as feedback signals, while the oscillation frequency is tracked in the FM approach. The oscillating cantilever is brought close to the specimen without 'touching' the surface in the non-contact mode. The interactions between the specimen and the probe tip are attractive forces, which will disturb the oscillation of the cantilever by decreasing the oscillating frequency and amplitude. The feedback system acts to keep the oscillation amplitude (AM) or frequency (FM) of the cantilever constant. In the tapping mode, or the intermittent-contact mode, the oscillation amplitude of the cantilever is typical higher than that in the non-contact mode. It permits the probe tip to gently tap the specimen in a short duration. The interactions between the specimen and the probe tip involve both attractive and repulsive forces.

The **peak force tapping mode** is a new intermittent-contact method.[242] The probe tip (non-vibrated) periodically taps the sample, and the interaction force is directly measured by the deflection of the cantilever. The feedback system keeps a constant peak force (down to 10 pN), which is significantly lower than that is typically used in tapping mode (~ 1 nN). The precise control of the interaction force can preserve both the tip and the specimen from mechanical damage. The peak force tapping mode is particularly suitable for the soft and sticky samples or those that are brittle or loosely bonded to a substrate. In **Chapter 5**, the peak force tapping mode has been applied to capture the surface morphology of hydrogels under water.

The AFM have been widely applied in physical, biological and materials science, not only in mapping of surface topography but in quantitative analysis of mechanical, chemical, and biological interactions.

2.8 Dynamic Mechanical Analysis

Dynamic mechanical analysis (DMA), also termed dynamic thermomechanical analysis (DTMA), mainly refers to the technique to study the viscoelastic properties of materials by applying periodical stress or strain (usually in sinusoidal form) to the test samples and measuring the response of strain or stress.[243] The frequency of the applying stress (or strain) and/or temperature can be programmed for different measurements. Note that DMA can also refer to torsional braid analysis that measures the decay of oscillations (controlled by natural damping) of a suspending, swinging sample (will not be discussed in this section).[243]

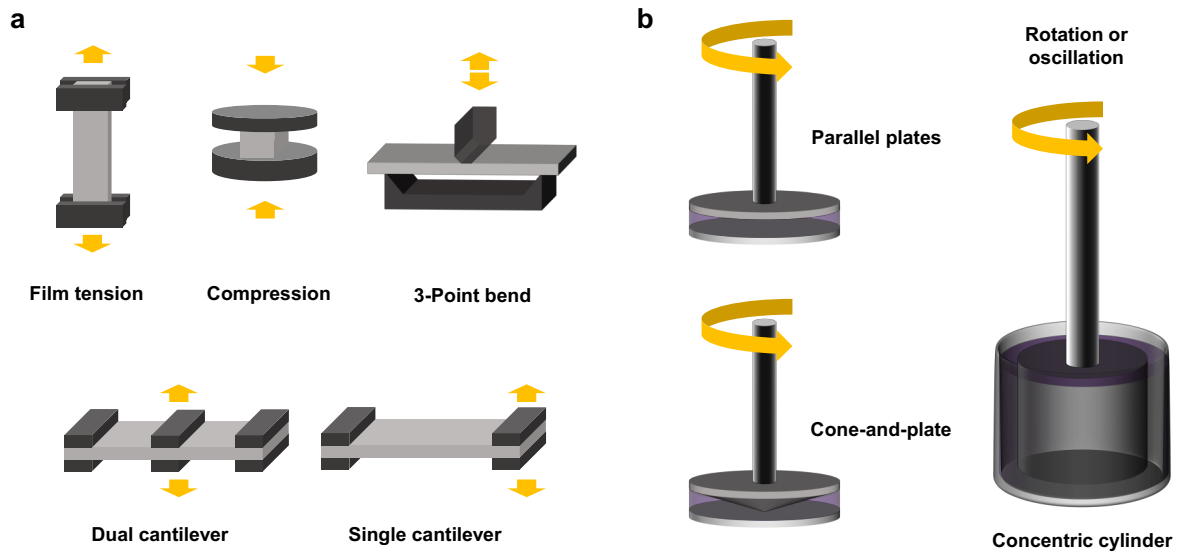

Figure 2.5 Schematic illustration of geometries of the a) axial mode and b) torsional mode for the DMA measurements.

The stress (or strain) can be applied in axial or torsional mode during the DMA measurements in practice (**Figure 2.5**). The instruments based on the axial mode

(frequently termed **dynamic mechanical analyzer**) are usually used for solid and semisolid materials. The test samples can be stretched, compressed, or bent by choosing different fixtures with specific geometries such as film tension, compression, 3-point bending, and dual-/single cantilever (**Figure 2.5**a). The instruments based on the torsional mode (mostly termed **rotational rheometer**) are particularly suitable for liquids, soft gels, and melts. The test samples can be rotationally sheared with a controlled shear stress (or shear rate, namely rotational tests), or oscillated with a controlled frequency of shear strain (in sinusoidal form, namely oscillation tests). The rotational test is used for characterizing the viscous behavior of the material, while the oscillation test characterizes the viscoelastic behavior. The measuring geometries can be parallel plates, cone-and-plate, concentric cylinders, or other complex geometries (**Figure 2.5**b). The rotational rheometer has been used in this thesis to characterize the phase transition of ionogels (**Chapter 3**) and the percolation network of CNTs in nanocomposite hydrogels (**Chapter 5**) with the oscillation test.

The oscillation test can be performed at a constant frequency of shear strain (or shear stress) by varying temperature (namely temperature sweep). It can also be performed at a constant temperature by varying frequency (namely frequency sweep). Before the measurements, an amplitude sweep (or strain sweep) by gradually increasing the amplitude of oscillations (of shear strain or stress) to define the linear viscoelastic regime is necessary, ensuring that the structures of the material will not be destroyed by the oscillation test. Complex shear modulus (G^*) and viscosity (η^*) obtained from the oscillation test are two important parameters that describe the viscoelastic properties of the materials.

The complex shear modulus ($G^* = G' + iG''$) of the test samples can be obtained from the shear stress (τ) divided by the shear strain (γ), with two components as

characteristics of energy storage for the elastic portion (storage modulus, *G*') and energy dissipation for the viscous portion (loss modulus, *G*''). *G*' and *G*'' have been described as,[244]

$$G' = \frac{\tau_A}{\gamma_A}\cos\delta,\ G'' = \frac{\tau_A}{\gamma_A}\sin\delta$$

Here, τ_A, γ_A are the amplitude of shear stress and shear strain, and δ is the phase lag of oscillations between shear strain and shear stress. The tan δ is termed loss factor or damping factor. δ = 0 for an ideally elastic material (*i.e*., Hookean solid) with the stress proportional to the strain, whereas $\delta = \pi/2$ for a purely viscous material (*i.e.,* Newtonian fluid) with the stress proportional to the strain rate. For the viscoelastic materials, δ locates somewhere in between ($0 < \delta < \pi/2$). Complex viscosity ($\eta^* = \eta' + i\eta''$) of the test samples is given by,[244]

$$\eta^* = \frac{G^*}{i\,\omega}$$

Hence,

$$\eta' = \frac{G''}{\omega},\ \eta'' = \frac{G'}{\omega}$$

Here, ω is the angular frequency of the shear strain (or shear stress). These parameters are widely used to characterize the material properties such as glass transition, phase transition, structural heterogeneity, and structural evolution, *etc*.

Chapter 3

Phase Transition-Activated Switching of Surface Properties for Combating Biofouling§

Biofouling has emerged as an issue of great concern in various areas while achieving long-term stability of antibiofouling remains challenging. In this chapter, the synthesis of ionogels with a responsive, self-replenishing surface for combating biofouling is described. Ionogels are prepared by infiltrating poly(vinylidene fluoride-co-hexafluoropropylene) skeleton with binary mixtures of ionic liquids: 1-octadecyl-3-methylimidazolium bis(trifluoromethyl sulfonyl)imide ($[C_{18}C_1im][NTf_2]$) and 1-hexyl-3-methylimidazolium bis(trifluoromethyl sulfonyl)imide ($[C_6C_1im][NTf_2]$). The mixtures of ionic liquids are released spontaneously from the gel matrix and eventually crystallize on the surface, leading to self-replenishment of the surface of ionogels. The incorporation of $[C_6C_1im][NTf_2]$ provides the antimicrobial efficacy of ionogels while the crystals of $[C_{18}C_1im][NTf_2]$ serves as a skeleton maintaining $[C_6C_1im][NTf_2]$ on the surface. By heating, the ionogel surface transforms from solid to liquid-infused state that facilitates the removal of biofilms developed under a long time of colonization. The antimicrobial efficacy is maintained even after several cycles of biofilm formation and detachment.

§ This chapter is a slightly modified version of the following article:[245]

L. Ye, F. Chen, J. Liu, A. Gao, G. Kircher, W. Liu, M. Kappl, S. Wegner, H. -J. Butt, and W. Steffen. *Macromol. Rapid Commun*. **2019**, *40*, 1900395.

Author Contributions: L. Y. conceived the idea and performed the main experiments of this work. H. -J. B., W. S. supervised the project. F. C. cultivated the bacteria and carried on the antibacterial assays. G. K. synthesized the ionic liquid. J. L., A. G., W. L., M. K., and S. W. participated in the material characterizations and analyses. L. Y., F. C., H. -J. B., and W. S. wrote the manuscript.

3.1 Introduction

Biofouling has a significant impact on a wide variety of areas as health, economy, or environment causing negative consequences.[22, 23] Bacteria have evolved many strategies to attach to surfaces and form biofilms effectively.[246, 247] The incorporation of biocides,[25, 248-250] or the functionalization with specific moieties has been widely exploited to prevent bacterial adhesion and biofilm growth on the surface.[26, 27, 251] For instance, polymer membranes impregnated with silver nanoparticles inhibit bacterial growth by releasing ions that can disrupt the bacterial membrane, enzymes and proteins.[252] However, non-specific adsorption of protein and surfactant secreted by bacterial cells is not negligible, which will mask the antimicrobial-related surface chemistry.[28, 253-255] Poly(ethylene glycol) (PEG)-modified surfaces exhibit superior bacterial resistance by minimizing the non-specific protein adsorption.[256, 257] But it is well known that PEG is prone to (per)oxidation, resulting in degradation of polymer chains.[258] Bifunctional surfaces prepared with zwitterionic or responsive moieties can switch surface properties where bacteria can be killed on contact and then released by external stimuli, *i.e.*, changing temperature, pH, *etc*.[25, 26] Nevertheless, it is unknown whether the underlying mechanism based on the transition of molecular conformations would still work when the surface is covered with biofilms over time.

Superhydrophobic surfaces with non-wetting features have been reported to delay biofilm formation.[24, 259] Superhydrophobic surfaces resist the wetting of water by entrapping air plastron within the micro-/nano- hierarchical structures, reducing the contact between the surface and microbes. However, the bacterial resistance of superhydrophobic surfaces is reported to be short-lived, and the hierarchical surface structures even promote bacterial adhesion after losing the entrapped air.[98] Recently, slippery liquid-infused porous surfaces (SLIPSs) with the dynamic surface have been

reported to resist the adhesion of bacteria, algae, and mussels.[28, 108, 132] SLIPSs are microstructured (porous) substrates impregnated with a thin liquid film, minimizing the contact of bio-contaminants with the solid surface. However, the depletion of the infused liquid caused by evaporation or drainage leads to the loss of surface functionality.[134-136] Although SLIPSs with self-replenishing features based on polymeric gels have been recently developed, the active control against the loss of infused liquids remains impossible.[137-141]

Ionogels are hybrid material with a high content of immobilized ionic liquids in a highly porous polymer matrix.[142] Ionic liquids, known as 'green solvents', are organic salts with low melting temperatures and negligible vapor pressure.[145, 260] Ionic liquids exhibit antimicrobial efficiency with high selectivity for bacteria over mammalian cells.[158, 159, 261-263] Surfaces grafted with ionic liquids show superior performance against multidrug-resistant superbugs.[158] Meanwhile, ionic liquids are reported as a promising infusing liquid for SLIPSs due to their physicochemical stabilities.[125, 264, 265] The ionic liquid-infused textured surfaces exhibit excellent dynamic omniphobicity.[264]

In this chapter, a new type of responsive ionogel with a self-replenishing surface is prepared for attaining renewable antibiofouling properties. The mixtures of two ionic liquids with compatible chemical structures but with different lengths of alkyl chain in the cation are used to prepare responsive ionogels with self-replenishing surface properties. A semicrystalline polymer is used as a skeleton to attain good mechanical properties for the ionogels. The surface properties and antibiofouling performances of the ionogels are investigated.

3.2 Experimental

Materials: Poly(vinylidene fluoride-co-hexafluoropropylene) (PVDF-HFP, M_w = 400 kg mol^{-1}, M_w/M_n = 3.0, T_g = − 35 °C, T_m = 141 °C) was purchased from Sigma Aldrich

(Germany). 1-hexyl-3-methylimidazolium bis(trifluoromethyl sulfonyl)imide ($[C_6C_1im][NTf_2]$, T_g = − 9 °C) was purchased from Merck (Darmstadt). 1-octadecyl-3-methylimidazolium bis(trifluoromethyl sulfonyl)imide ($[C_{18}C_1im][NTf_2]$, T_m = 55 °C) was synthesized as follows:[266] 1-octadecyl-3-methylimidazolium chloride ($[C_{18}C_1im][Cl]$) was synthesized by electrophilic addition from *n*-methylimidazole with *1*-chlorooctadecane at 90 °C for 48 h under an argon atmosphere. The solid precipitates were washed with ether and recrystallized from tetrahydrofuran. $[C_{18}C_1im][NTf_2]$ was synthesized by metathesis reaction in aqueous solution from $[C_{18}C_1im][Cl]$ with bis(trifluoromethyl sulfonyl)imide lithium ($Li[NTf_2]$) salt. The product was recrystallized in a mixture of ethanol/water (75: 25).

Synthesis of Ionogels: Polymer solutions (0.5 g, 10 wt%) of PVDF-HFP in acetone were prepared at 40 °C with magnetic stirring for 4 h until a clear homogeneous solution was obtained. 2.0 g of ionic liquid mixtures with the different molar ratio was added to the polymer solution under magnetic stirring. They dissolved entirely within a few seconds. The solutions were cast into a petri dish, and the solvent was evaporated at room temperature for 24 h. Subsequently, the samples were dried under vacuum conditions at 60 °C for 12 h to get rid of volatile residual solvent.

Sample Characterizations: The thermal properties of ionogels were measured by differential scanning calorimetry (Mettler Toledo, DSC 822). The measurements were performed at a 10 °C min^{-1} scan rate with a temperature range from −70 °C to 190 °C. The fracture surface of the solvent extracted samples was inspected by a scanning electron microscopy (Zeiss, LEO Gemini 1530) with an accelerating voltage of 0.5 kV. The samples for the surface observation were prepared by solvent extraction of ionic liquid with acetonitrile, and then the solvent was gradually replaced by water at a step of 10% volume and finally freeze-dried overnight to remove the water.

The temperature-dependent surface wettability of ionogels and the manipulation of water droplet sliding were carried out with a goniometer (DataPhysics, OCA 35), equipped with a proportional–integral–derivative (PID) temperature controller (Brainchild, BTC 9300). To erase the surface roughness induced by solvent evaporation, the ionogel samples on a glass slide were heated to 160 °C for 1h and then carefully cooled to room temperature. For the water sliding angle measuring, a water droplet with the volume of 15 μL was applied. For the water sliding manipulation, the water droplet was put on the surface of the samples tiled by 5°, and the samples were first heated to 80 °C, then cooled to 25 °C and reheated to 80 °C again. The temperature was continuously manipulated by the PID temperature controller.

The self-replenishing properties of the ionogel surface were characterized by scratching-recovery tests. The samples were scratched by a flat head tweezer over 50 times and then left for recovery at room temperature overnight. The scratching-recovery test was carried out for more than 30 times to evaluate the long-time renewability. The fracture surface and top surface of the samples before/after scratching and after recovery at room temperature were inspected by scanning electron microscopy with an accelerating voltage of 1.5 kV.

The samples for antibacterial assays were prepared by spin-coating (10 wt% solution, 1000 rpm, 90 s) the ionogels on the glass substrate, while a bare glass slide was used as a control. The *E. coli* containing green fluorescent protein plasmid was cultured overnight in Lysogeny broth (LB) medium with 50 μg mL^{-1} ampicillin and 0.5 mM isopropyl β-D-1-thiogalactopyranoside (IPTG) at 37 °C, 250 rpm. 100 μL bacterial solution in phosphate-buffered saline (PBS) (OD_{600} = 0.1) was deposited on the surface of the samples and incubated at 37 °C for 6 h. The samples were kept in the 35 mm sterile Petri dishes with high humidity to prevent solvent evaporation. The

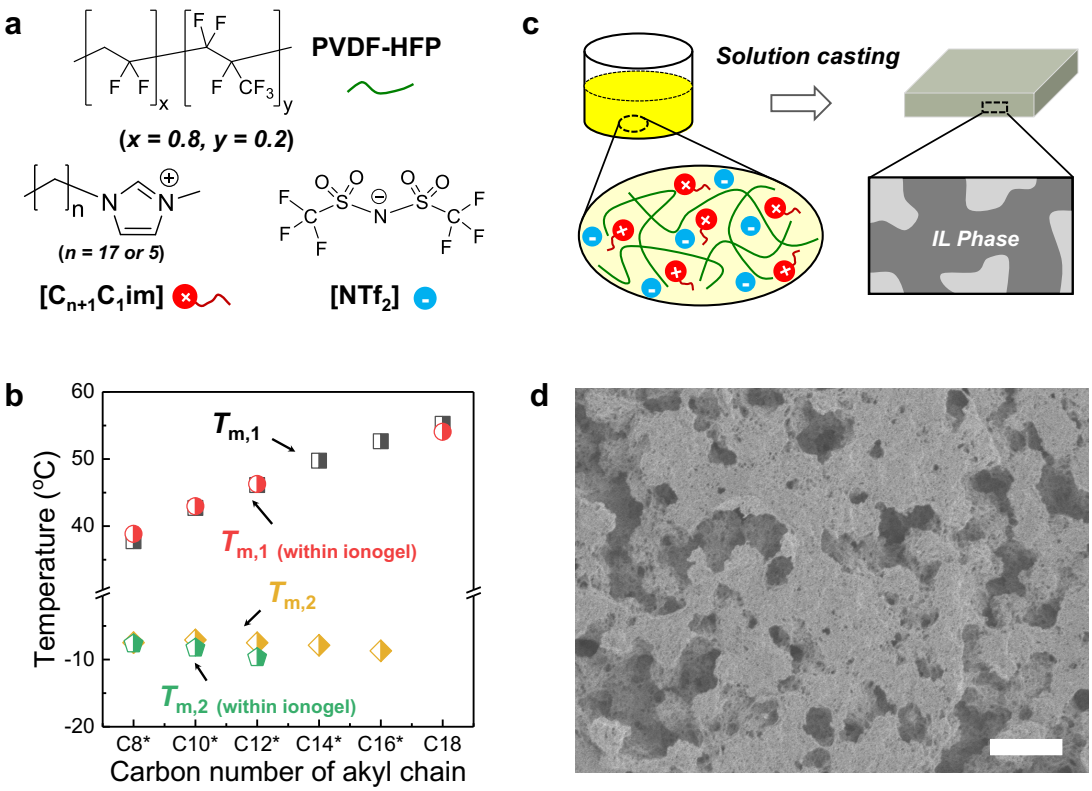

Figure 3.1 Preparation of ionogels. a) Chemical structure of poly(vinylidene fluoride-*co*-hexafluoropropylene) (PVDF-HFP) and 1-alkyl-3-imidazolium bis(trifluoromethyl sulfonyl)imide. b) Melting points of $[C_{18}C_1im][NTf_2]$ ($T_{m,1}$) and $[C_6C_1im][NTf_2]$ ($T_{m,2}$) in the mixtures (*Black, Yellow*) and within the ionogels (*Red, Green*). c) Schematic illustration of preparing ionogels from solution casting. d) Scanning electron microscopy (SEM) image of the fracture surface of **IG-C12*** after selective extraction of ionic liquids. Scale bar: 2 μm.

surface of the samples was then washed by PBS solution, and the bacteria were collected by centrifugation. The colony forming assays were performed with 40 μL of bacteria suspension with serial dilution on solid agar plates. The bacterial viabilities were calculated by dividing the colony forming units' (CFUs) numbers of the samples with the CFU number of the control.

For the evaluation of renewable antibiofouling properties, the samples (1 cm × 1 cm) were immersed into 3 mL of bacteria in LB solution (containing 50 μg mL^{-1} ampicillin and 0.5 mM IPTG, OD600 = 0.1) in sterile Petri dishes and incubated for varying time (12 h, 24 h, 48 h and 72 h). The samples were then washed in a 60 °C

water bath using a pipette for 2 min. The surface of the samples was inspected by a confocal laser scanning microscopy (Leica, SP8) using a 10x objective (NA = 0.8). The excitation wavelength was 488 nm. After that, the samples were re-incubated with the bacterial solution under the same conditions mentioned above for 72 h, and then the surface, as well as the antimicrobial efficacy, was examined after being washed through the same processes as described above. The biofilm formation and detachment processes were performed three times under the same conditions.

3.3 Results and Discussion

Table 3.1 Notation, molar ratio, and T_m of $[C_{18}C_1im][NTf_2]$ and $[C_6C_1im][NTf_2]$ in the mixtures.

Notation	**$[C_{18}C_1im][NTf_2]$: $[C_6C_1im][NTf_2]$**	**$T_{m,1}$ (°C)[a]**	**$T_{m,2}$ (°C)[a]**
$[C_6C_1im][NTf_2]$	/	/	−9.0[b]
$[C_8{*}C_1im][NTf_2]$	1:5	37.8	−7.5
$[C_{10}{*}C_1im][NTf_2]$	1:2	42.7	−7.1
$[C_{12}{*}C_1im][NTf_2]$	1:1	46.1	−7.5
$[C_{14}{*}C_1im][NTf_2]$	2:1	49.8	−7.8
$[C_{16}{*}C_1im][NTf_2]$	5:1	52.6	−8.7
$[C_{18}C_1im][NTf_2]$	/	55.0	/

[a] data from DSC curves performed by heating in a rate of 10 °C min^{-1} following the cooling from 100 °C to −70 °C. [b] data (T_g) from the supplier.

To prepare the ionogels, 1-octadecyl-3-methylimidazolium bis(trifluoromethyl sulfonyl)imide ($[C_{18}C_1im][NTf_2]$, **Figure 3.1**a) was synthesized. The $[C_{18}C_1im][NTf_2]$ was then mixed with 1-hexyl-3-methylimidazolium bis(trifluoromethyl sulfonyl)imide ($[C_6C_1im][NTf_2]$) to prepare ionic liquid mixtures with the varying molar ratios. The mixtures of ionic liquids are denoted as $[C_n{*}C_1im][NTf_2]$, where *n* is the statistical average carbon atom number (rather than an actual number of carbon atom) of the 1-alkyl chain (**Table 3.1**). The mixtures with different compositions showed two distinct

melting temperatures, which can be clearly seen in DSC curves (**Figure 3.1**b, **and Figure S3.1** in **Appendix I**). This phenomenon is different from that observed in eutectic mixtures of ionic liquids.[267, 268] It is regarded as the result of the mismatch between the cations due to the difference in length of 1-alkyl chains. The two components in the mixtures crystallized separately, which is similar to the crystallization of polymer blends.[269, 270] The $[C_6C_1im][NTf_2]$, which is still in a liquid state at room temperature, is maintained within the crystal network of $[C_{18}C_1im][NTf_2]$ with the formation of binary mixtures with the solid features.

The ionogels (denoted as **IG-C18**, or **IG-Cn***) are prepared by mixing $[C_{18}C_1im][NTf_2]$, or $[C_n{*}C_1im][NTf_2]$ with PVDF-HFP in a weight ratio of 80/20 ionic liquid/PVDF-HFP. PVDF-HFP is a semicrystalline polymer, which has been exploited to prepare solid electrolytes with good mechanical stability.[271-274] PVDF-HFP and ionic liquids were dissolved in acetone and mixed, then solution-cast into films with ~ 1 mm thickness after evaporation of the solvent. A deteriorating solvent quality during evaporation of the acetone leads to gelation of the solution by crystallization of PVDF-HFP and the gradual formation of a gel.[271] Both the T_m of $[C_{18}C_1im][NTf_2]$ and $[C_6C_1im][NTf_2]$ within the ionogels showed no apparent changes compared to those in the mixtures (**Figure 3.1**b). This result is ascribed to the phase separation between PVDF-HFP and ionic liquids. The homogeneous solution transformed into a gel with a bicontinuous structure comprised of polymer-rich and ionic liquid-rich phases after solvent evaporation (**Figure 3.1**c). This is proven, after selective extraction of the ionic liquid phase from the ionogels, by SEM (**Figure 3.1**d, and **Figure S3.2** in **Appendix I**). The pores of the structure are corresponding to the initial ionic liquid-rich phase that was selectively extracted. The semicrystalline PVDF-HFP phase served as an elastic, mechanically stable skeleton (confirmed by the dynamic mechanical properties,

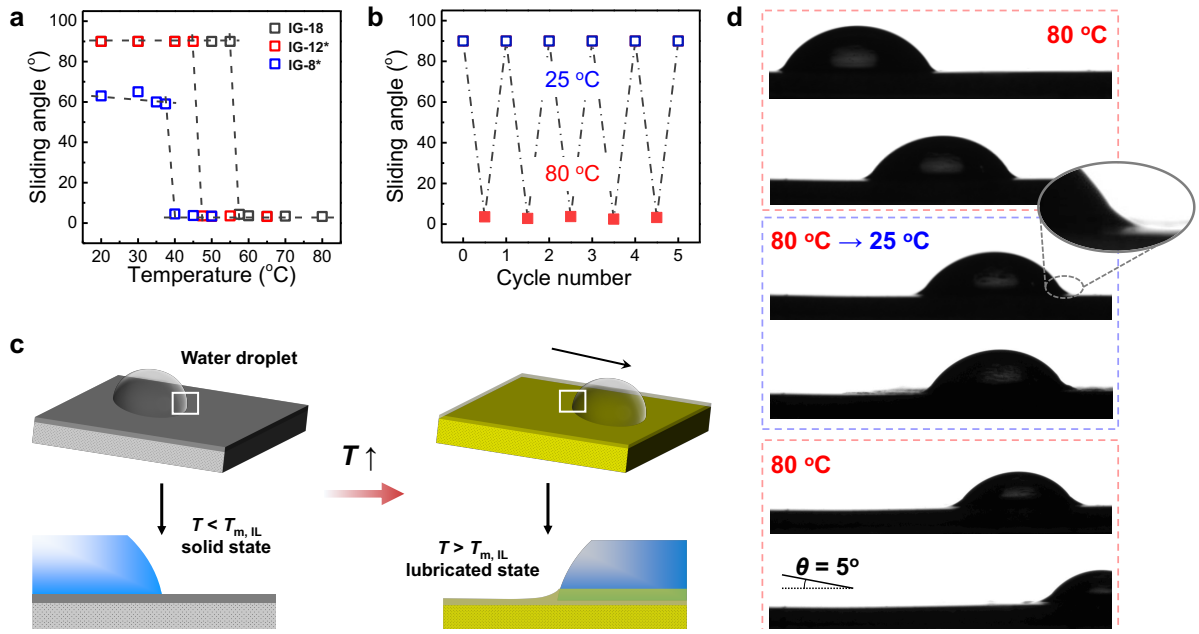

Figure 3.2 Temperature-dependent surface wettability of ionogels. a) Temperature dependence of the sliding angle of a water drop of 15 µL on the surface of ionogels. b) Multiple cycles of switching water drops sliding on the surface of **IG-C18** between 25 and 80 °C. c) Schematic illustration of "stick-slip" transition of water drops sliding on the ionogel surface. d) Demonstration of drop manipulation on the surface of **IG-C18** by varying temperature. A water drop with an initial volume of 15 µL was applied (the decrease in volume of the droplet is caused by the evaporation).

Figure S3.3 in **Appendix I**). The ionic liquids are infiltrated in the highly porous polymer skeleton without affecting the phase transition.

Before studying the antibiofouling properties, the temperature dependence of the sliding angle of water drops on the surface was investigated (**Figure 3.2**a). Water is immiscible with the ionic liquids as well as PVDF-HFP. A water drop placed on the ionogel surface formed a finite contact angle. A "stick-slip" transition of water drops sliding on the ionogel surface was observed when heating above the T_m of $[C_{18}C_1im][NTf_2]$. The T_m of $[C_{18}C_1im][NTf_2]$ varied from 55 °C for **IG-18** to 37.8 °C for **IG-8*** (**Table 3.1**). For example, water drops were pinned on the solid surface of **IG-12*** below 50 °C (the T_m of $[C_{18}C_1im][NTf_2]$). A water drop with a volume of 15 µL did

not slide off even when the surface was titled to 90°. Above 50 °C, water drops can slide down easily, and the sliding angle of a droplet is 3° at 65 °C. The sliding angle can be switched reversibly (**Figure 3.2**b). The phase transition of $[C_{18}C_1im][NTf_2]$ induces the transformation of the surface from the solid state to a slippery liquid-infused state (**Figure 3.2**c).[109, 113, 114, 275] Thus, the motion of a water drop on the surface can be regulated by varying the temperature (**Figure 3.2**d). The inspection of the rim (the inserted image) revealed a wetting ridge of ionic liquids surrounding the water drop at elevated temperatures, indicating a typical slippery liquid-infused surface.[109] The ionic liquids acted as a lubricant at elevated temperatures and facilitated the sliding of water drops on the surface. However, the liquid-infused surface transformed into a solid surface as ionic liquids crystallized upon cooling.

The surface morphology of ionogels at room temperature was inspected by SEM. The ionic liquid mixtures are observed to be released from the gel matrix forming flower-like structured crystals on the surface (**Figure 3.3**a). These crystals should be ascribed to $[C_{18}C_1im][NTf_2]$ since $[C_6C_1im][NTf_2]$ is still in the liquid state at room temperature. The flower-like structures on the surface exhibit self-healing properties after mechanical damage by scratching. In a typical experiment, the surface of **IG-C8*** was scratched and the recovery of the surface at room temperature was investigated (**Figure 3**b-c). The samples were scratched over 50 times and the flower-like structured crystals of ionic liquids were completely removed (**Figure 3.3**b). However, the crystals can be regenerated after storage at room temperature overnight (**Figure 3.3**c). The flower-like structures can be regenerated after more than 30 times of the scratching-recovery tests (**Figure 3.3**d).

The surface of those ionogels containing large content of $[C_6C_1im][NTf_2]$, including **IG-8***, **IG-10*** and **IG-12***, can be recovered after mechanical damage within 24 h. For

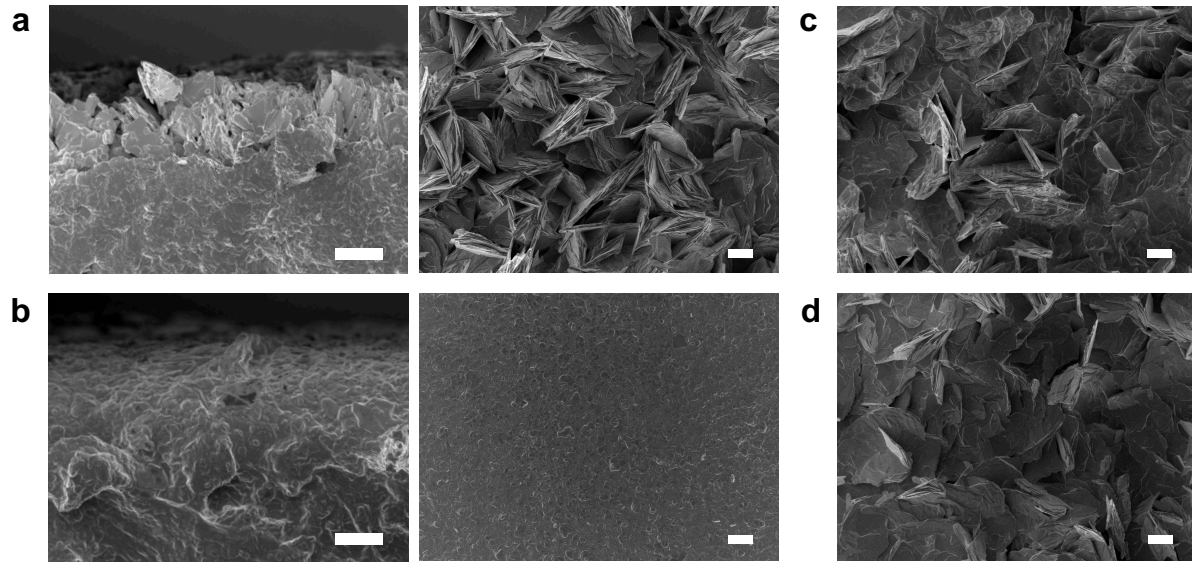

Figure 3.3 Self-replenishing properties of the ionogel surface. a) Scanning electron microscopic (SEM) images of fracture surface (left) and the top surface (right) of **IG-8***. b) SEM images of the fracture surface (left) and the top surface (right) of **IG-8*** after scratching over 50 times. c) SEM image of the top surface of **IG-8*** stored at room temperature overnight after mechanical scratching over 50 times. d) SEM image of the top surface of **IG-8*** after 30 times of scratching-recovery tests. Scale bars: 20 µm.

IG-14*, **IG-16*** and **IG-18**, the recovery of the surface becomes increasingly difficult. The self-replenishing behavior of the ionogel surface is attributed to the spontaneous migration of ionic liquids from the inner gel matrix to the surface. It is driven by a change in enthalpy of mixing. The polymer and ionic liquids are mixed by dissolving in a co-solvent. However, the evaporation of solvent/after gelation results in an increase in the free energy of mixing, leading to a demixing of polymer and ionic liquids. Therefore, ionic liquids can spontaneously leach out from the ionogels. In fact, a self-regulated migration of a liquid (syneresis[138, 139]) or even a solid (blooming[276, 277]) from polymer matrix has been observed previously. The diffusion of $[C_{18}C_1im][NTf_2]$ within the ionogels was difficult due to the high T_m. Therefore, the addition of $[C_6C_1im][NTf_2]$ remarkably enhanced the mobility of $[C_{18}C_1im][NTf_2]$.

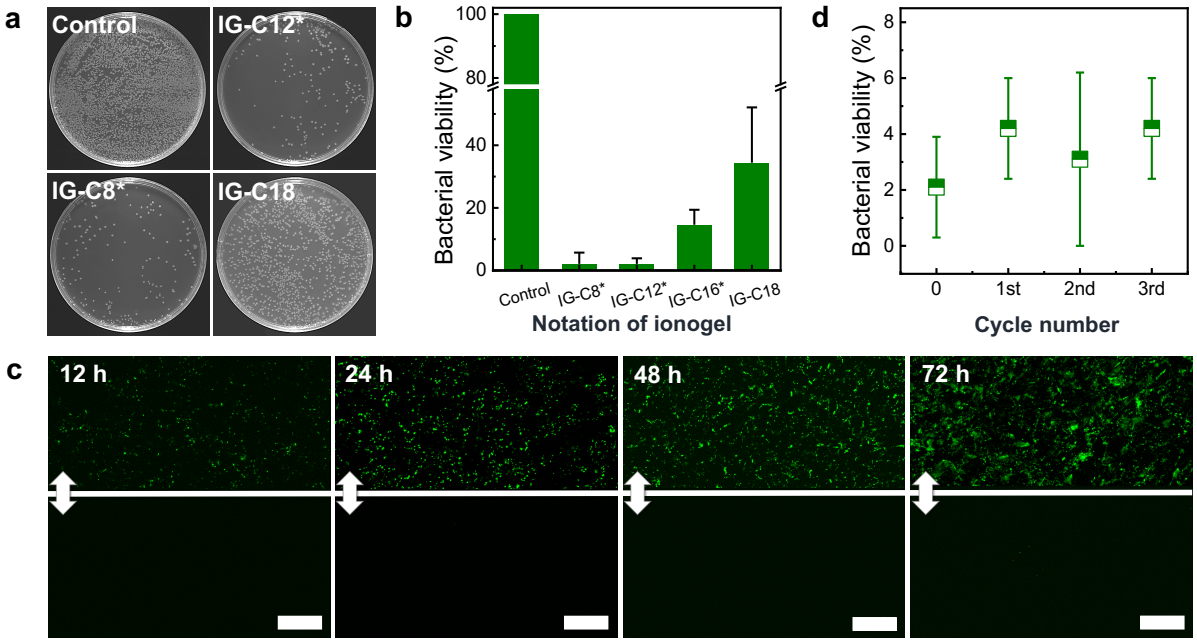

Figure 3.4 Antibiofouling performance of the ionogel surface. a) Optical images of *Escherichia coli* (*E. coli*) colonies forming after incubation on the ionogel-coated glass substrates for 6 h, using bare glass slides as the control. b) *E. coli* viabilities calculated from colony counting assay. c) Confocal laser scanning microscopic (CLSM) images (*Z*-projection) of the surface of **IG-C12*** before (upper) and after (lower part) gentle washing. Scale bar: 100 μm. Green fluorescent protein was incorporated into *E. coli* to make them visible in CLSM observations. d) *E. coli* viabilities after incubation on the surface of **IG-C12*** after each cycle of biofilm formation and detachment.

The antimicrobial activity of ionogels was tested using *E. coli*. Bacterial suspensions were incubated on the ionogel surface for 6 h. Then, the surface was washed with a PBS solution. The bacteria were collected and applied with serial dilution for plating and colony counting (**Figure 3.4**a). The ionogels containing a suitable amount of $[C_6C_1im][NTf_2]$, especially for **IG-C8*** and **IG-C12***, exhibit an excellent antimicrobial efficacy with bacterial viability below 10% (**Figure 3.4**b). The development of biofilm on the ionogel surface was further investigated. In a typical experiment, the ionogel samples were immersed into 3 mL of bacterial suspensions and incubated for up to 72 h until biofilm formation. The formation of biofilm on the surface of **IG-C12*** was investigated. On the bare glass surface, biofilms developed

within 24 h (**Figure S3.4** in **Appendix I**). However, only sporadic bacteria or aggregates were observed on the surface of **IG-12*** after incubation for 24 h (the upper part of confocal laser scanning microscopic (CLSM) images in **Figure 3.4**c). The results highlight the superior efficacy of the ionogel surface in inhibiting/delaying the development of biofilms.

When extending the incubation time, as expected, dense aggregates or biofilms started to form (**Figure 3.4**c). Although the ionogel surface can kill the bacteria at the initial stage, dead bacteria as well as the secretions from bacterial cells may serve as a barrier and facilitate the growth of the residual active bacteria to form biofilms. Due to the transition of surface properties, the biofilms can be removed gently by rinsing the surface at an elevated temperature. The surface of the **IG-C12*** samples with biofilm formation was rinsed using a pipette in a water bath of 60 °C for 2 min (the T_m of $[C_{18}C_1im][NTf_2]$ in **IG-12*** is 46 °C). The biofilm was easily washed away from the surface (**Figure 3.4**c). Upon heating, the surface of the ionogel turned into a liquid-infused state, facilitating the detachment of biofilms due to the dynamic surface properties. The cycle of biofilm formation and detachment can be carried out for at least three times (**Figure S3.5** in **Appendix I**). The antimicrobial efficacy of the ionogel was further examined after each cycle of biofilm formation and detachment (**Figure 3.4d**). It turned out no apparent decrease in antimicrobial efficacy happens after performing three cycles of biofilm formation and detachment. These results indicate the renewability of the ionogels for antibiofouling.

3.4 Conclusions

In this chapter, a new type of ionogels has been prepared by mixing solid/liquid binary mixtures of ionic liquids with a semicrystalline polymer. At room temperature, the mixtures of ionic liquids can be spontaneously released from the inner gel matrix and

crystallize at the surface. During the scratching/recovery test, the crystals of ionic liquids on the surface can be regenerated after being mechanically scratched for over 50 times, and the scratching/recovery tests can be carried out for more than 30 times. The ionogels maintaining a suitable amount of low-T_m ionic liquids exhibited excellent antimicrobial properties and inhibited the initial development of biofilms. Moreover, the mixtures on the surface acted as a sacrificial barrier and facilitated the removal of bio-contamination. Biofilms formed by incubation the ionogel in *E. coli* containing medium for 72 h can be easily washed away when heating to a temperature above the melting point of the mixtures. The cycle of biofilm formation and detachment can be carried out for at least three times without causing a dramatic decrease in antimicrobial efficacy of ionogels. This new type of ionogels combine the bactericidal properties of antimicrobial materials and the dynamic surface properties of SLIPSs. Such a combination provides a chance to tackle the irreversible loss of the antimicrobial efficacy of the surface after contamination and achieve active control against the unexpected loss of infused liquid (ionic liquid) of the surface.

3.5 Appendix I

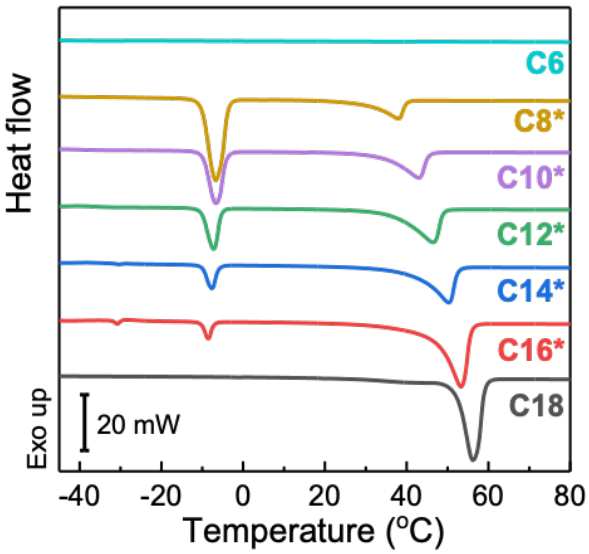

Figure S3.1 Phase transition behavior of $[C_6C_1im][NTf_2]$ and $[C_{18}C_1im][NTf_2]$ and their blends performed by a differential scanning calorimetry at a 10 °C min^{-1} scan rate with a temperature range from −70 °C to 100 °C. Two distinct T_m's are observed in the mixtures, indicating that the two ionic liquids crystallize separately. The low-T_m $[C_6C_1im][NTf_2]$ is maintained within the crystal networks of $[C_{18}C_1im][NTf_2]$ without the formation of eutectic mixtures.

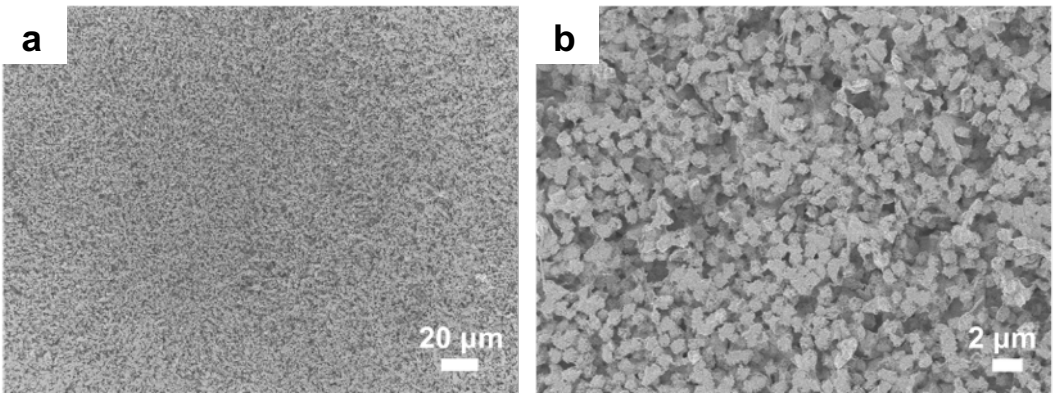

Figure S3.2 Scanning electron microscopy (SEM) images of top surface of **IG-12*** after selective extraction of ionic liquids: a) low magnification and b) high magnification.

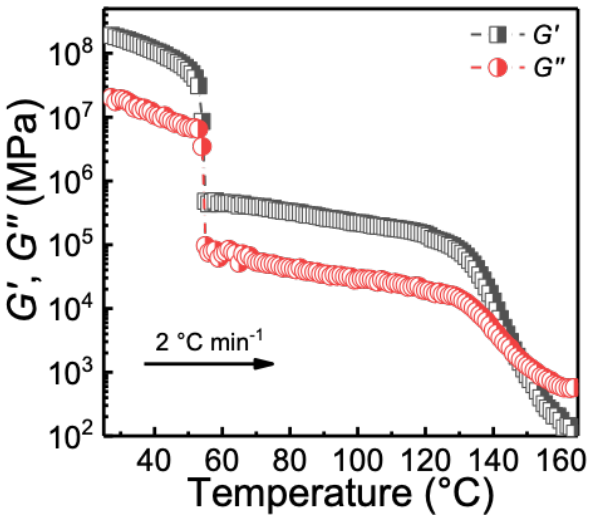

Figure S3.3 Dynamic mechanical properties (storage modulus *G*', and loss modulus *G*'') of **IG-C18** measured by a rheometer with parallel plate geometry with a temperature scan rate of 2 °C min^{-1} at frequency of 10 rad s^{-1}. The melting of ionic liquid is happening at 50 − 60°C. Then, the material turned into a viscoelastic solid or gel-like material with an extended plateau with *G*' > *G*''. The material starts to flow (becomes a viscoelastic liquid) above 140 °C.

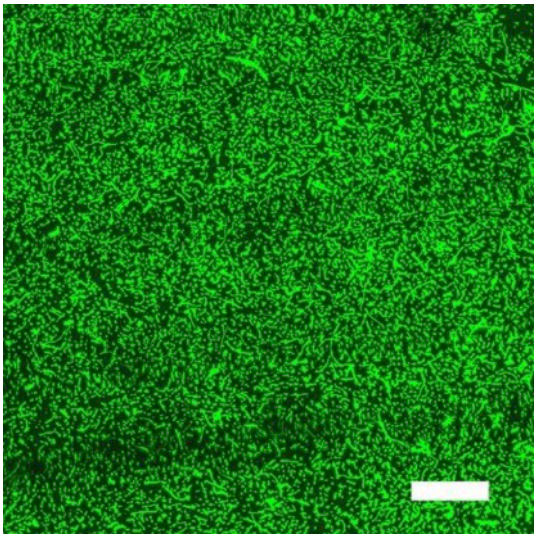

Figure S3.4 Confocal laser scanning microscopic (CLSM) images (*Z*-projection) of bare glass slides after incubation in bacterial suspensions for 24 h. Scale bar: 100 μm.

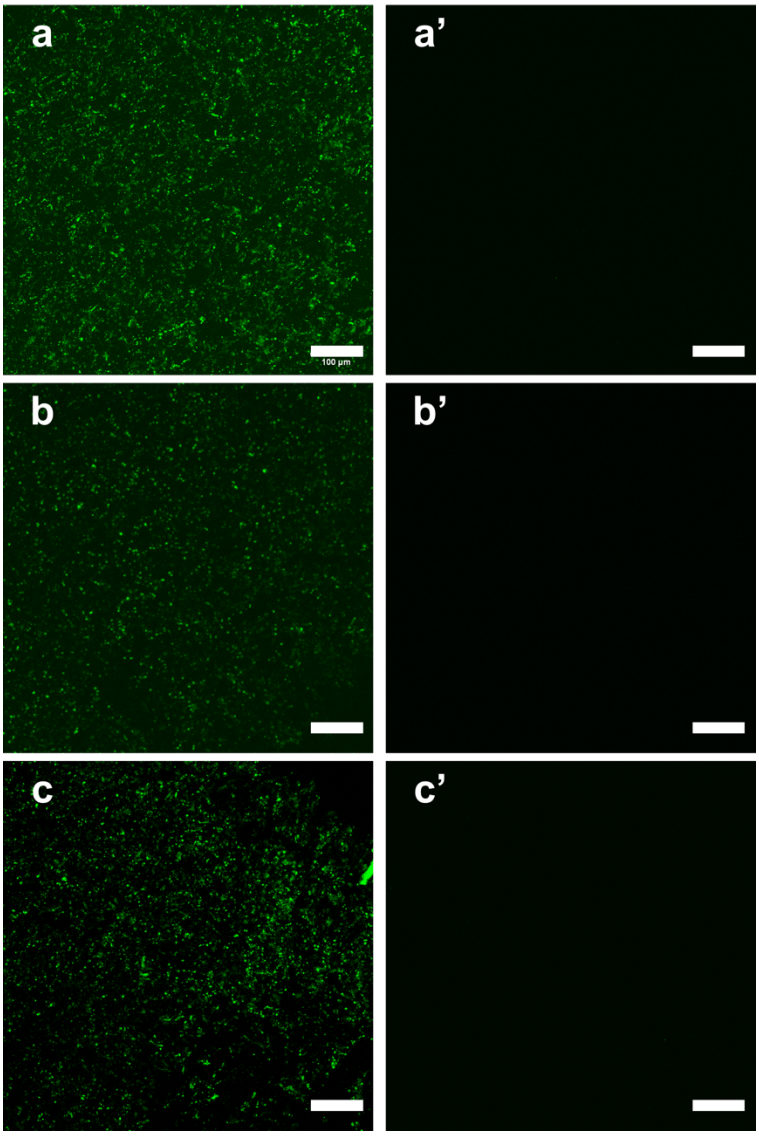

Figure S3.5 Confocal laser scanning microscopic (CLSM) images (*Z*-projection) of the surface of **IG-C12*** after 72 h of incubation in bacterial suspensions. The images before a), b), c), and after a'), b'), c') being washed by water at 60 °C. a) → a'): 1st cycle; b) → b'): 2nd cycle; c) → c'): 3rd cycle, scale bar: 100 µm.

Chapter 4

Elastic, Superhydrophobic and Photocatalytically Active Coating for Blood Repelling Dressing§

Mechanical robust and biocompatible superhydrophobic surfaces are of great potential in wound dressing for reducing uncontrolled hemorrhage and wound infection. In this chapter, a mechanical elastic, superhydrophobic composite coating with photocatalytic activity is described. The superhydrophobic coating was prepared from biocompatible titanium dioxide (TiO_2) nanoparticles and poly(dimethylsiloxane) (PDMS), where TiO_2 nanoparticles were chemically crosslinked by PDMS. The crosslinking of TiO_2 nanoparticles with PDMS results in forming hierarchical micro-/nano- superhydrophobic structures, which can be coated on various substrates. The PDMS crosslinks provided mechanical elasticity of the composite coating, allowing for robust blood repellency of the surface even under large deformations. The photocatalytic activity of TiO_2 nanoparticles offered additional self-cleaning and antibacterial properties under UV illumination. The superhydrophobic PDMS/TiO_2 composite coating exhibited great potential for wound dressing reducing blood loss and bacterial infections.

§ This chapter is a slightly modified version of the following article:[278]

J. Liu, **L. Ye,** Y. Sun, M. Hu, F. Chen, S. Wegner, V. Mailänder, W. Steffen, M. Kappl, and H. -J. Butt. *Adv. Mater*. **2020**, *32*, 1908008.

Author Contributions: J. L. designed and performed the research. W. S., H. -J. B. supervised the project. L. Y., Y. S., M. H., F. C., S. W., V. M., and M. K. participated in material characterization and analyses. Specifically, L. Y. participated in the characterizations of bacterial adhesion, blood repellency under stretching, and the joint-mimicking experiment. J. L., W. S., M. K., H. -J. B. wrote the manuscript.

4.1 Introduction

Proper wound treatments at the first-response aid are of utmost significance since uncontrolled hemorrhage and wound infection have emerged as the main cause of death.[279-281] On the other hand, the exposure and transfer of blood between patients and medical personnel pose great risks of cross-infection of bacteria or virus.[282-285] The traditional medical textiles such as cotton fabrics comprised of biodegradable cellulose fibers are (super)hydrophilic, which makes them easily impregnated by the blood.[286] Although the superhydrophilic textiles can help stop bleeding by fast adsorbing the liquid from the blood to accelerate blood coagulation, they could also lead to excessive blood loss due to uncontrolled adsorption.[29, 103] Moreover, blood coagulation on medical textiles leads to the formation of concrete clot-gauze composites at wounds. The clot-gauze composites makes it difficult to replace and remove the old dressings without causing additional pain, secondary bleeding, and potential infections.[103, 287] In addition, the natural breathability of the medical textiles, which is important for wound healing, is inevitably reduced due to the permeation and solidification of the blood.[31, 288]

Superhydrophobic surfaces with non-wetting features are reported to have great potential in repelling blood,[30, 33, 102] and reducing bacterial adhesion.[24, 259] The hierarchical structures of the superhydrophobic surface with a trapped air plastron effectively reduce the contact between blood and the surface.[30] The resistance of superhydrophobic surfaces to the wetting of blood at wounds potentially reduces the blood loss of the patients and the direct contact of the medical personnel with the blood. *Zhu et al*. reported that Janus superhydrophobic/superhydrophilic fabrics can promote blood coagulation while reducing the excessive blood loss.[29] This relies on the fact that the superhydrophilic side of fabrics promotes blood coagulation by rapid

water adsorption. At the same time, the superhydrophobic backside prevents excessive blood loss by resisting the penetration of the blood.[29, 31] On the other hand, superhydrophobic surfaces effectively reduce the formation of clot-gauze composites due to the reduced permeation of blood. *Li et al*. reported a type of superhydrophobic hemostatic surface with immobilized carbon nanofibers.[103] They observed that carbon nanofibers could promote rapid clotting while the superhydrophobicity of the surface results in minimal blood adhesion.

However, the practical applications of superhydrophobic surfaces for blood-repelling dressings are still limited by their poor mechanical stability and lack of biocompatibility. For instance, the fragility of superhydrophobic structures makes them easily destroyed when a bleeding wound is usually treated with medical gauze by mechanical pressure, producing free microparticles which pose a risk of causing micro-thrombosis when they enter the vascular system.[34, 35] On the other hand, fluorinated hydrocarbons are often used to achieve superhydrophobicity due to their low surface energy. However, fluorinated hydrocarbons are nondegradable and have a great negative impact on the environment and human health.[289, 290]

In this chapter, a new method of preparing robust blood-repellent surfaces from titanium dioxide (TiO_2) nanoparticles and polydimethylsiloxane (PDMS) is described. Various substrates can be modified with hierarchical micro-/nano- structures achieving superhydrophobicity by the assembly of TiO_2 nanoparticles crosslinked with PDMS. Both TiO_2 and PDMS are known as biocompatible materials.[291-296] TiO_2 is photocatalytically active under UV illumination,[297, 298] while PDMS exhibits good resistant to UV light.[299, 300] The combination of elastic PDMS and photocatalytically active TiO_2 nanoparticles provides the superhydrophobic surface with superior mechanical strength, antibacterial efficiency, and blood-repelling properties.

4.2 Experimental

Modification of Titanium Dioxide Nanoparticles. 0.5 g titanium dioxide nanoparticles (TiO_2, diameter: 21 ± 5 nm, P25, Sigma) were dispersed in tetrahydrofuran (THF, 10 mL) by sonication. 30 mL (25 − 35% methylhydrosiloxane)-dimethylsiloxane copolymer (PDMS-copolymer, M_w: 1.9 − 2.0 kDa, Gelest Inc.) was added and mixed with TiO_2 nanoparticles in THF. THF was left for evaporation at room temperature for 24 h, and the particle dispersion was illuminated with UV-A light (intensity: 10 mW cm^{-2}) and stirred for 10 h.[301] After the reaction, the modified TiO_2 nanoparticles were purified by centrifugation at 10 000 rpm for 10 min and redispersed in THF. This process was repeated five times. The modified nanoparticles can easily disperse in organic solvents such as THF, toluene and hexane. The mass of modified TiO_2 nanoparticles dispersed in THF was measured by weighing the deposition of 10 μL dispersion with a balance (Sartorius Genius ME, Mettler Toledo) after evaporation of THF. The concentration of particles was finally controlled to be 7.0 wt%.

Preparation of PDMS/TiO_2 Films. The modified TiO_2 nanoparticles (dispersed in THF, 7.0 wt%) were mixed with vinyl-terminated PDMS (vinyl-PDMS, M_w: 62.0 kDa, Gelest) as well as Pt-catalyst (0.005 wt% relative to vinyl-PDMS, Platinum(0)-1,3-divinyl-1,1,3,3-tetramethyldisiloxane complex solution in xylene, Gelest) at a certain ratio in in toluene (or THF, hexane). The substrates (glass, polyester fabrics, polyurethane, commercial wound dressings) were pre-modified with oxygen plasma (5 min, power: 100%). Then, the substrates were immersed into the mixture and allowed to react in a closed chamber at 60 °C for 6 h. The crosslinking reaction between PDMS molecules occurred both in bulk and on the surface of the substrates, with the formation of composite gels anchored on the substrates. After removing PDMS residues with toluene, superhydrophobic nanostructures can be attained on the surface.

Characterization of Mechanical Properties. The elastic modulus and hardness of the samples anchored on glass substrates were measured with a MFP-3D Nanoindenter (Asylum Research, Santa Barbara, CA) equipped with a diamond Berkovich indenter was used. A maximum loading force of 100 μN was applied. Young's modulus and hardness were obtained from the indentation curves by fitting the unloading curves with the Oliver-Pharr model.

Bacterial Viability Assay. E. coli K12 MG1655 were transformed with a fluorescent protein expression plasmid (GFP-pTrc99A, ampicillin resistant, isopropyl β-D-thiogalactoside (IPTG) inducible). 10 mL of Lysogeny broth (LB) medium containing 50 μg mL^{-1} ampicillin and 0.5 mM IPTG were inoculated with a single colony and incubated overnight at 37 °C at 250 rpm. The bacteria were diluted with phosphate buffer saline (PBS), or LB medium, to the desired density (OD_{600} = 0.1). The glass slides (control) and PDMS/TiO_2-covered glass slides were fixed on the bottom of sterile borosilicate 2-well plates (ibidi μ-Slide, glass bottom). 2 mL of bacterial solution was added and incubated for up to 210 min in the dark and under UV-light illumination (5 ± 0.5 mW cm^{-2}), respectively. To evaluate the bacterial viability after incubation with the sample surfaces, the bacteria were mixed with propidium iodide (PI, 1 μL mL^{-1} bacterial culture), which selectively enters cells with damaged membranes, and incubated for 15 min to stain the dead cells. Stained bacteria were observed using a Leica SP8 laser scanning confocal microscope with excitation wavelengths of 488 and 610 nm. All bacteria display green fluorescence due to the expression of the GFP protein. Dead bacteria display red fluorescence of PI.

Blood Repellency Properties. 100 μL of human blood was put on the modified textile forming spherical shape and left for evaporation at room temperature for 1 h. The blood droplet can easily slide off from when the surface was tilted for 8°. For the

stability test, the coated textiles were immersed into human blood for 1 to 10 times, each time the surface was in blood for 1 h. The advancing and receding contact angles as well as contact angle hysteresis were measured. Human blood was obtained from the Department of Transfusion Medicine Mainz from ten healthy donors after physical examination and after obtaining their informed consent in accordance with the Declaration of Helsinki. The use of human blood was approved by the local ethics committee "Landesärztekammer Rheinland-Pfalz" (837.439.12 (8540-F)).

Hemostasis Properties. The PDMS/TiO_2 layer was coated on the commercial medical gauze. A blood loaded-polyvinyl chloride (PVC) tube with an incision was used to mimic a bleeding wound. The PVC tube was fixed on a forefinger with the incision site located at the finger joint, mimicking a wound near a joint. The incision was bandaged with the modified (3 layers) or unmodified (3 layers) medical gauzes. The 'bleeding' was monitored during finger bending.

4.3 Results and Discussion

As reported previously, PDMS can be easily grafted onto the surface of metal-oxide photocatalysts under UV-A light illumination.[301, 302] In this work, the surface of TiO_2 nanoparticles was first grafted with a PDMS-copolymer (**Figure S4.1**a, and **Figure S4.2** in **Appendix II**). The modified TiO_2 nanoparticles can quickly dispersed in toluene forming a stable suspension (**Figure S4.1**b in **Appendix II**). The modified TiO_2 nanoparticles were then mixed with vinyl-terminated PDMS and Pt-catalyst with a certain ratio in toluene. In the presence of a Pt-catalyst, the –Si–H bonds of PDMS-copolymers on TiO_2 nanoparticles can react with the $–CH=CH_2$ of vinyl-PDMS (**Figure 4.1**a),[303] which drives the connection between nanoparticles with covalent crosslinks. Superhydrophobic PDMS/TiO_2 composite films with hierarchical structures can be formed on various substrates after removal of PDMS residues.

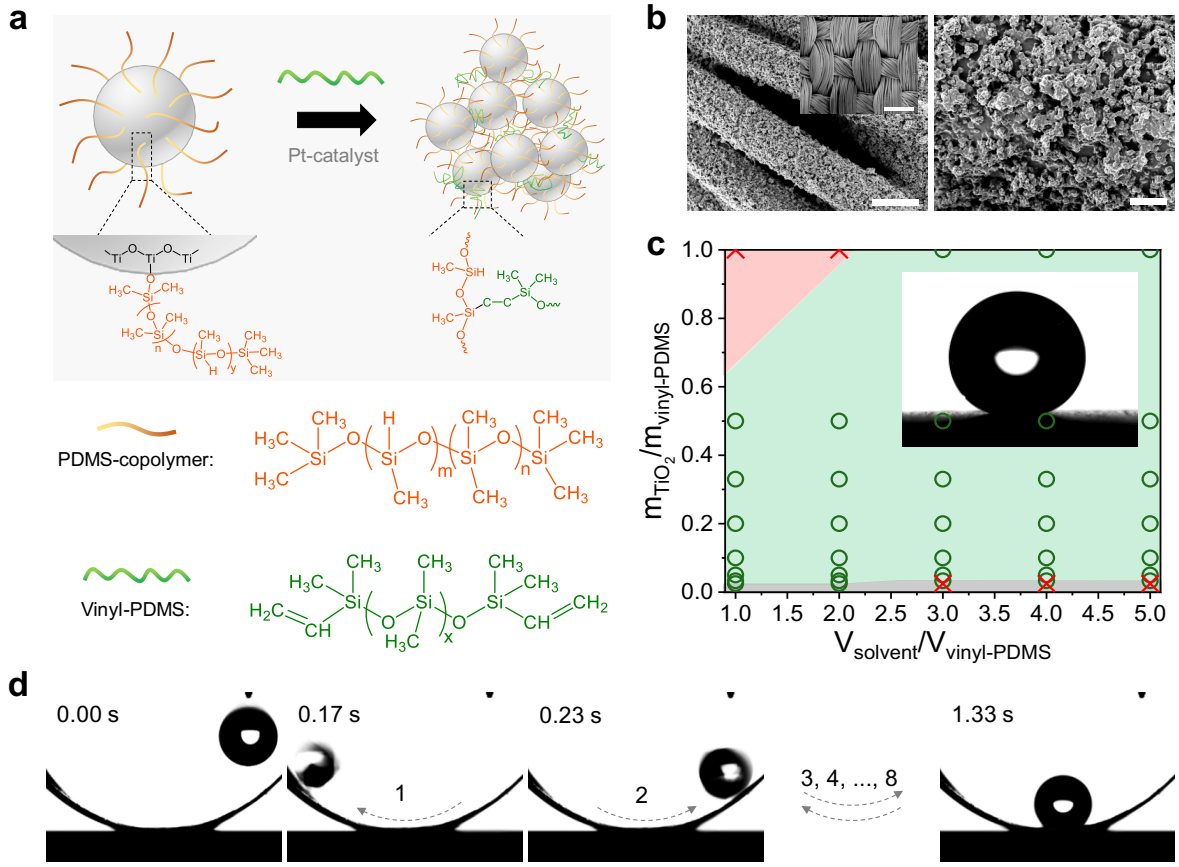

Figure 4.1 Superhydrophobic PDMS/TiO_2 composite films on various substrates. a) Schematic illustration of the fabrication of PDMS/TiO_2 composites. b) Morphology of polyester fabrics covered with PDMS/TiO_2 film at different magnifications. From left to right, the scale bars are 10 µm (inset: 200 µm) and 2 µm. $m_{TiO2}/m_{vinyl\text{-}PDMS}$ = 0.1, $m_{TiO2}/m_{vinyl\text{-}PDMS}$ = 3, where $m_{TiO2}/m_{vinyl\text{-}PDMS}$: mass ratio of TiO_2 nanoparticles to vinyl-PDMS; $V_{solvent}/V_{vinyl\text{-}PDMS}$: volume ratio of solvent to vinyl-PDMS. c) Optimal parameters for preparing superhydrophobic surfaces. ○: formation of superhydrophobic surfaces (light green background); ×: failed formation of superhydrophobic surface (pink and gray background). Inset: a 5 µL water drop on the PDMS/TiO_2 films. d) Sequence shows a water droplet (5 µL) sliding on the bent polyurethane tape coated with PDMS/TiO_2 composite films.

Figure 4.1b shows the morphology of PDMS/TiO_2 film on polyester fabrics. The PDMS/TiO_2 film uniformly covered the textile surface, even the surface inside the fabrics. The static water contact angle on this surface was 165° ± 1°. The assembly of TiO_2 nanoparticles on the fabrics forming of hierarchical surface structures (**Figure S4.3**, and **Figure S4.4** in **Appendix II**). The polyester fabrics coated with unmodified

TiO_2 nanoparticles has poor water-repellent properties with advancing contact angles lower than 140°. Since unmodified TiO_2 nanoparticles tended to aggregate in PDMS, the surface roughness was insufficient to yield superhydrophobicity.[304] Here, the surface was defined to be superhydrophobic when the static contact angle exceeded 150°. **Figure 4.1**c shows the optimal conditions for preparing superhydrophobic surface. When the concentration of TiO_2 nanoparticles was too high, the contact angle of water on the PDMS/TiO_2 film was only around 142°. In contrast, when the particles and vinyl-PDMS were too diluted, the low crosslink density of TiO_2 nanoparticles led to failure of connection between particles.

As another example, the PDMS/TiO_2 composite film was coated on polyurethane (PU) tape. To demonstrate the low energy dissipation of sliding drops, the substrates were bent, and a water drop can slide back and forth on the PU surface for 8 times (**Figure 4.1**d). The mechanical stability of the PDMS/TiO_2 film on PU tapes was further investigated under stretching and bending conditions. The variation of the advancing (Θ_{ACA}), receding (Θ_{RCA}) contact angles and contact angle hysteresis (Θ_{CAH}) of the PU tapes is shown in **Figure 4.2**a, b. The PDMS/TiO_2-coated PU tapes exhibited superior superhydrophobicity (Θ_{ACA} = 166° ± 1° and Θ_{RCA} = 165° ± 1°) with an extremely low contact angle hysteresis ($\Theta_{CAH} \approx 1°$) when the elongation did not exceed 180% (**Figure 4.2**a). A 5 μL water drop can slide easily off from the PDMS/TiO_2-coated PU tapes stretched to 140% at a tilting angle of only 1°. Although Θ_{RCA} decreased to 150° ± 1° after stretching to 200%, the PDMS/TiO_2-coated PU tapes are still superhydrophobic (**Figure S4.5** in **Appendix II**). The PDMS/TiO_2-coated PU tapes exhibited good resistance to bending, as reflected by the stable Θ_{ACA} and Θ_{RCA} and low Θ_{CAH} after bending the surface between 90° and 180° for 1000 times (**Figure 4.2**b). Besides, the modified PU tapes showed stable repellency to the water jet in the bending state.

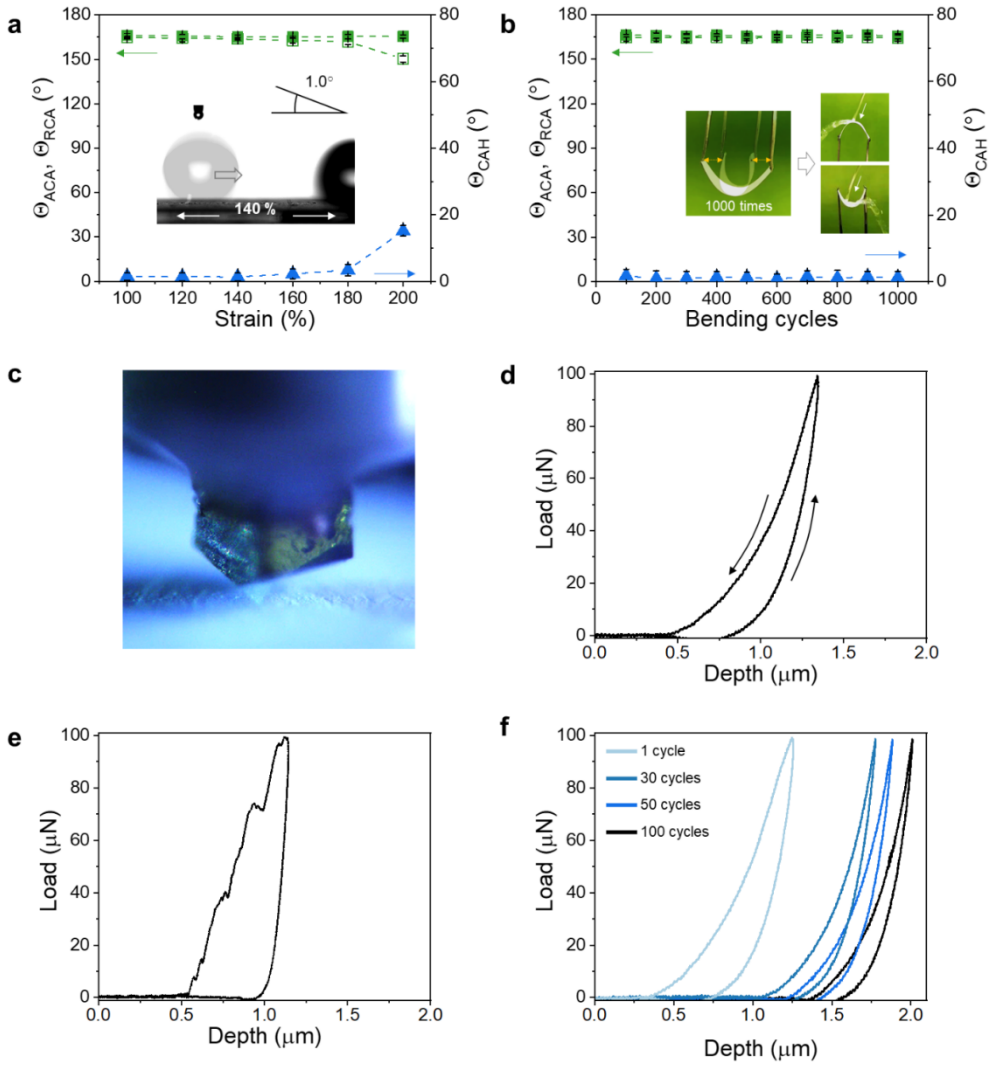

Figure 4.2 Mechanical stability of PDMS/TiO_2 composite films. a) The advancing contact angle (Θ_{ACA}, ■), receding contact angles (Θ_{RCA}, □), and contact angle hysteresis (Θ_{CAH}, ▲) of the PDMS/TiO_2 film on PU tape as a function of strain. Inset: a 5 μL water drop sliding on a stretched (140% strain) and tilted (1°) polyurethane tape coated with PDMS/TiO_2 film. b) The advancing contact angle (Θ_{ACA}, ■), receding contact angles (Θ_{RCA}, □), and contact angle hysteresis (Θ_{CAH}, ▲) of the PDMS/TiO_2 film on PU tape after repeated bending cycles. Inset: the bending of the PU tape with angles ranging from 90° to 180°. c) Berkovich diamond indenter approaching the film surface. d) Indentation force vs. depth curve as the indenter presses into and withdraws from the PDMS/TiO_2 film on a glass substrate. e) Indentation force vs. depth curve as the indenter presses into and withdraws from the inorganic TiO_2 film. f) Indentation force vs. depth curves for repeated indentation at one certain position.

The elastic modulus and hardness of the PDMS/TiO_2 composite films were measured by nanoindentation. **Figure 4.2**d shows typical indentation curves of the

composite film on a glass substrate. The hysteresis between approach and retract curves is a result of partial plastic deformation of the samples during indentation. Indentation and unloading curves of the PDMS/TiO_2 composite films were smooth, indicating that no cracking or disruptive failure occurred in the structures. To elucidate the role of PDMS in the elasticity of the composite film, an inorganic superhydrophobic surface was prepared by heating the PDMS/TiO_2 film at 500 °C for 30 min. This results in the formation of TiO_2 films with similar surface structures, which could be rendered superhydrophobic by treatment with a fluorosilane. Though pure TiO_2 film showed a higher modulus and hardness (**Figure S4.6** in **Appendix II**) than PDMS/TiO_2 film, its capability to respond elastically to large strain deformation was much lower than that of the PDMS/TiO_2 film. Indentation curves of the inorganic film (**Figure 4.2**e) exhibited pronounced steps in the approach part. These steps indicate cracking or stepwise brittle failure of the structure, and much less elastic recovery with a larger permanent plastic deformation. In addition, multiple indentation cycles of the PDMS/TiO_2 film at the same testing site showed smooth and continuous force curves (**Figure 4.2**f), indicating that no obvious cracking occurred even up to 100 cycles.

The superhydrophobic PDMS/TiO_2 films exhibited superior photocatalytic activity and UV resistivity. The advancing contact angle of the films was maintained around 166° ± 1° with the contact angle hysteresis < 2°, even after UV-A illumination for 33 h (**Figure 4.3**a). Moreover, the superhydrophobicity of the composite films can be recovered by UV illumination even after contamination. The receding contact angle of the PDMS/TiO_2 composite film decreased from 165° ± 1° to 0° after contamination by oleic acid but recovered after UV-A illumination for 2 h (**Figure 4.3**b). After 6 cycles of contamination by oleic acid and photodegradation, the PDMS/TiO_2 films remained superhydrophobic. The PDMS/TiO_2 films showed superior self-cleaning properties

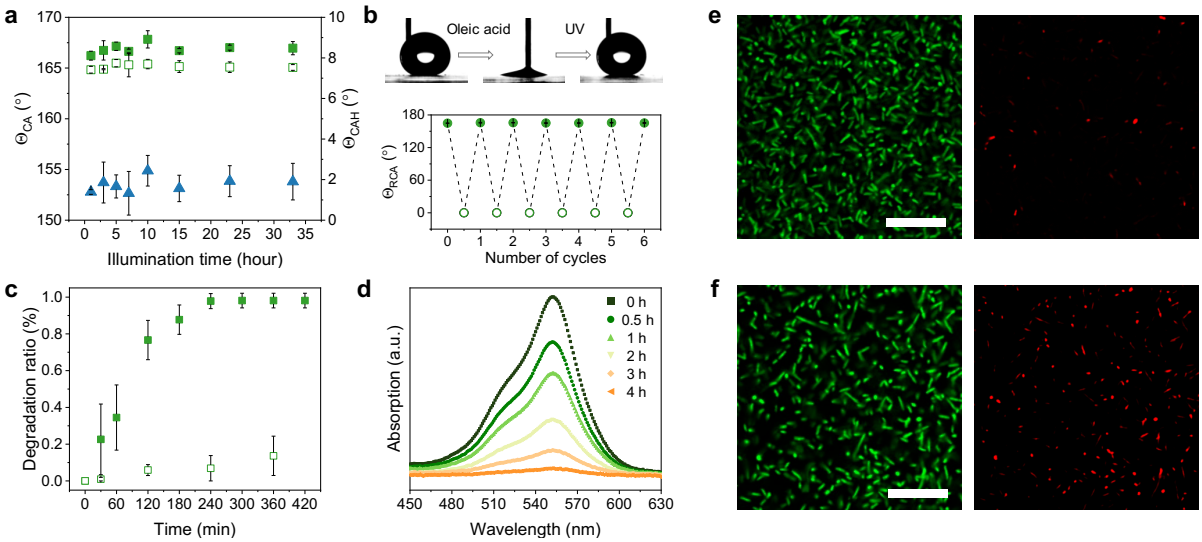

Figure 4.3 Photocatalytic activities of the PDMS/TiO_2 composite film ($m_{TiO2}/m_{vinyl\text{-}PDMS}$ = 0.1, $V_{solvent}/V_{vinyl\text{-}PDMS}$ = 3). a) Advancing (Θ_{ACA}, ■) and receding contact angles (Θ_{RCA}, □) and contact angle hysteresis (Θ_{CAH}, ▲) of water on PDMS/TiO_2 film as functions of the UV-A (5 ± 0.5 mW cm^{-2}) illumination time. b) Images comparing the receding contact angle of water on the PDMS/TiO_2 film before (left), after oleic acid contamination (middle), and after UV-A illumination for 2 h (right). The diagram shows the variation of the Θ_{RCA} of a water drop on the PDMS/TiO_2 film contaminated by oleic acid and UV-A illumination for 6 cycles. c) Degradation ratio for Nile red over time under illumination with UV-A light (10 ± 1 mW cm^{-2}) in the presence of PDMS/TiO_2 film (■) and glass surface (□). 10 µg mL^{-1} of Nile red was dissolved in silicone oil (10 cSt). d) UV–vis spectra of Rhodamine B (1 µg mL^{-1}, 3 mL) aqueous solution after being degraded by PDMS/TiO_2 film for different times (10 ± 1 mW cm^{-2}). e, f) Confocal laser scanning microscopy images of *E. coli* on the bare glass substrates (e) and PDMS/TiO_2 films (f) after incubation for 210 min under UV-A illumination (5 ± 0.5 mW cm^{-2}). Green and red fluorescence indicate alive and dead *E. coli*, respectively. Scale bar: 20 µm.

against both chemical and physical contamination (*i.e.,* inorganic particles, **Figure S4.7** in **Appendix II**).

The photocatalytically activity of the PDMS/TiO_2 films were further investigated by degrading chemicals in solvents. As an example, Nile red dissolved in silicone oil was degraded on the PDMS/TiO_2 films under UV illumination after 5 h (**Figure 4.3c**). The degradation of Nile red was much faster than that on glass substrates. Due to the low surface tension of silicone oil, the Nile red solution is in the Wenzel state on the films,

where dye molecules directly contact with TiO_2 nanoparticles.[48] In contrast, an aqueous solution is in the Cassie state on the film — an air layer exists between solution and the film. As shown in **Figure 4.3**d, Rhodamine B in aqueous solution can be completely degraded in 4 h under UV-A illumination.

The PDMS/TiO_2 films showed additional antibacterial properties under UV-A illumination (**Figure 4.3**e, f). The states (dead or live) of *E. coli* on glass substrates and PDMS/TiO_2 films after incubation for 210 min under UV illumination and in the dark were evaluated using confocal microscopy. The *E. coli*. incubated in the dark remains alive (**Figure S4.8** in **Appendix II**). Although UV illumination led to the death of a portion of *E. coli* both on glass substrates and on PDMS/TiO_2 films, significantly increased bacteria were killed on the PDMS/TiO_2 film. The results indicate an additional antibacterial activity of the film beyond the direct UV-A illumination. The free radical generated by TiO_2 nanoparticles in the composite films under UV light illumination,[301, 305, 306] promoting the destruction of bacterial cell membrane.

The wetting property of blood on the surface is quite different from water because of the lower surface tension (50 – 60 mN m^{-1}) and its intrinsic hemostatic mechanisms.[307-310] The PDMS/TiO_2-coated textiles showed a static contact angle larger than 150° for human blood (**Figure S4.9** in **Appendix II**). To further characterize the blood repellency, a 100 µL of blood drop was deposited on a coated textile for 1 h (**Figure 4.4**a). The blood drop can slide easily off from the surface when tilted by 8° (**Figure 4.4**b). No blood stain can be discerned on the surface after removal of the drop (**Figure 4.4**c). In another test, the coated textiles were immersed in blood multiple times. The contact angles of blood drops on the textiles did not change (**Figure 4.4**d). The stable blood repellent performance of the coated textile is attributed to the hierarchical micro-/nano- structures providing a stable air layer on the surface when

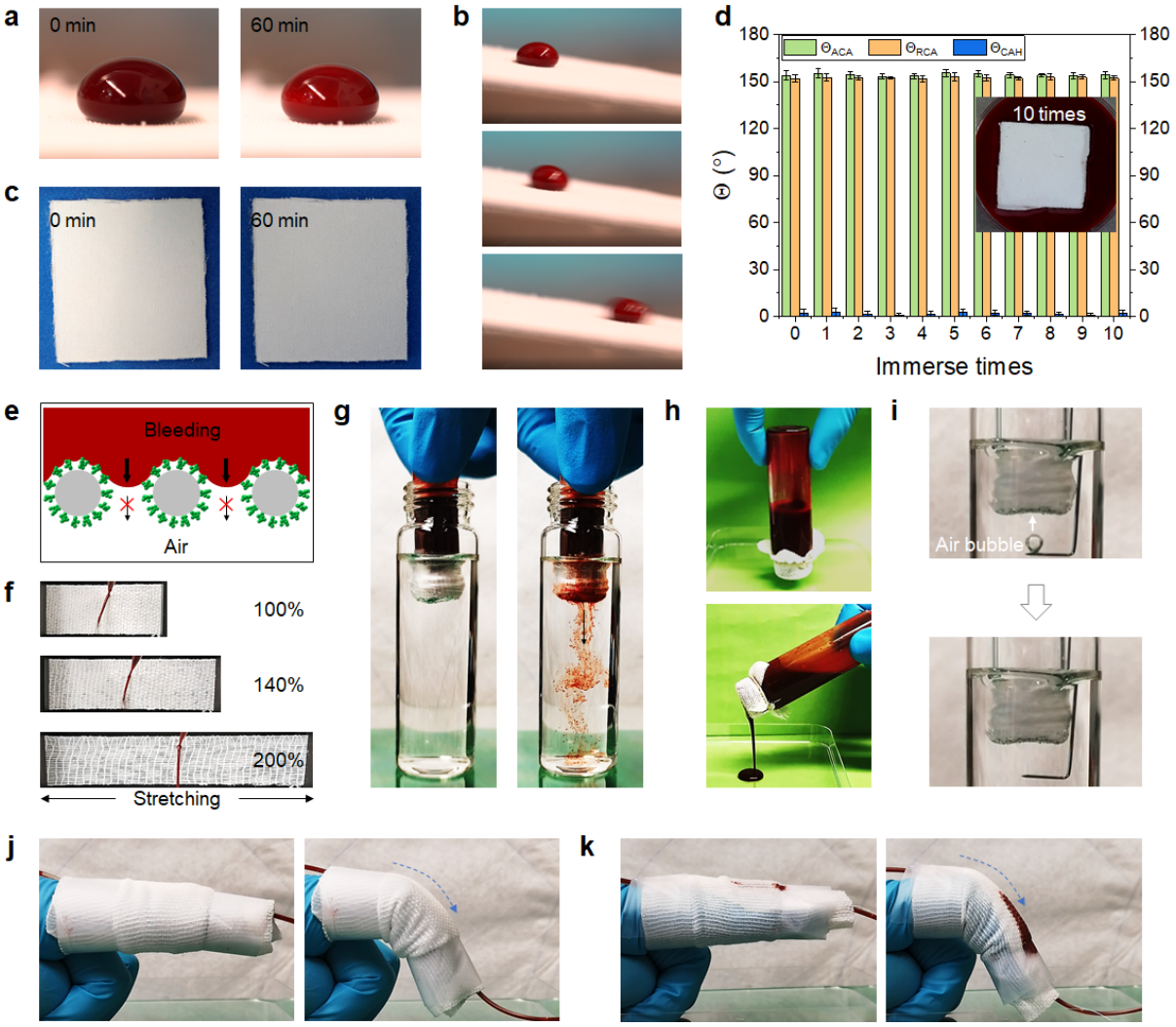

Figure 4.4 Hemostasis ability of wound dressing modified with the PDMS/TiO_2 composite film. a) Images of a 100 µL of blood droplet on PDMS/TiO_2-coated textile for 1 h. b) Sliding of blood droplet (100 µL) after deposition on the coated textile for 1 h. c) Photos of the coated textile before and after removal of the blood droplet. d) Advancing and receding contact angles of a sessile drop of human blood on a coated textile before and after immersing in blood for one time (1 h) or multiple times. e) Schematic illustration of the hybrid structure on the textiles coated with PDMS/TiO_2 composite film preventing blood permeation. The gray circle: structure of gauze; red part: blood; green part: structure of PDMS/TiO_2. f) Repellency of blood (red stripe) flowing on modified gauzes at different elongations. g, h) Shielding ability of the modified gauze avoiding blood leakage in water (g) or air (h). i) Air permeability of the modified gauzes under water. j, k) A polyvinyl chloride tube with a small incision is used to mimic bleeding, showing stable shield ability of modified gauzes under joint movement.

exposed to blood (**Figure 4.4**e). The intermittent nanostructures and air cushion greatly reduce the contact area between blood and surface. **Figure 4.4f** demonstrated

mechanical stability of blood repellency of the PDMS/TiO_2 film modified textiles when stretched. No blood adhesion was observed after impacted by blood flow, even when stretched by 200%. The stability of the PDMS/TiO_2 films was further evaluated by a deformation test (**Figure S4.10** in **Appendix II**). The blood repellency of the modified textiles was maintained even after twisting for tens of times.

The PDMS/TiO_2-modified textiles exhibited several additional advantages. Blood leakage from the test vial can be prevented by using the PDMS/TiO_2-modified textiles for at least 3 h (**Figure 4.4**g, h, and **Figure S4.11** in **Appendix II**). In contrast, the blood can easily penetrate the unmodified textiles and leak from the test vial. The blocking effect of blood effectively may reduce the unexpected loss of blood from a wound. In addition, the PDMS/TiO_2-modified textiles exhibited good air permeability in a water environment (**Figure 4.4i**). The air bubble injected with a needle was rapidly adsorbed by the film. Efficient air permeability may provide sufficient oxygen for promoting wound healing.[311] To mimic a bleeding wound, a blood-loaded PVC tube with a small incision was bandaged with medical gauzes with/without modification with PDMS/TiO_2 composites and fixed to the joint of forefinger. In contrast to a continuously bleeding bandaged up with an unmodified gauze (**Figure 4.4k**), the wound bandaged up with the PDMS/TiO_2-modified gauze efficiently inhibited bleeding during joint bending (**Figure 4.4j**).

4.4 Conclusions

In this chapter, the preparation of elastic, superhydrophobic and photocatalytically active composite films on various substrates from TiO_2 nanoparticles and PDMS was demonstrated. The PDMS/TiO_2 composite films exhibited excellent repellency to water and blood due to the superhydrophobic features. Blood droplets dried on the PDMS/TiO_2-modified surface showed low adhesion to the surface and were easily

removed. The elasticity of the composite films provided superior mechanical stability of blood repellency of the modified substrates. A mimicked 'joint bleeding' can be inhibited by the PDMS/TiO_2-modified medical gauzes even during joint movement. The photocatalytic activity of the composite film resulted in additional self-cleaning and antibacterial properties when exposed to UV light. The superhydrophobicity of the surface can be restored by UV illumination even after fouled with the organic contaminant. Besides, the PDMS/TiO_2 composite films enhanced the antibacterial efficiency under UV illumination. Given these specific properties, the PDMS/TiO_2 composite films serve as a good candidate coating for wound dressings, reducing blood loss, clot-gauze composite formation and bacterial infections.

4.5 Appendix II

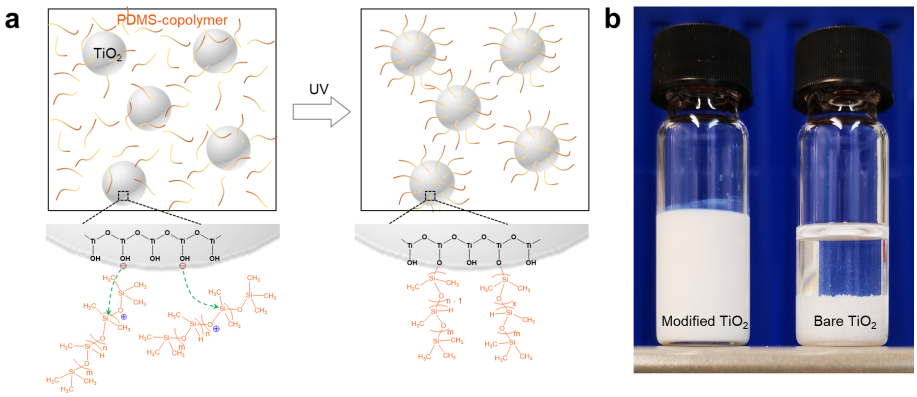

Figure S4.1 a) Schematic illustration of the modification of TiO_2 nanoparticles with PDMS-copolymer. Under UV light illumination, PDMS-copolymer was grafted of on TiO_2 nanoparticles. b) Photos of the dispersion of PDMS-copolymer modified TiO_2 nanoparticle (left) and precipitate of unmodified TiO_2 nanoparticles (right) in toluene solution (7 wt%). The photos were taken after 8 h.

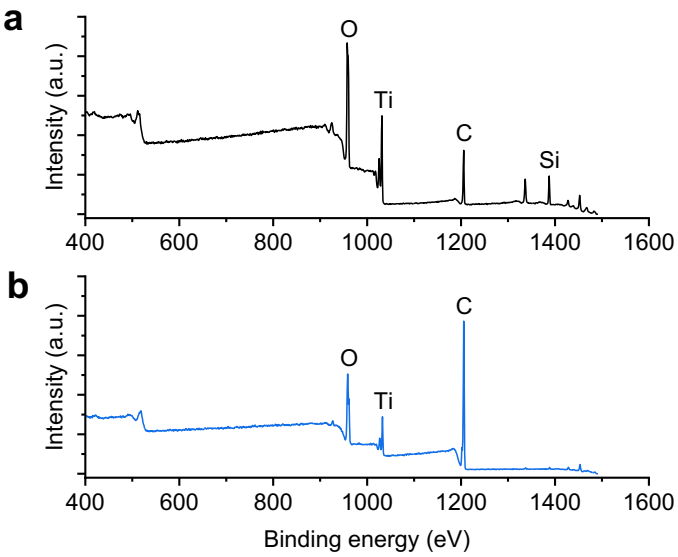

Figure S4.2 X-ray photoelectron spectrums of TiO_2 nanoparticles a) after and b) before PDMS-copolymer modification. Silicon element was detected on the surface of the PDMS-copolymer modified TiO_2 nanoparticles.

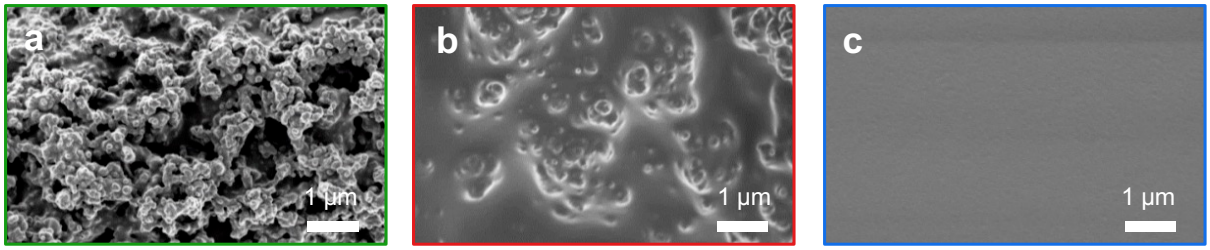

Figure S4.3 Scanning electron microscopy images of the surfaces coated with a) modified TiO_2 nanoparticles ($m_{modified\ TiO2}/m_{vinyl\text{-}PDMS}$ =0.1, $V_{solvent}/V_{vinyl\text{-}PDMS}$ = 3), b) unmodified TiO_2 nanoparticles ($m_{unmodified\ TiO2}/m_{vinyl\text{-}PDMS}$ =0.1, $V_{solvent}/V_{vinyl\text{-}PDMS}$ = 3) with 1 wt% PDMS-copolymer, c) and 1 wt% PDMS-copolymer without TiO_2 nanoparticles.

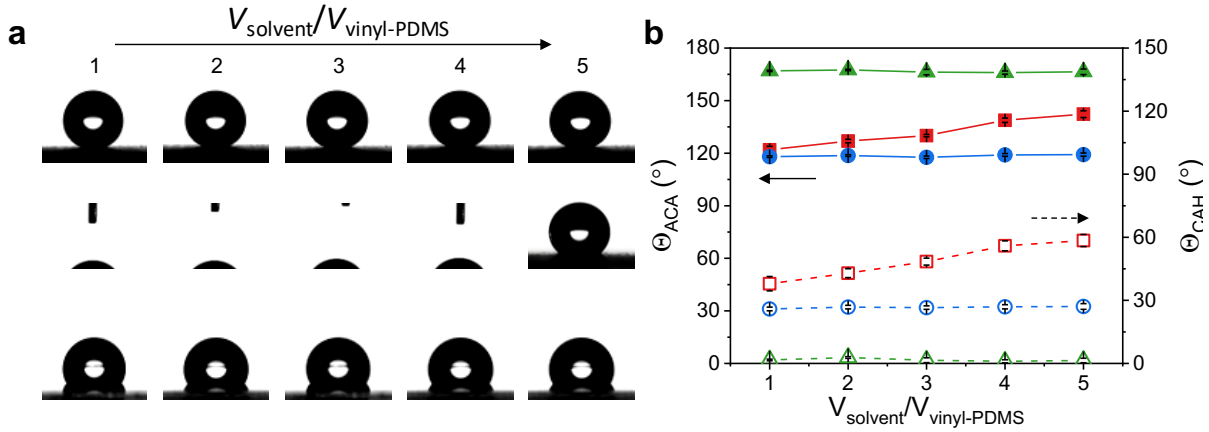

Figure S4.4 a) Optical photos of water drops (5 µL) on the surfaces prepared with the modified TiO_2 nanoparticles (top, $m_{TiO2}/m_{vinyl\text{-}PDMS}$ = 0.1), unmodified TiO_2 nanoparticles with 1 wt% PDMS-copolymer (middle, $m_{TiO2}/m_{vinyl\text{-}PDMS}$ = 0.1), and 1 wt% PDMS-copolymer (bottom). The solvent volume fraction was changed. b) Advancing contact angle (Θ_{ACA}) and contact angle hysteresis (Θ_{CAH}) of water droplet on surfaces corresponding to those in (a). The surfaces prepared with the modified TiO_2 nanoparticles showed superior superhydrophobicity with ultra-low hysteresis to water (Θ_{ACA} = 166° ± 1°, Θ_{CAH} < 2°, Θ_{ACA}: ▲, Θ_{CAH}: △). For the surfaces prepared with unmodified nanoparticles, the advancing contact angles (■) increased from 120° to 140° and failed to attain superhydrophobicity. The contact angle hysteresis (□) to water was even higher than pure PDMS surface (○). The pure PDMS surface showed stable advancing contact angle (●) around 120° and contact angle hysteresis around 30°.

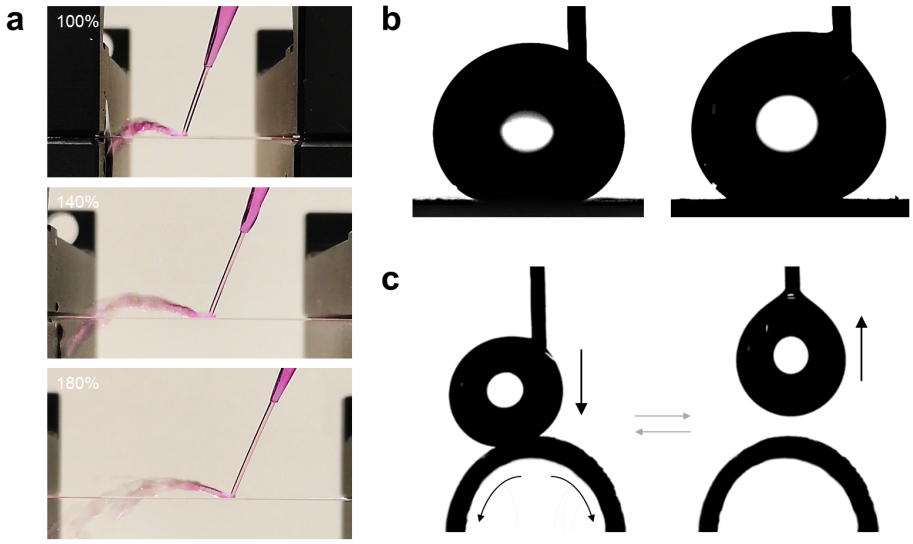

Figure S4.5 a) Images showing water flow impacting on the PDMS/TiO_2 composite film coated polyurethane (PU) surface at different stretching elongation from 100% to 140%, 180% (from top to bottom). b) The shape of water drops when receding on the PU surface with the elongation of 140% (left) and 200% (right). The PDMS/TiO_2 composite film coated PU surface lost superhydrophobicity at the elongation of 200% (Θ_{CAH} increased from 1° to 15°). c) Pressing and withdrawing of a 5 μL water drop on the bended PU surface coated with PDMS/TiO_2 composite film.

Figure S4.6 Young's modulus and hardness of PDMS/TiO_2 composite film before and after calcination at 500 °C for 30 min.

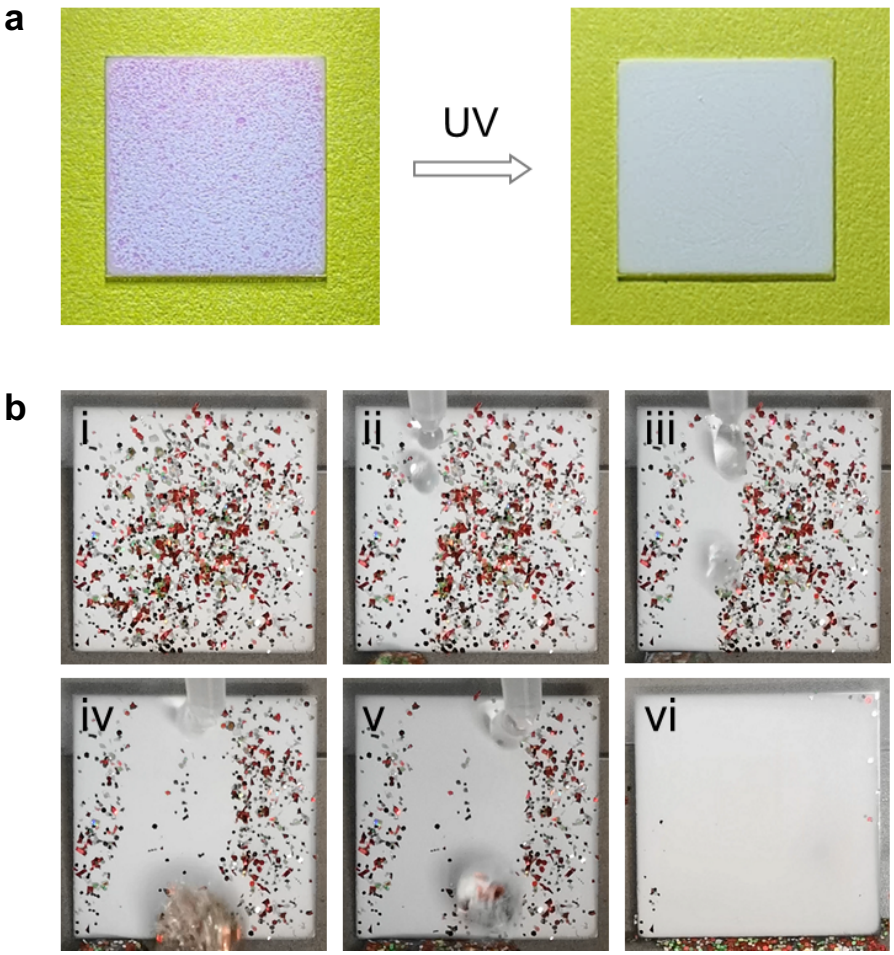

Figure S4.7 Demonstration of self-cleaning properties of the PDMS/TiO_2 composite films after contamination with organic chemicals and inorganic particles. a) Nile red on the PDMS/TiO_2 composite film was degraded by UV illumination after 2 h. b) Inorganic particles on the PDMS/TiO_2 composite film were removed by water.

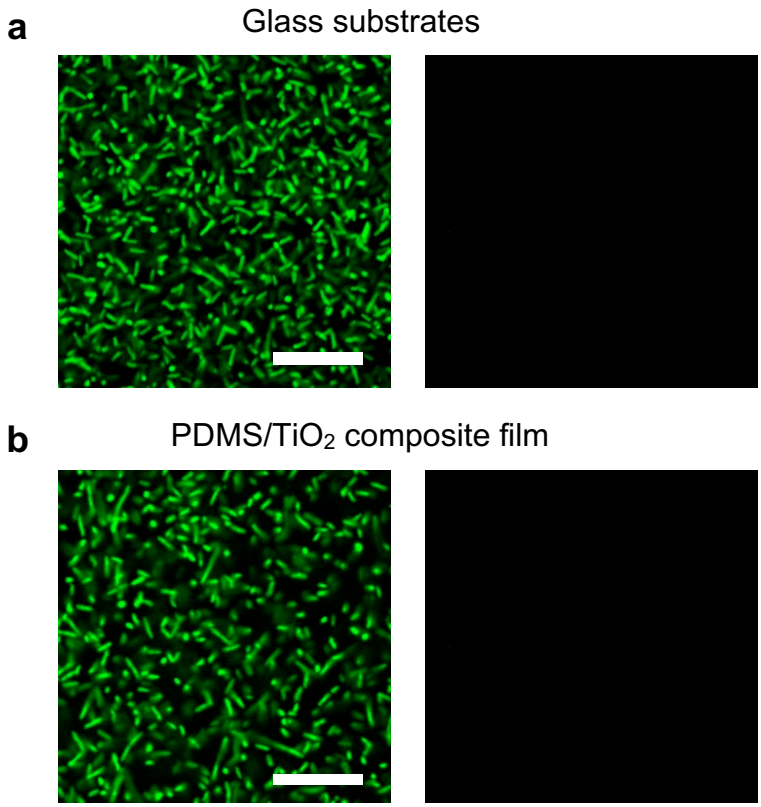

Figure S4.8 Confocal laser scanning microscopy images of *E. coli* on a) glass substrates and b) PDMS/TiO_2 composite films after incubation for 210 min in dark. Scale bar: 20 μm.

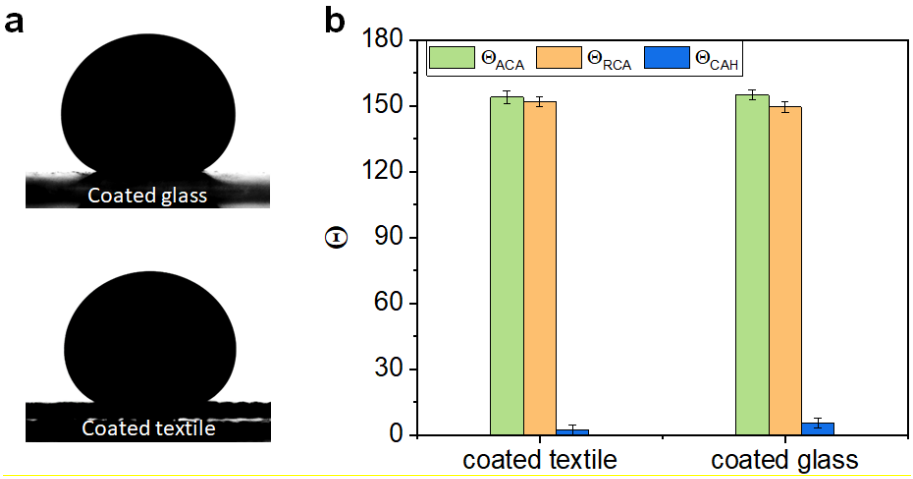

Figure S4.9 The wettability of blood on the PDMS/TiO_2 coated surfaces. a) Images showing static blood drops (10 μL) on coated glass and textile. b) Advancing (Θ_{ACA}) and receding (Θ_{RCA}) contact angles as well as the contact angle hysteresis (Θ_{CAH}) of blood on coated glass and textile.

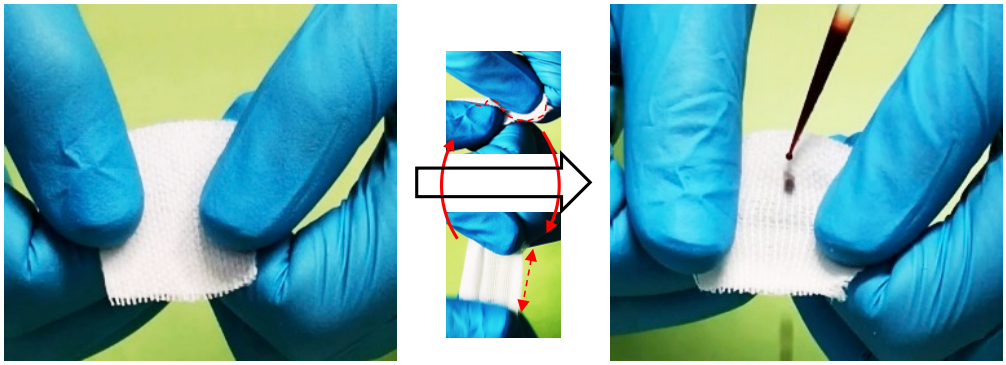

Figure S4.10. Twisting and stretching of the PDMS/TiO_2 modified textiles. The textiles maintained the repellency to blood-flow even after tens of times of deformation.

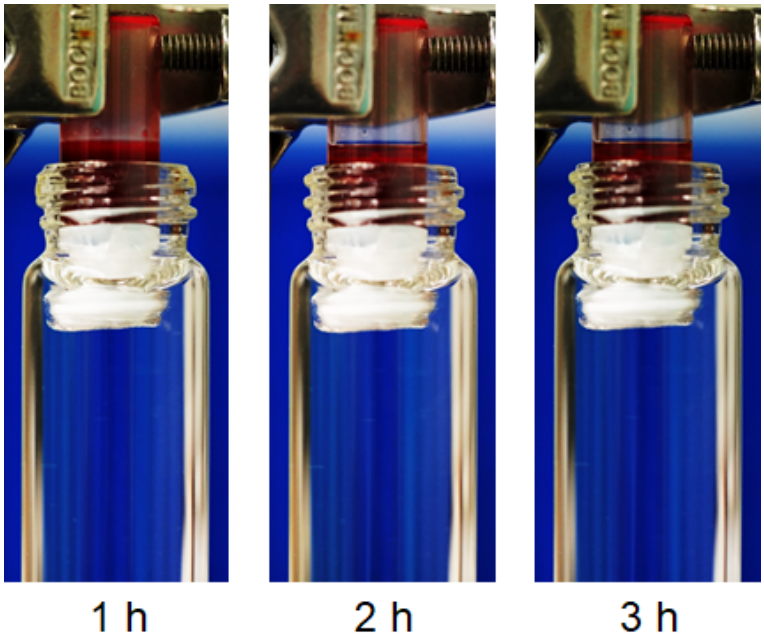

Figure S4.11 Demonstration of the capability of the PDMS/TiO_2 modified textiles preventing blood leakage into the water for at least 3 h.

Chapter 5

Carbon Nanotube-Hydrogel Composites Facilitate Neuronal Differentiation while Maintaining Homeostasis of Network Activity§

It is often assumed that carbon nanotubes (CNTs) stimulate neuronal differentiation by transferring electrical signals and enhancing neuronal excitability. Given this, CNT-hydrogel composites are regarded as potential materials able to combine high electrical conductivity with biocompatibility, and therefore promote nerve regeneration. However, whether CNT-hydrogel composites actually affect neuronal excitability and differentiation and how they do so remain elusive. In this chapter, CNT-hydrogel composites were prepared by in situ polymerization of poly(ethylene glycol) around a preformed CNT meshwork. It is found that the composites facilitate long-term survival and differentiation of pheochromocytoma 12 cells. Adult neural stem cells cultured on the composites showed an increased neuron-to-astrocyte ratio and higher synaptic connectivity. Moreover, primary hippocampal neurons cultured on composites, maintained morphological synaptic features as well as their neuronal network activity evaluated by spontaneous calcium oscillations, which were comparable to neurons cultured under control conditions. These results indicate that the composites are promising materials that could indeed facilitate neuronal differentiation while maintaining homeostasis of neuronal excitability.

§ This chapter is a slightly modified version of the following article:[312]

L. Ye, H. Ji, J. Liu, C. -H. Tu, M. Kappl, K. Koynov, J. Vogt, and H. -J. Butt. *Adv. Mater*. **2021**, DOI:10.1002/adma.202102981.

Author Contributions: L. Y. conceived the idea of this project, performed the material preparations, characterizations and analyses, and participated in the cell experiments. H. J. performed the cell experiments. K. K., J. V., and H. -J. B. supervised the project. L. J., C. -H. T., and M. K. participated in sample characterizations and analyses. L. Y., H. J., K. K., J. V., and H. -J. B. wrote the manuscript.

5.1 Introduction

Developing biomaterials capable of promoting neuronal differentiation, regrowth and formation of local and long-range axonal connections is of great importance for the development of new clinical technologies to tackle neuronal injury.[313-315] Conductive scaffolds have been reported to transfer electrical signals from the extracellular matrix to cells and to stimulate neuronal differentiation under electrical stimulation.[40, 41] In this respect, carbon nanotubes (CNTs) and their analogs with high electrical conductivity are promising materials.[316, 317] The thin films of CNT meshwork (usually coated on substrates) with organized fractal-like nanostructures were reported as good substrates for neuronal growth and long-term survival.[318-321] Moreover, there are reports that neurons on CNT meshwork exhibit enhanced signal transmission.[44, 45, 322] Such an enhancement in network activity has also been reported for neurons on graphene (an analog of CNTs),[234, 323] although it remains controversial.[324] It is assumed that the contact and interaction between CNTs (or graphene) and the cell membrane can improve neuronal excitability by modifying membrane potential.[45, 234] Based on these findings, CNTs and their analogs have rapidly become of interest to the material science community in the design of novel materials in nerve tissue engineering.[42, 43, 325, 326]

Although CNTs are usually reported as non-cytotoxic to neurons, some essential issues need to be carefully addressed before in vivo applications. First, the direct exposure and potential accumulation of CNTs in human tissue, which may cause abnormal immune cell activation and fibroblast proliferation, are of great concern.[317] These risks can be greatly reduced by incorporating CNTs as fillers into a hydrogel matrix. Some hydrogel-based materials have very good biocompatibility and exhibit great potential in biomedical fields such as drug delivery,[186, 327] biosensors,[328] and

tissue engineering.[329, 330] Therefore, CNT-hydrogel composites are often regarded as potential materials which combine electrical conductivity with biocompatibility promoting nerve regeneration.[42, 224, 331-333] Second, the neuronal excitability boosting caused by CNTs, which is often assumed to promote neuronal regeneration, could actually cause detrimental consequences to the nervous system. For instance, spinal cord injury leads to an increase in the excitability in the motoneurons below the lesion, causing a common debilitating complication, *e.g.,* spasticity.[334] Excessively increased neuronal excitability will also inhibit axonal elongation and dampen regional brain connectivity.[335] Moreover, hyper-excitability of cortical circuits may lead to neuropsychiatric disorders, *e.g.*, epilepsy.[336, 337] Therefore, the homeostatic properties of neuronal excitability, namely maintaining a target level of electrical activity, are of great significance in processes ranging from memory storage to activity-dependent neuronal development.[338]

In this regard, CNT-hydrogel composites where CNTs are embedded within the hydrogel matrix might serve as biocompatible conductive scaffolds while having less effect on modifying intrinsic neuronal excitability due to the reduced contact between CNTs and cell membranes. The CNT-hydrogel composites were reported to stimulate neurite outgrowth of model cell line pheochromocytoma 12 (PC12) cells under electrical stimulation.[224, 331] Moreover, it has been recently reported that the differentiation of PC12 cells,[42, 332] dorsal root ganglia,[332] and stem cells[333] can be enhanced on CNT-hydrogel composites even without the presence of exogenous electric fields. However, the underlying mechanism remains elusive. Enhanced excitability of electrical activity was often assumed as vital in stimulating neuronal differentiation, although there is no concrete evidence supporting this so far.[42, 43, 326] Moreover, higher electrical activity as shown by increased Ca^{2+} transients during

neuronal development may greatly impede neuronal maturation leading to growth cone stalling and axonal retraction.[339]

Most of the existing studies focus on the expression of cell phenotypes and are largely based on PC12 cells. At the same time, the effect of CNT-hydrogel composites on neurogenesis and neuronal excitability remains largely unexplored. The underlying question is whether the CNTs embedded in hydrogels could indeed affect neurogenesis and neuronal excitability. Moreover, CNT-hydrogel composites are usually prepared in aqueous solutions and CNTs need to be pre-functionalized to improve dispersion.[222] In this study, a type of CNT-poly(ethylene glycol) (PEG) hydrogel composites has been prepared using a newly developed simple and versatile method, which does not require pre-functionalization of CNTs. To gain a deeper understanding on the effect of the composites on neuronal development, the differentiation of PC12 cells and neurogenesis of adult neural stem cells (NSCs) were investigated. Moreover, the network activity on composites was studied using primary hippocampal neurons.

5.2 Experimental

Materials and Sample Preparation. Poly(ethylene glycol) diacrylate (average M_n = 575 Da), 2-hydroxy-2-methylpropiophene (D1173, 97%), 3-(trimethoxysilyl)propyl acrylate (92%), and 1-hexyl-3-methyl-imidazolium bis(trifluoromethyl sulfonyl)imide (T_g = – 9 °C) were purchased from Sigma-Aldrich. CNTs (multiwalled, outside diameter = 18 – 28 nm, length = 10 – 30 μm, > 96%, 1.7% –OH, 98 S cm^{-1}) were purchased from Nanografi Nano Technology. Microscope glass slides (No. 1.5H) were purchased from Thermo Fisher Scientific. The cover slides were pre-modified by immersing them into a solution of 2 % (v/v) 3-(trimethoxysilyl)propyl acrylate in ethanol overnight, followed by rinsing with ethanol and drying with nitrogen gas. Poly(L-lysine) (PLL)-coated glass

substrates were used as the control. All the samples were pre-treated by immersing them into an aqueous solution of 0.1 wt% PLL (Sigma-Aldrich) at 4 °C overnight.

Viscoelastic Properties. The viscoelastic properties of the precursors were measured by a DHR-3 rheometer (TA Instruments). A 1° cone – plate geometry with a diameter of 40 mm was used. The sample thickness was around 1 mm. A strain amplitude sweep was performed first, in order to define the linear viscoelastic zone. The storage modulus, loss modulus and complex viscosity were obtained by a frequency sweep carried out at room temperature within the range of 0.1 – 100 rad s^{-1}.

Surface Morphology. The samples were gradually dehydrated and dried at ambient temperature. The surface morphology of the samples was captured by scanning electron microscopy (Zeiss, LEO Gemini 1530) with an accelerating voltage of 3 kV.

Surface Modulus. The samples were placed in a Petri dish which was filled with Milli-Q water (18.2 MΩ · cm). The surface modulus was measured using an Asylum MFP-3D nanoindenter (Oxford instruments). A spherical indenter made of sapphire was used with a radius of 0.5 mm. The indentation was done under force control. After touching the sample surface with a threshold force of 5 – 10 μN, the force was ramped up to 200 μN within 5 s, then held at 200 μN for 5 s, and then reduced to 0 μN within 5 s again. Indentation curves were fitted using the Hertz model, assuming a sample Poisson ratio of 0.5 for the polymer.

Surface Topography. The samples were placed in a Petri dish which was filled with Milli-Q water (18.2 MΩ · cm). The surface topography was captured using atomic force microscopy (JPK NW III, QI mode) under water. The cantilever with a CONT-W tip (NanoWorld) at the very end was used. The resonant frequency of the cantilever is 13 kHz (9 – 17 kHz). The spring constant of the cantilever is 0.2 N m^{-1} (0.07 – 0.4 N m^{-1}). The RMS surface roughness were analyzed by free software, Gwyddion (v2.56).

Immunostaining. Cells for imaging and analysis were fixed in 4% paraformaldehyde (PFA) at 4 °C for 30 min followed by washed with PBS for three times and were blocked with 10% normal goat serum and 0.2% Triton-X 100 for 1 h at room temperature. Then, cells were incubated with primary antibodies at 4 °C overnight followed by washing with PBS, and further stained with Alexa-labeled secondary antibodies (Invitrogen, 1:1000 dilutions) for 1 h at room temperature and finally with 4′, 6-diamidine-2′-phenylindole dihydrochloride (DAPI, Invitrogen, 1:20000 dilutions) to visualize cell nuclei.

Cell Viability and Cytotoxicity, and Focal Adhesion. PC12 cells (6×10^4 cells cm^{-2}) were plated and maintained in DMEM (Invitrogen) supplemented with 10% FBS, 0.1 mM minimum essential medium non-essential amino acids (MEM-NEAA; Invitrogen), 2 mM L-glutamine (Gibco), 100 U mL^{-1} penicillin and 100 μg mL^{-1} streptomycin. For cell viability, cells were fixed and stained with α/β-Tubulin Antibody (Cell signaling, #2148, 1:2000) after culturing for 24 h, 48 h and 72 h, and the cell number was calculated. For cell apoptosis, the cells (48 h) were stained with cleaved Caspase3 (a marker for dead cells). Cleaved Caspase3 positive cells were counted. For analysis of focal adhesion, the medium was replaced with 2.5% FBS culture medium after 24h and maintained for another 48 h. Primary antibodies were used for immunostaining as following: Phospho-FAK (pY397) antibody (Cell signaling, #3283S, 1:2000); Paxillin antibody (Thermo scientific, MA5-13356, 1:1000). To visualize F-actin, cells were further stained with Alexa Fluor™ 568 Phalloidin (Thermo scientific, A12380, 1:1000).

Protein Adsorption. Samples with a diameter of 2 cm were placed in a 6-well plate, and each well was filled with 2 mL of 1 wt% bovine serum albumin (BSA) solution in phosphate-buffered saline (PBS, pH 7.4, Sigma). The samples were left to allow for protein adsorption at ambient temperature (22 °C) for 1 h while stirring in an orbital

shaker at 90 rpm. Then, the samples were rinsed 3 times with PBS and placed into 1.5 mL of 1 wt% SDS solution for 24 h to thoroughly extract BSA from the samples. The BSA concentration in the SDS solution was analyzed with Micro BCA™ Protein-Assay-Kit (Thermo Scientific, 23235).

Differentiation of PC12 cells. PC12 cells were plated at a low density (1×10^4 cells cm^{-2}) in DMEM (Invitrogen) supplemented with 10% fetal bovine serum (FBS), 0.1 mM minimum essential medium non-essential amino acids (MEM-NEAA; Invitrogen), 2 mM L-glutamine (Gibco), 100 U mL^{-1} penicillin and 100 µg mL^{-1} streptomycin. The medium was replaced with DMEM (Invitrogen) supplemented with 2.5% FBS, 0.1 mM minimum essential medium non-essential amino acids (MEM-NEAA; Invitrogen), 2 mM L-glutamine (Gibco), 100 U mL^{-1} penicillin and 100 µg mL^{-1} streptomycin after 16 h. Cells were retained for 12 days for subsequent analysis.

Proximity Ligation Assay. PC12 cells were plated on the control and c-PEG-20 samples in DMEM medium containing 10% FBS at about 40% confluence. 6 h later, cells were transfected with CAG-integrin β1-HA-ires-GFP plasmid, in which an HA tag was added to the intracellular N-terminal of integrin β1. 24 h later, the medium was replaced with 2.5% FBS culture medium and the cells were cultured for another 24 h. Cells were fixed with 4% PFA followed by blocking with blocking solution and were incubated with primary antibodies at 4°C for overnight. Then the incubations with the PLA probes (anti-mouse and anti-rabbit IgG antibodies conjugated with oligonucleotides), ligation and amplification according to the user manual of Duolink® Proximity Ligation Assay (sigma). The following primary antibodies were used for PLA: HA-Tag (Cell signaling, 6E2, #23671:1000), FAK Antibody (Cell signaling, #3285, 1:1000) and Phospho-FAK (Tyr397) Antibody (Cell signaling, #3283, 1:1000), Paxillin Antibody (Cell signaling, #2542, 1:1000), Phospho-Paxillin (Tyr118) Antibody (Cell

signaling, #2541, 1:1000) and Talin-1 Antibody (Cell signaling, C45F1, #4021, 1:1000). Imaging was obtained on a Leica SP8 confocal laser scanning microscope. Quantitative analysis was performed by counting PLA positive dots per cell.

Western Blotting. PC12 cells were plated on PLL-coated glass slides and c-PEG-20 samples in DMEM medium containing 10% FBS. 24h later, the medium was replaced with 2.5% FBS culture medium and cells were cultured for another 48 h. Then the medium was removed, and cells were washed gently by ice cold PBS. Cells were lysed on ice by adding 100 µL RIPA buffer (50 mM Tris-HCl (pH 7.5). 150 mM NaCl, 1 mM EDTA, 1% Triton X-100 and 0.1 % SDS) supplemented with protease inhibitor (cOmplete™ Protease Inhibitor Cocktail, Roche) and phosphatase inhibitor (PhosSTOP™, Roche). WB was performed according to standard procedures. Briefly, samples were separated by 10% SDS-PAGE and blotted on a nitrocellulose membrane (0.45 µm, BIO-RAD, USA). Then the membrane was blocked in 10% non-fat dry milk in PBS at room temperature for 1 h and was further incubated with primary antibodies in 1% non-fat BSA at 4 °C for overnight. The following primary antibodies were used: FAK Antibody (Cell signaling, #3285, 1:4000), Phospho-FAK (Tyr397) Antibody (Cell signaling, #3283, 1:4000) and ß-actin (MP Biomedicals, clone B4， 1:5000). After three washes, membranes were incubated with a corresponding secondary fluorescent antibody (IRDye® 800CW Goat anti-Rabbit IgG Secondary Antibody or IRDye® 800CW Goat anti-Mouse IgG Secondary Antibody) at 1:10000 dilution. Immunofluorescent bands were detected using Fusion FX Spectra machine. Quantification of immunosignals was adjusted to ß-actin as loading control and was performed using ImageJ (Fiji).

Differentiation of Adult Neural Stem Cells. Adult neural stem cells culture was prepared from the lateral wall of the subventricular zone (SVZ) of young adult (8 − 12 weeks)

C57/Bl6 mice. Prior to commencing the culture, plates were coated with 0.1% (w/w) poly(D-lysine) (Sigma-Aldrich) and Laminin (5 µg mL^{-1}, Sigma) at 4°C overnight. After anesthetizing the mice according to the appropriate institutional guidelines and performing cervical dislocation, the mouse brain was quickly removed and put into the ice-cold Hank's Balanced Salt Solution (HBSS, Gibco) medium. The thin layer of tissue surrounding the ventricle was carefully dissected and stored in HBSS medium on ice. Thereafter, the tissue was digested in pre-warmed 0.05% Trypsin-EDTA in HBSS for 10 min in a water bath at 37 °C, followed by centrifugation at 300 x g for 5 min, discarding the supernatant. Then, the tissue was washed twice with growth medium, which is composed of Neural Basal Medium A (Invitrogen) with 2% B27 (Invitrogen), 1× GlutaMAX (Invitrogen). The tissue was suspended again in 2 mL of growth medium and dissociated by gently pipetting up and down approximately 10× using a P1000 pipette, followed by passing the cell suspension through a 40 µm sieve to remove debris and un-dissociated tissue clumps.

The resulting cell suspension was plated onto the poly(D-lysine)/laminin coated plates, maintained in growth medium supplemented with 20 ng mL^{-1} purified mouse receptor-grade epidermal growth factor (EGF, Sigma) and 20 ng mL^{-1} recombinant bovine fibroblast growth factor (FGF-2, Sigma). At this stage, the yield of adult neural stem cells was very low. EGF and FDF-2 stimulate stem cell proliferation and yield enough quantities of adult neuronal stem cells for subsequent experiments. For the differentiation, equal amounts of stem cells were plated on the samples and maintained growth medium with EGF and FDF-2. When the cells reached approximately 80% confluency, the growth medium was replaced with a medium containing 5 ng mL^{-1} FGF and 0 ng mL^{-1} EGF. Following 2 days in 5 ng mL^{-1} FGF, the medium was replaced again with a growth medium in the absence of EGF and

FDF-2. Cells were retained for ~ 5 weeks for subsequent analysis. Primary antibodies were used for immunostaining as following: MAP2 antibody (Sigma, #HPA012828, 1:2000) for neurons, GFAP antibody (Sigma, #G6171, 1:2000) for astrocytes.

Primary Culture of Hippocampal Neurons. Hippocampi from C57BL/6J mouse embryos at embryonic day (E17) were dissected and incubated in HBSS supplemented with 0.05% trypsin for 15 min at 37 °C. Then the hippocampi were washed twice and dissociated in a plating medium (MEM, Invitrogen) supplemented with 10% horse serum, 100 U mL^{-1} penicillin and 100 µg mL^{-1} streptomycin (Gibco), 0.6% glucose (Fresenius Kabi) using Pasteur pipettes with polished tips. Neurons (1 x 10^5 cells per cm^2) were seeded on the samples and kept at 37 °C and 5% carbon dioxide (CO_2). Cells were gradually washed with PBS and incubated in a neurobasal medium (Invitrogen) supplemented with 2% B27 (Invitrogen), 100 U mL^{-1} penicillin, 100 µg mL^{-1} streptomycin (Gibco) and 0.5 mM L-glutamine (Gibco) after 3 h. The cells were retained for ~ 2 weeks and ~ 3 weeks for analysis and calcium imaging, respectively.

DNA Transfection. Lipofectamine® 2000 (Invitrogen) was used for DNA transfection. The complexes for transfection were prepared as follows: 4 µL of Lipofectamine® 2000 was diluted in 100 µL of Opti-MEM I Reduced Serum Medium and incubated for 5 min at room temperature. In parallel, 2.0 µg of DNA was diluted in 100 µL of Opti-MEM I Reduced Serum Medium and mixed gently. After 5 min incubation, the diluted DNA and diluted Lipofectamine® Transfection Reagent was mixed gently and incubated for 20 min at room temperature. The samples were placed in 6-well plates. 200 µL of complexes was added to each well and mixed gently by rocking the plate back and forth. The medium was replaced with fresh growth medium after 6 h. The cells were used 48 h post-transfection.

Sholl Analysis, and Spine Analysis. The neurons for Sholl analysis and spine analysis were transfected with the pAAV-hSyn-IRES-mCitrine plasmid visualizing cell morphology (see *DNA transfection* above). Cells were fixed and stained with a GFP antibody 2 days after transfection. Fluorescent images were captured by confocal laser scanning microscopy (Leica SP8, and Zeiss LSM880). The images were quantified using ImageJ (Fiji). For Sholl analysis, a 20× objective (NA = 0.8) was used and Z-series stacks with a step distance of 1 µm were recorded. The Z-projected (Max intensity) was performed to converse the stacks into 2D images. The dendrites of neurons were traced with the semi-automated Simple Neurite Tracer plugin.[340] The tracers were saved as SWC (or Traces) files. The Sholl analysis was performed by the Sholl Analysis plugin using the SWC files with a step of 10 µm.[341] For spine analysis, a 63× oil objective (NA = 1.4) was used and Z-series stacks with a step of 0.2 µm were recorded. Spines were defined as dendritic protrusions from 0.5 µm up to 5 µm in length and were manually counted along a selected dendritic segment. For each dendritic segment, the number of spines per µm dendrite was calculated.

Calcium Imaging. Primary hippocampal neurons were incubated with 1 µM Rhod-4 AM (Abcam, #ab142780) for 30 min at 37 °C in 5% CO_2. The samples were washed and conditioned in 4-(2-hydroxyethyl)-1-piperazineethanesulfonic acid (HEPES)-buffered Krebs-Ringer solution (Avantor, J67795.AP, containing 120 mM sodium chloride, 5 mM potassium chloride, 2 mM calcium chloride, 1 mM magnesium chloride, 25 mM sodium bicarbonate, 5.5 mM HEPES, and 1 mM D-glucose, pH 7.2) for 30 min at 37 °C. The calcium imaging was performed by confocal laser scanning microscopy (Zeiss LSM880) equipped with an incubator (the temperature was equilibrated at 37 °C). A 20× Plan-Apochromat objective (NA = 0.8) was used. The excitation was done with a HeNe laser operating at 543 nm and the emitted fluorescence was

detected in the range from 560 to 700 nm. The fluorescent fluctuation of the regions of interest (soma) was recorded and analyzed by the ZEN v2.3 software (Zeiss). Changes in cytosolic calcium are shown as $(f - f_0)/f_0$, where f is the fluorescence intensity at soma over time, f_0 is the fluorescence intensity at the rest state.

5.3 Results and Discussion

In this work, an ionic liquid was used as a medium to prepare CNT-based hydrogel composites. Ionic liquids, known as 'green solvents' with negligible vapor pressure, have been reported to promote the dispersion of carbon nanomaterials in a polymer matrix or solutions even without functionalization.[160, 161, 164] The main advantage of combing CNTs and ionic liquids is that bucky gels containing CNT meshwork infused with large amounts of ionic liquids can be obtained by simply mixing using mechanical grinding. The entangled CNT bundles are exfoliated to provide finer bundles forming percolation networks in ionic liquids.[342, 343] The idea of the work is to transfer the in situ formed CNT network into a hydrogel matrix by in situ polymerization of suitable monomers in ionic liquids followed by solvent replacements. PEG is considered biocompatible, and its use in biomedical applications is well established. To prove the concept of the idea, CNT-PEG hydrogel composites were selected as a model system. Poly(ethylene glycol) diacrylate, which is well dissolvable in ionic liquids, was used as precursor for synthesizing PEG hydrogel matrix by polymerization and crosslinking under UV illumination.[344]

To prepare CNT-PEG hydrogels, CNTs (10, 20, 40 mg) of 10 – 30 μm lengths were mixed with 2 mL 1-hexyl-3-methyl-imidazolium bis(trifluoromethyl sulfonyl)imide by mechanical grinding for 30 min (**Figure 5.1**). Then, 0.5 mL poly(ethylene glycol) diacrylate containing 10% (v/v) 2-hydroxy-2-methylpropiophene as a photoinitiator was added to the mixtures by stirring. The final mixtures were stirred for > 2 h and

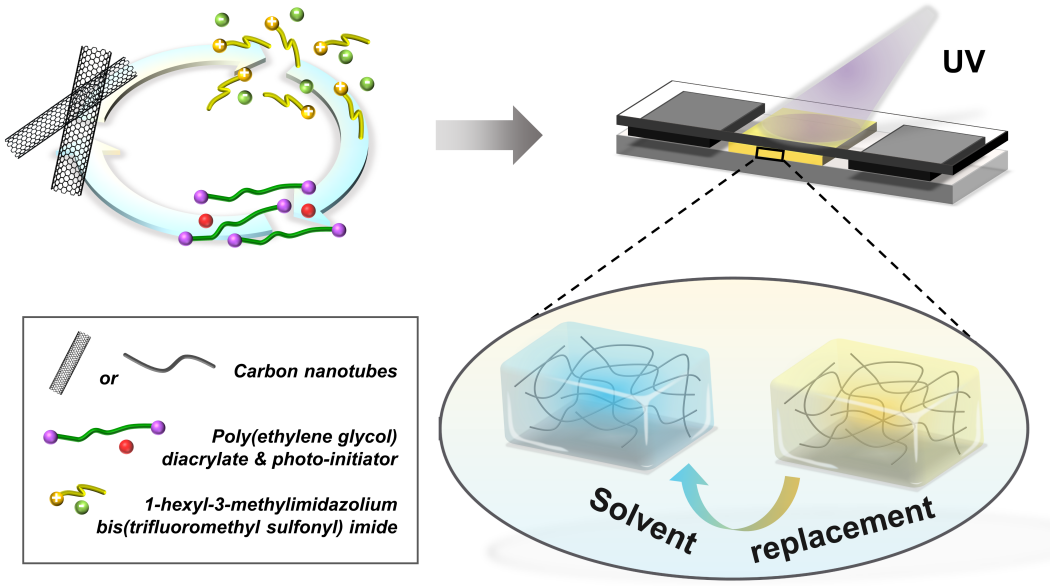

Figure 5.1 Schematic illustration on the preparation of CNT-PEG hydrogel composites. The CNTs were ground in 1-hexyl-3-methylimidazolium bis(trifluoromethyl sulfonyl) imide. Poly(ethylene glycol) diacrylate with photoinitiator was added to the mixtures and they were used as precursors. Then, the precursors were sandwiched between two glass slides with two cover slides (140 μm thick) used as spacers. The hydrogel composites with varying CNT content were prepared by UV-induced polymerization followed by solvent replacements.

used as precursors. 50 μL of the precursors were sandwiched between two glass slides and illuminated by UV light (365 nm, 250 mA) for a specific amount of time (10 – 240 s, **Table S5.1** in **Appendix III**) to make a composite film with a thickness of ~ 140 μm. The top cover slide was pre-modified with 3-(trimethoxysilyl)propyl acrylate to anchor the composite films covalently. The CNT-PEG hydrogel composites with varying CNT loading were obtained by replacing the ionic liquid with acetonitrile and then with water. The composites are denoted as c-PEG-*x*, where *x* is the initial concentration (w/v) of CNTs in the ionic liquid.

Before studying neuronal differentiation, the physicochemical properties of the composites were characterized. **Figure 5.2**a shows the frequency (ω) dependence of the real (G') and imaginary (G'') parts of the complex shear moduli of the precursors as measured by oscillatory shear rheology. The frequency response of the precursor

of pure PEG hydrogels reveals non-Newtonian liquid behavior. It is characterized by a typical terminal region with $G'(\omega) \sim \omega^2$, $G''(\omega) \sim \omega^1$. Upon incorporating the CNTs, a plateau with $G' > G''$ is observed at low frequencies in c-PEG-5 samples. It indicates the formation of weak CNTs percolation networks. For c-PEG-20 samples, $G' > G''$ over a wider range of frequency reflects the response of strong CNTs networks. The formation of CNTs percolation networks also resulted in a remarkable increase in the shear viscosity of precursors (**Figure S5.1** in **Appendix III**). The surface morphology of the composites was inspected by scanning electron microscopy. After dehydration, the composites showed some protrusions of CNTs through the top of the surface (**Figure 5.2**b, **Figure S5.2** in **Appendix III**).

The surface mechanics and topography of materials designed to mimic extracellular matrix have great impact on cell adhesion, migration and differentiation.[345, 346] The surface mechanics of the composites in water was investigated by a nanoindenter. The elastic modulus of the composites was obtained by fitting indentation curves (**Figure S5.3** in **Appendix III**) using the Hertz model. The elastic modulus of the composite samples varied from ~ 0.8 MPa (*i.e.,* c-PEG-5) to ~ 1.3 MPa (*i.e.,* c-PEG-0) (**Figure 5.2**c). It should be noted that the precursors with CNTs required longer exposure time to UV illumination for adequate crosslinking and mechanical strength. The prolonged illumination time were attributed to the reduction of polymerization efficiency resulting from the UV adsorption of CNTs, or the dark color of precursors.[347] Thus, the UV exposure time was tuned to achieve a comparable elastic modulus of the composite films (**Table S5.1** in **Appendix III**).

The surface topography of the composites in water was investigated using atomic force microscopy. Pure PEG hydrogels show a smooth surface (**Figure 5.2**d). The root mean square (RMS) roughness (30 μm × 30 μm) was ~ 3 nm (**Figure 5.2**d). Upon

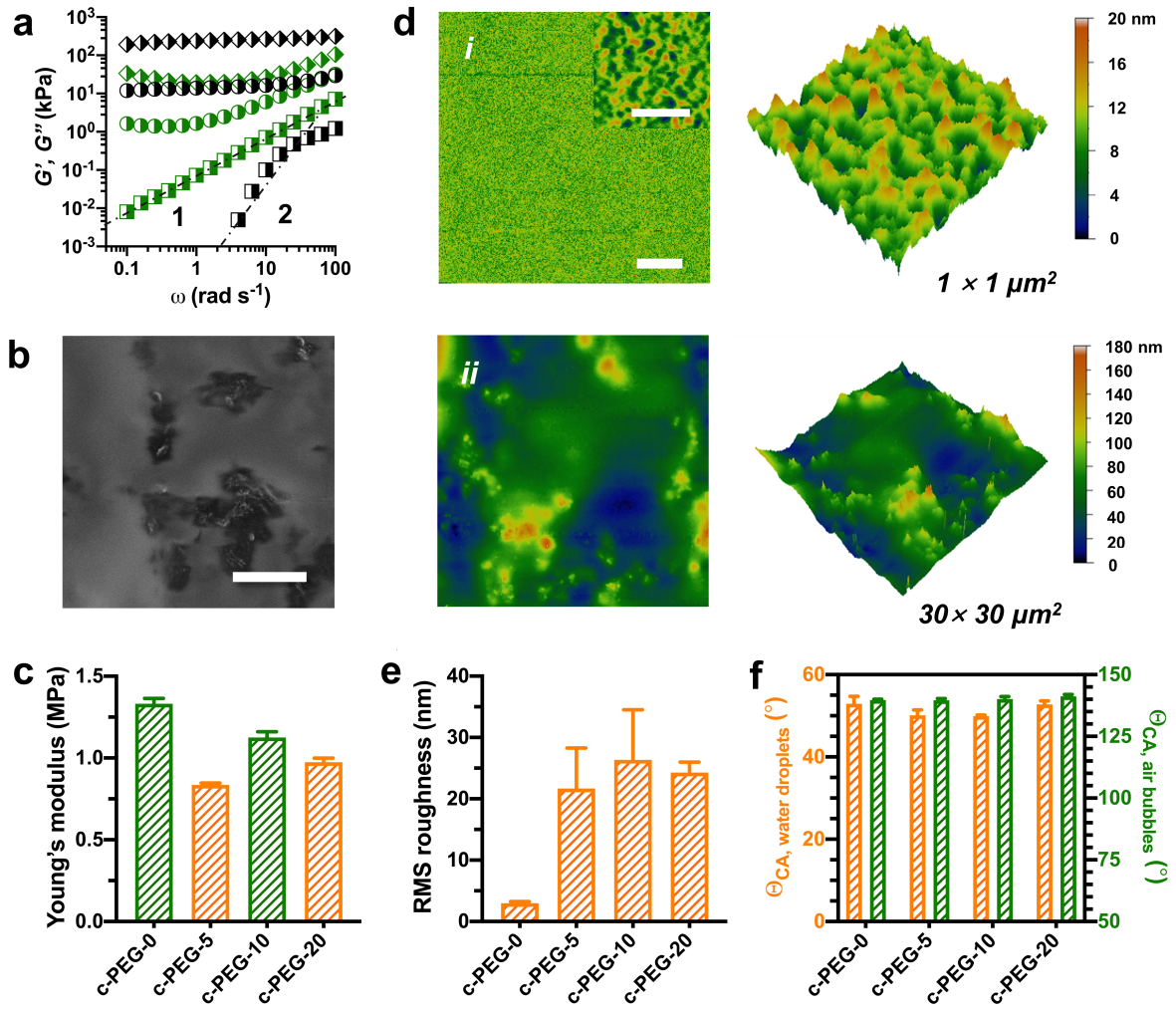

Figure 5.2 Characterization of CNT-PEG hydrogel composites. a) Storage modulus (*G'*, black) and loss modulus (*G''*, green) of the precursors of c-PEG-0 (◨), c-PEG-5 (◑), c-PEG-20 (⬗) samples. b) Scanning electron microscopy image of the surface of c-PEG-20 samples gently dehydrated at ambient temperature. Scale bar: 5 µm. c) Young's modulus of the composite samples obtained from the nanoindentation experiments. d) Surface topographies (2D and 3D height images) of c-PEG-0 (i) and c-PEG-20 (ii) samples captured in water by atomic force microscopy. Scale bar: 5 µm (inset: 500 nm). e) Root mean square (RMS) roughness of the surface (30 µm × 30 µm) of the composites. f) Apparent contact angles (Θ_{CA}) of water droplets in air (orange) and air bubbles underwater (green) on the surface of the composite samples. Bar graphs show mean ± SEM.

incorporating CNTs, the surface roughness of the composites increased significantly compared to pure hydrogels (**Figure 5.2**d, and **Figure S5.4** in **Appendix III**). The RMS roughness of c-PEG-20 samples was ~ 24 nm. This indicates the increase of surface

microstructures. No remarkable differences in surface roughness among the composite samples could be discerned (**Figure 5.2**e). Moreover, no significant difference in the apparent contact angle of water drops in air (or air bubbles under water) was observed (**Figure 5.2**f).

The effect of CNT-PEG hydrogel composites on neuronal differentiation was first investigated using PC12 cells. PC12 cells exhibited minimal cell viability after culturing on c-PEG-0 samples for 24 h (**Figure 5.3**a), which was attributed to the intrinsic cell repellent properties of pure PEG hydrogels due to their minimal protein adsorption (**Figure 5.3**b).[348] However, when compared to pure hydrogels, cell adhesion was increased on the composites. The cell viability increased with higher CNT loading but did not change further above c-PEG-10 samples. The results might indicate that CNTs in the composites enhance the adsorption of extracellular matrix proteins, as CNTs are prone to interact with many biomolecules.[321, 349] The protein adsorption of the composites was evaluated using bovine serum albumin. An increased adsorption of bovine serum albumin was observed when CNTs content was increased (**Figure 5.3**b). The cytotoxicity of the composites was evaluated by comparing cell viability (**Figure 5.3**c) and apoptosis (**Figure 5.3**d) of PC12 cells cultured on poly(L-lysine) (PLL)-coated glass substrates (as the positive control) and c-PEG-20 samples for different incubation periods (also see **Figure S5.5, S5.6** in **Appendix III**). These results point at minimal cytotoxicity of the composites.

The differentiation of PC12 cells was investigated by culturing them in a low-serum medium (containing 2.5% fetal bovine serum) where proliferation was inhibited while no exogenous neurotrophic factors were supplemented. After 12 days, PC12 cells could hardly be observed on pure hydrogels while cells on PLL-coated glass substrates differentiated to a minimal degree (**Figure 5.3**e,f). The differentiation of

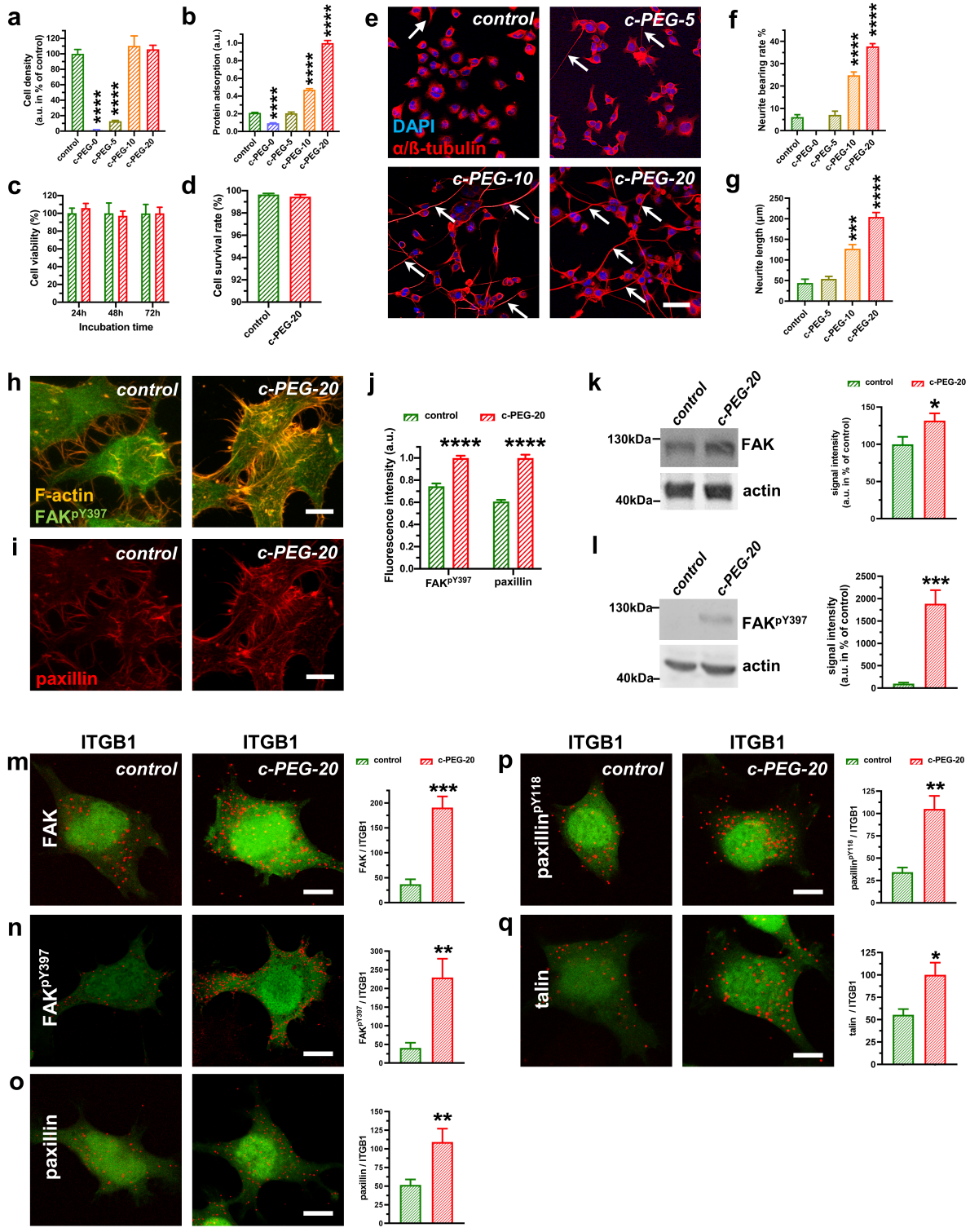

Figure 5.3 *Caption details see next page*.

PC12 cells was enhanced with increasing CNT content in the composites. For instance, cells cultured on c-PEG-20 samples exhibited a maximum 38 % proportion of cells bearing neurites (**Figure 5.3**f). No significant changes in the neurite bearing rate of

PC12 cells were observed when cells were cultured on a sample with even higher CNT loading (**Figure S5.7** in **Appendix III**). As discussed above, the protein adsorption was enhanced on the composites (**Figure 5.3**b). This points to the possibility that the adsorption of growth factors (*i.e.,* diffusible signaling proteins that stimulate cell growth, differentiation, *etc.*) secreted by the differentiated PC12 cells was enhanced when PC12 cells were cultured on the composites, a fact, which might contribute to long-term survival and differentiation.[321, 350]

Figure 5.3 Proliferation and differentiation of PC12 cells on poly(L-lysine) (PLL)-coated glass and CNT-PEG substrates. a) Cell density of PC12 cells after incubation on PLL-coated glass substrates (control) and different CNT-PEG composite samples (n = 7 for control and c-PEG-20, 3 for c-PEG-0, c-PEG-5 and c-PEG-10, 7 for c-PEG-20, one-way ANOVA). b) Normalized protein adsorption of PLL-coated glass substrates and different CNT-PEG composite samples (n = 6 for all conditions), one-way ANOVA. c) Cell viability of PC12 cells cultured on PLL-coated glass substrates (control, green) and c-PEG-20 samples (red) at different culture time points following plating (n = 7 for 24 h, 6 for 48 h and 5 for 72 h control and 7 for all time points for c-PEG-20 samples, two-way ANOVA). d) Cell survival rate of PC12 cells after 24 h on PLL-coated glass substrates and on c-PEG-20 samples (n = 6 for controls and 5 for c-PEG-20 samples). e) Immunostaining images of PC12 cells after differentiation for 12 days on PLL-coated glass substrates (control), c-PEG-5, c-PEG-10 and c-PEG-20 samples. Cells were stained with α/β-tubulin antibody (red) and the nuclei were stained with DAPI (blue). Arrows point to neurites. Scale bar: 50 µm. f) Neurite analysis of PC12 cells cultured on different substrates. Cells with a protrusion length of more than 5 µm were assigned as neurite-bearing cells (n = 5 for PLL-coated glass substrates, 3 for c-PEG-0, 3 for c-PEG-5, 8 for c-PEG-10 and 16 for c-PEG-20, one-way ANOVA). g) Neurite length measurement of PC12 cells cultured on different substrates. (n = 21 cells for control, 67 cells for c-PEG-5, 80 cells for c-PEG-10 and 110 cells for c-PEG-20, one-way ANOVA). h, i) Immunofluorescent detection of phosphorylated focal adhesion kinase (FAK^{pY397}) and of paxillin in PC12 cells cultured on PLL-coated glass substrates (left) or c-PEG-20 samples (right). Note that the fluorescence intensity for PLL-coated glass substrates (left) was adjusted for brightness/contrast to allow for better visualization. F-actin (orange) displays cell protrusions and shows presence of FAK^{pY397} in cell filopodia, which was especially visible when PC12 cells were cultured on c-PEG-20 samples. j) Quantitative assessment of fluorescence intensity

revealed significant increase of FAK^{pY397} and paxillin in PC12 cells cultured on c-PEG-20 samples (n = 6 cells for each condition, two-sided t-test). k, l) Western blot of the total FAK (k) and of the active, phosphorylated FAK (FAK^{pY397}, l) show a significant increase of FAK and of FAK^{pY397} when PC12 cells were cultured on c-PEG-20 samples (n = 6 for all conditions, two-sided unpaired t-test). m-q) Images of proximity ligation assay pointing protein-protein interaction of integrin beta 1 (ITGB1) with FAK (m), FAK^{pY397} (n), paxillin (o), paxillin^{pY118} (p) and talin (q). Note the higher protein-protein interaction signals (depicted by red signals) on c-PEG-20 samples when compared to PLL-coated glass substrates (controls). Quantitative analysis of signals pointing to protein/protein interaction revealed significant higher interaction for FAK/ITGB1 (m), FAK^{pY397}/ITGB1 (n), paxillin/ITGB1 (o), paxillin^{pY118}/ITGB1 (p), talin/ITGB1 (q). (n = 5 cells on control glass substrates and 6 cells on c-PEG-20 samples for FAK/ITGB1; 5 cells on control substrate and 5 cells on c-PEG-20 samples for FAK^{pY397}/ITGB1; 6 cells on control substrate and 6 cells on c-PEG-20 samples for paxillin/ITGB1; 6 cells on control substrate and 6 cells on c-PEG-20 samples for paxillin^{pY118}/ITGB1; 6 cells on control substrate and 6 cells on c-PEG-20 samples for talin/ITGB1; unpaired two-tailed t-test was used for normal distributed data and Mann-Whitney test was used for non-parametric data). Bar graphs show mean ± SEM. *p < 0.05, **p < 0.01, ***p < 0.001, ****p < 0.0001

The potential mechanism for triggering the differentiation of PC12 cells on the composites was analyzed, focusing on the focal adhesion-mediated signaling. The surface microstructures have been reported to promote cell differentiation by triggering intracellular signal transduction pathways via the integrin-mediated focal adhesions.[40] Focal adhesions are macromolecular complexes consisting mainly of integrins, focal adhesion kinases (FAK), paxillin, talin, which form mechanical links between intracellular actin bundles and the extracellular matrix or substrates. The integrin activation results in various intracellular signaling alterations related to cell motility, survival, proliferation and differentiation and was shown to be important for neuronal adhesion as well as for neuronal maturation, where it plays an important role in the formation of synaptic contacts, morphologically visible as dendritic spines.[351] The phosphorylation of FAK at tyrosine-397 (FAK^{pY397}) is regarded as the most critical event for neuronal differentiation since FAK^{pY397} functions as an activated form and a

'switch' for multiple signaling outputs.[352, 353] One of the most important downstream targets of FAK is paxillin. The phosphorylation of paxillin (paxillin^{pY118}) acts as a platform for the downstream signaling.

PC12 cells cultured on c-PEG-20 samples for 3 days developed more neurites as shown by filamentous actin (F-actin), which reflects the neuronal polarization during the early differentiation stage (**Figure 5.3**h). The fluorescence intensity of immunostaining indicates a higher expression level of FAK^{pY397} and paxillin of PC12 cells cultured on c-PEG-20 samples compared to the control (**Figure 5.3**i, j, and **Figure S5.8** in **Appendix III**). In order to quantify upregulation of FAK and of its active form, FAK^{pY397}, fluorescence Western blotting was performed, which allows for linear signal quantification. Here, higher total FAK levels as well as increased levels of FAK^{pY397} in cells cultured on c-PEG-20 was detected pointing indeed to increased formation of focal adhesions (**Figure 5.3**k, l). To further evaluate whether the composites are able to promote focal adhesions formation, proximity ligation assay was performed, which is a robust tool to detect protein complexes and an accepted method to detect protein-protein interactions in situ. The data showed significantly increased numbers of FAK/integrin β1(ITGB1), paxillin/ITGB1 and talin/ITGB1 complexes in PC12 cells cultured on c-PEG-20 samples when compared to control cultures (**Figure 5.3**g, h), suggesting an increase of focal adhesion formation induced by the composites. Moreover, PC12 cells on c-PEG-20 samples displayed more FAK^{pY397}/ITGB1 and paxillin^{pY118}/ITGB1 complexes, supporting the surmise that CNT-PEG hydrogel composite induces the differentiation-supporting intracellular signal transduction. Taken together, these results indicate that the surface microstructures promote focal adhesion formation and downstream pro-differentiation signaling activation.

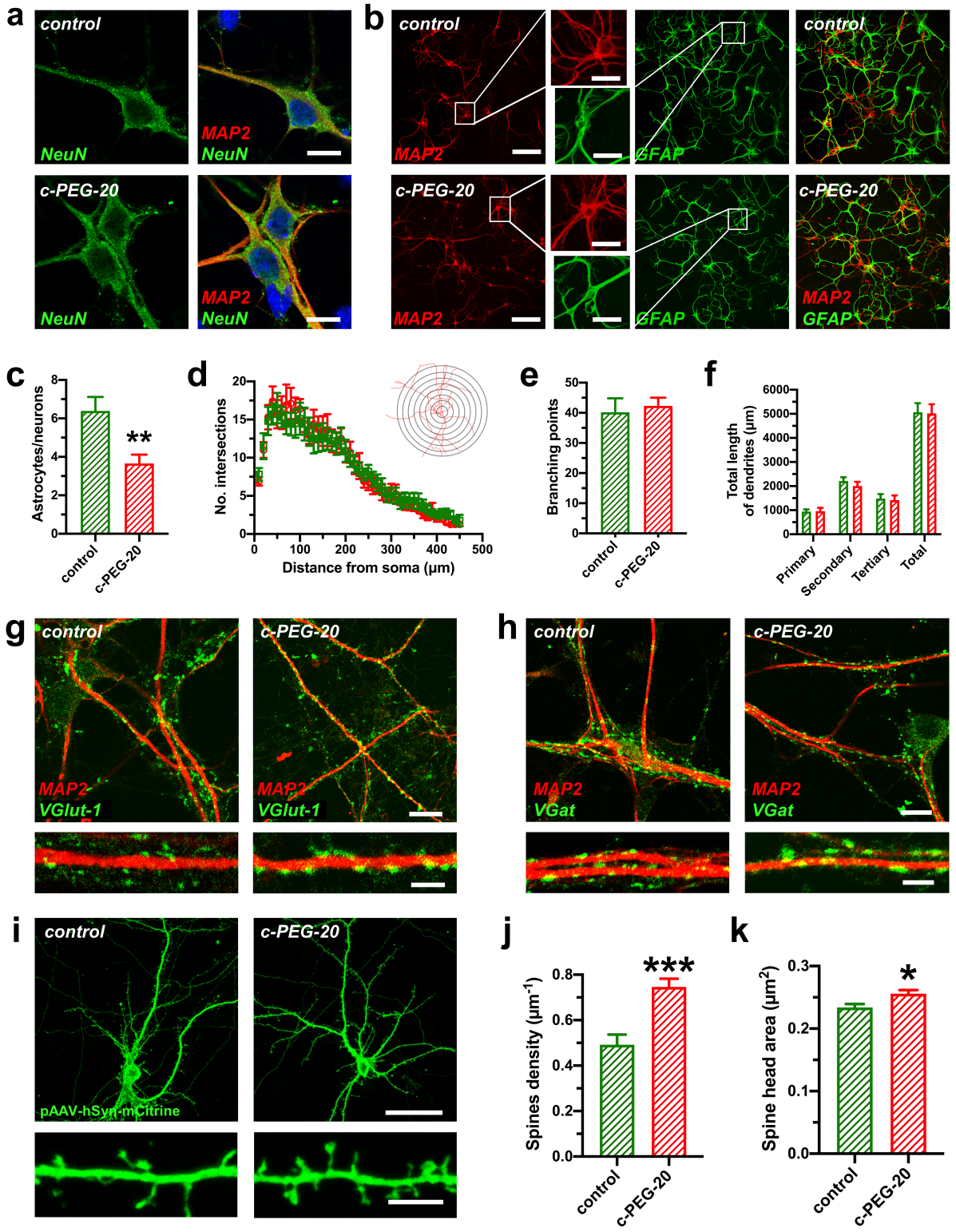

Figure 5.4 Differentiation of adult mouse neural stem cells (NSCs) on PLL-coated glass substrates and c-PEG-20 samples. a) Expression of the neuronal marker NeuN was comparable in neurons cultivated on PLL-coated glass substrates and c-PEG-20 samples. Scale bar: 10 µm. b) Immunostaining images of networks derived from NSCs differentiation on PLL-coated glass substrates and c-PEG-20 samples for 5 weeks. Neurons and astrocytes are stained with MAP2 and GFAP-antibodies, respectively. Scale bar: 50 µm (inset: 20 µm).

c) Astrocytes-to-neurons ratio of NSC-differentiated on glass substrates (control, green) and c-PEG-20 samples (red) (n = 8 control and 7 c-PEG-20, two-sided unpaired *t*-test). d) Sholl analysis plots comparing dendritic complexity of neurons derived from NSC differentiation on glass substrates (green) and c-PEG-20 samples (red). (n = 10 neurons cultured on PLL-coated glass substrates and 10 neurons on c-PEG-20 samples, two-way ANOVA). The inset shows a conceptual example of Sholl analysis. e-f) Branching points (e) and total length of neuron dendrites (f) derived from NSCs on glass substrates (green) and c-PEG-20 samples (red) (n = 10 neurons per condition, two-sided t-test (e) and two-way ANOVA (f)). g) Assessment of glutamatergic input revealed comparable VGlut-1 punctae along MAP-2 stained dendrites on neurons cultivated on control glass substrates and on c-PEG-20 samples. h) Immunostaining revealed similar distribution of inhibitory synapses on MAP-2 stained dendrites of neurons cultivated on glass substrates and on c-PEG-20 samples. i) Immunostaining showing typical NSC-differentiated neurons displaying complex dendritic trees and an axon cultivated on PLL-coated glass substrates (control) and c-PEG-20 samples. Neurons were transfected with the pAAV-hSyn-IRES-mCitrine plasmid and stained with GFP-antibody to visualize the dendritic spines. Higher detail below shows dendritic spines of neurons from NSCs differentiated on control glass substrates or on c-PEG-20 samples. Scale bar: 30 µm, 5 µm. j) Spine density of neurons derived from NSCs show significant higher spine density when cultivated on c-PEG-20 samples. (n = 333 spines from 11 fields of view on glass substrates and n= 612 spines from 14 fields of view on c-PEG-20 samples, unpaired *t*-test). k) Spine head area was significantly increased when neurons were cultivated on c-PEG-20 samples when compared to control substrates (n = 737 spines on neurons on control glass substrates and 875 spines from neurons cultivated on c-PEG-20 samples, two-sided t-test). Bar graphs show mean ± SEM. *p < 0.05, **p < 0.01, ***p < 0.001

While PC12 cells are a commonly used model system to investigate cell viability, adhesion and differentiation, they are derived from the peripheral nervous system and therefore a difficult model to assess regenerative properties of substrates meant to be used for therapy of the central nervous system lesions since they do not form functional synapses. Neural stem cells (NSCs) have been shown to be suitable for restoring connectivity after spinal cord injury.[354, 355] Thus, after observing an enhanced differentiation of PC12 cells, the differentiation of adult murine NSCs on the composites was further investigated (**Figure 5.4**). NSCs are self-renewing, multipotent

cells capable of differentiation into neurons and astrocytes.[356-358] After differentiation for 35 days, both NSCs cultured on PLL-coated glass substrates (control) and c-PEG-20 samples differentiated into neurons (**Figure 5.4**a) and developed into neuron-astrocyte networks (**Figure 5.4**b). No differences in the gross morphology of networks was discerned between PLL-coated glass substrates and c-PEG-20 samples. However, the astrocytes-to-neurons ratio was observed to be lower in c-PEG-20 samples compared to glass substrates (**Figure 5.4**c). Further analysis revealed that the neuronal cell density on the c-PEG-20 samples was comparable to that on the glass substrates, while the cell density of astrocytes was significantly reduced (**Figure S5.9** in **Appendix III**). These results suggest that c-PEG-20 samples were likely to inhibit the proliferation or survival of the NSCs differentiated astrocytes.

The dendritic development of neurons was evaluated by a semi-automatic Sholl analysis. The analysis is conceptually achieved by drawing concentric circles around the soma in a distant-dependent manner. The number of intersections at a varying distance (step = 10 µm) from the soma reflects dendritic complexity (**Figure 5.4**d). No distinct differences were observed between glass substrates and c-PEG-20 samples. The branching and total length of the dendrites were further investigated (**Figure 5.4**e, f). The total length of primary, secondary and tertiary dendrites was thus classified. The results show no significant differences between samples on glass substrates and c-PEG-20 samples. The connectivity patterns of the NSC-derived neurons and interrogated excitatory and inhibitory synaptic inputs was further assessed. Immunostaining displayed well-developed glutamatergic synapses (depicted by the presynaptic excitatory marker VGlut1) and inhibitory, GABAergic synapses in the neuronal network, which were clearly visible along the MAP-2 stained dendritic structures (**Figure 5.4**g, h). Detailed dendritic investigation (lower image in **Figure**

5.4g, h) pointed to bigger and denser synaptic inputs on dendrites of NSC-derived neurons cultured on c-PEG-20 samples.

To quantify synaptic connectivity patterns, detailed morphological analyses (**Figure 5.4**i-k, and **Figure S5.10** in **Appendix III**) were performed, indicating that neurons cultivated on c-PEG-20 samples showed increased density of dendritic spines and a larger spine head area (**Figure 5.4**i-k). The dendritic spines are specific microstructures for neuronal communication and are morphological correlates of functional synapses.[359] The spine density corresponds to the density of synapses, while the spine head area reflects synaptic strength.[360-362] The mean spine density of neurons on PLL-coated glass substrates and c-PEG-20 samples was 0.49 μm^{-1}, and 0.74 μm^{-1}, respectively. These results indicate a higher synaptic connectivity of the neurons cultivated on c-PEG-20 samples when compared to neurons cultivated on PLL-coated glass substrates. As discussed above for PC12 cells, the enhanced protein adsorption and surface microstructures mediated focal adhesion formation might well contribute to the development and maturation of the neurons differentiated from NSCs, which is consistent with the previous report that integrin activation promotes spine formation.[351]

After investigating the differentiation of NSCs, the maturation and the network activity of primary hippocampal neurons was further evaluated. Primary hippocampal neurons were prepared from the embryonic (day 17) mouse hippocampal anlage and represent an intermediate time point in the development of this postmitotic neuronal population,[363, 364] which makes them especially suitable for analysis of effects of different substrates on neuronal differentiation and maturation. Cultures of primary neurons form synaptic connections and are therefore used as in vitro models to study neuronal excitability regulation. Primary hippocampal neurons exhibited similar gross

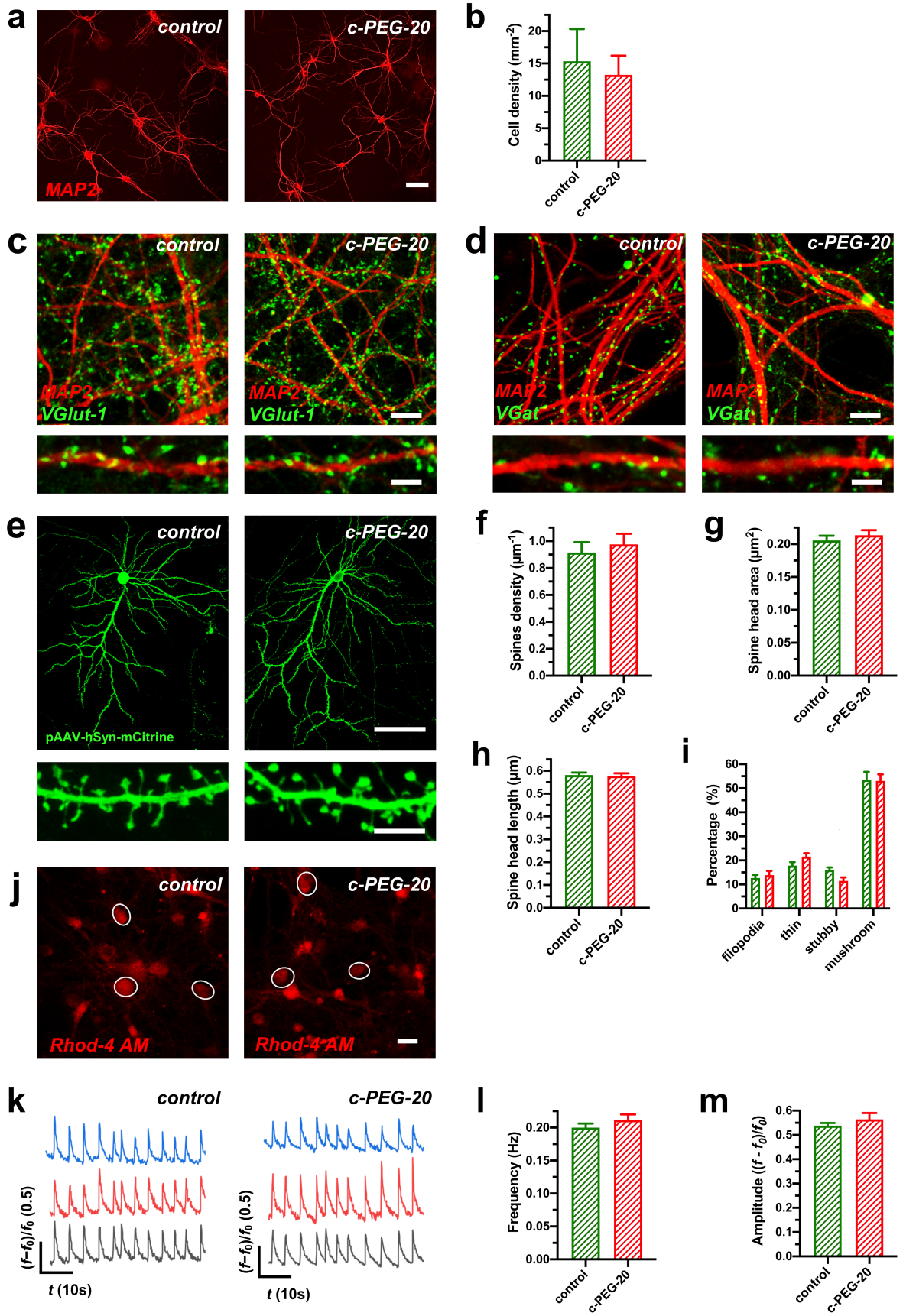

Figure 5.5 *Caption details see next page.*

morphology and network densities on PLL-coated glass substrates (control) and c-PEG-20 samples after 16 days in vitro (DIV 16) (**Figure 5.5**a, b). In order to assess neuronal network excitation/inhibition balance, immunofluorescent staining of glutamatergic, excitatory and GABAergic, inhibitory inputs was first performed. The results indicates similar distribution of excitatory and inhibitory synapses along the MAP-2 stained dendrites (**Figure 5.5**c, d).

Figure 5.5 Differentiation and neuronal activity of primary hippocampal neurons cultured on PLL-coated glass substrates and c-PEG-20 samples. a, b) Immunostaining of dendritic processes (stained with MAP-2) of neuronal networks of primary hippocampal neuron cultures grown on PLL-coated glass substrates (control) and c-PEG-20 samples for 16 days in vitro (DIV16). Quantitative assessment of cell densities of neurons cultured on the different substrates did not reveal significant differences (n = 3 cultures on control and 4 cultures on c-PEG-20 samples for cell density, two-tailed t-test). Scale bar: 50 µm. c) Glutamatergic input revealed comparable VGlut-1 puncta along MAP-2 stained dendrites on primary hippocampal neurons cultivated on control glass substrates and on c-PEG-20 samples. d) Inhibitory synapses on MAP-2 stained dendrites of neurons cultivated on glass substrates displayed a similar distribution when compared to neurons cultivated on c-PEG-20 samples. Scale bars: 10 µm for (c, d) and 5 µm for (c, d) detail images. e) Exemplary images of GFP-transfected primary hippocampal neurons and their dendritic spines (below) from neuronal cultures grown on PLL-glass substrates and c-PEG-20 samples for 16 days in vitro (DIV16). For visualization, neurons were transfected with the pAAV-hSyn-IRES-mCitrine plasmid and stained with GFP antibody for visualizing dendritic spines (shown below). Scale bars: 50 µm and 5 µm for detail. f-i) Dendritic spines densities (f), spine head area (g), spine head length (h) and quantitative analysis of spine categories (i) were comparable when primary hippocampal neurons were cultured on PLL-coated glass substrates (control, green) or c-PEG-20 samples (red) (n = 614 spines from neurons cultivated on control and 534 spines from neurons cultivated on c-PEG-20 samples [f], n = 520 spines from neurons cultivated on control and 570 spines from neurons cultivated on c-PEG-20 samples [g], n = 520 spines from neurons cultivated on control and 570 spines from neurons cultivated on c-PEG-20 samples [h], n = 614 spines analyzed from neurons cultivated on control glass substrates and 534 spines from neurons cultivated on c-PEG-20 samples [i], two tailed t-test or Mann-Whitney test for nonparametric data). j) Overview on rhodamine-4 AM loaded neurons cultivated on

control and c-PEG-20 samples. Circled neurons were assessed for Ca^{2+}-oscillations as exemplary depicted by original traces shown in (k). Scale bar: 20 µm. l, m) Frequencies and amplitudes of synchronized calcium oscillations did not show significant differences for primary hippocampal neurons when grown on PLL-coated glass substrates or c-PEG-20 samples (n = 13 recordings on control and 11 recordings on c-PEG-20 samples for frequency analysis and n = 36 measurements for amplitudes from neurons cultivated on control glass substrates and 33 measurements for amplitudes from neurons plated on c-PEG-20 samples, two sided t-test). Bar graphs show mean ± SEM.

The maturity of neurons was then analyzed by evaluating dendritic spine densities, measurement of the spine head area, spine head length and by assessment of the different spine categories. The mean spine densities of neurons on glass substrates and c-PEG-20 samples were 0.94 and 0.97 μm^{-1}, respectively (**Figure 5.5**f). The data suggest that primary hippocampal neurons grown on c-PEG-20 substrate displayed a comparable spine head area, spine head length and a spine maturation as shown by analysis of the different spine categories by careful assessment of spine morphology (**Figure 5.5**g-i). These results indicate that c-PEG-20 samples are optimally suited for development of primary immature neurons which exhibit a robust innate differentiation program, a finding which is consistent with previous studies.[44, 45, 234, 322] Therefore, primary hippocampal neurons serve as a good model for investigating the properties of network activity on the composites.

The network activity of primary hippocampal neurons was next investigated by calcium imaging, which is a reliable method used to track the activity of neuronal populations.[365] The primary hippocampal neurons cultured in vitro for 14 days exhibited spontaneous synchronized calcium oscillations driven by synaptic activity.[366] Using a calcium indicator (Rhod-4 AM) and confocal microscopy, the oscillations of free cytosolic calcium in primary cultures of hippocampal neurons were recorded (**Figure 5.5**j,k). The frequency of calcium oscillations, which is dependent on the

periodic changes of the membrane potential driven by action potentials, reflects neuronal network excitability.[366, 367] The amplitude reflects the efficacy of action potential in evoking postsynaptic calcium current through glutamatergic receptors and voltage-gated calcium channels.[366, 368] Here, the frequencies and amplitudes of calcium oscillations in the neurons cultured on PLL-coated glass substrates and c-PEG-20 samples were compared (**Figure 5.5**l, m). These results indicate that the CNT-PEG hydrogel composites are able to maintain the homeostasis of neuronal network activity.

These results differ from earlier studies performed on CNT-coated substrates where an increased neuronal excitability was reported.[44, 322] The main difference between CNT-coated substrates and CNT-PEG hydrogel composites is that in the latter case, the CNTs were embedded in the hydrogel and thus their interactions with the neurons might have been partially disrupted. Thus, the encapsulation of the CNT network into the hydrogel matrix could indeed play a critical role in maintaining the homeostasis of neuronal network activity. Therefore, the encapsulation of the CNT network into the hydrogel matrix did not change the developmental balance between excitatory synapses and inhibitory synapses, thereby preserving intrinsic neuronal activity and neuronal network homeostasis.

5.4 Conclusions

In summary, a novel and versatile method for preparing CNT-hydrogel composites has been demonstrated. The effects of CNT-PEG hydrogel composites on neuronal differentiation and electrical activity were investigated using PC12 cells, adult NSCs which were differentiated into neurons and astrocytes and primary hippocampal neurons. It is demonstrated that the composites were beneficial for the long-term survival and differentiation of PC12 cells and NSCs. The results show an enhanced

differentiation of PC12 cells and an increased neuron-to-astrocyte ratio of NSCs on the composites compared to the control conditions of glass substrates. Furthermore, the spine density of neurons derived from NSCs was increased. The enhanced differentiation of PC12 cells and NSCs may be ascribed to the enhanced surface microstructures and protein adsorption. Moreover, network activity of primary cultures of hippocampal neurons cultured on the composites was maintained within a physiological range and was comparable to neuronal activity of primary neurons from the same preparation cultured on standard control conditions. In addition, c-PEG-20 composites allowed for optimal neuronal differentiation up to the level of dendritic spines. To sum up, the data suggest that the CNT-PEG hydrogel composites are novel versatile substrates for culturing neurons, suitable for the development of lesion interponates for potential use in vivo. These substrates display several advantages for neuronal differentiation while maintaining homeostatic properties of neuronal networks which is an important prerequisite when intended to be used for repair of CNS lesions, which are often associated with pathological hyperexcitability as present, *e.g.*, in the case of ischemic stroke.

5.5 Appendix III

Table S5.1 UV illumination time of CNT-PEG hydrogel composites with varying CNT content.

Notation	CNT concentration (g L^{-1})[a]	UV illumination time (s)[b]
c-PEG-0	0	10
c-PEG-5	5	60
c-PEG-10	10	120
c-PEG-20	20	240

[a)] The concentration here is referring to the CNTs in the ionic liquid. [b)] UV light: 365 nm, 250 mA (*i.e.*, 15.6 mW cm^{-2}).

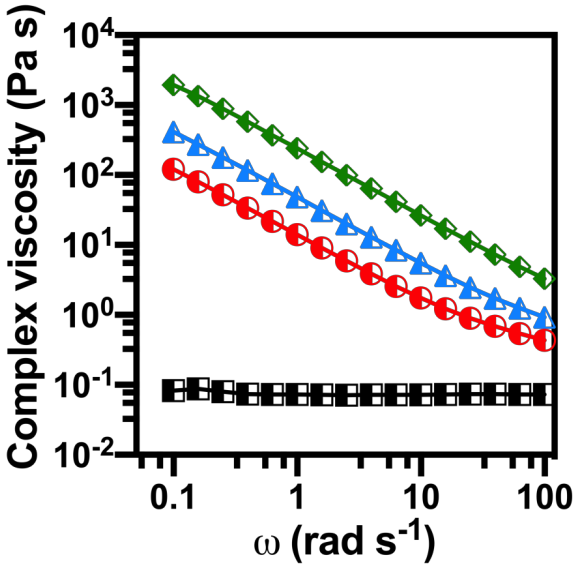

Figure S5.1 Frequency dependence of complex viscosity of the precursors of CNT-PEG hydrogel composites with varying CNT content. (◧: c-PEG-0, ◐: c-PEG-5, ◭ c-PEG-10, ◆: c-PEG-20 samples).

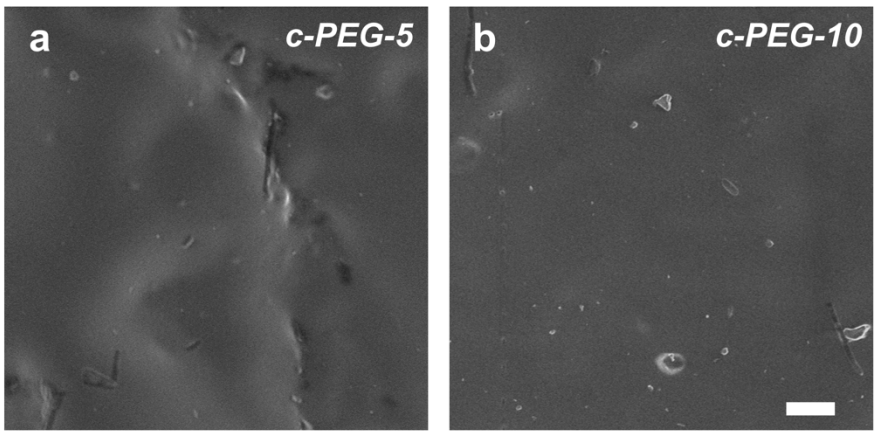

Figure S5.2 Scanning electron microscopy images of (a) c-PEG-5 and (b) c-PEG-10 samples after gentle dehydration. Scale bar: 5 µm.

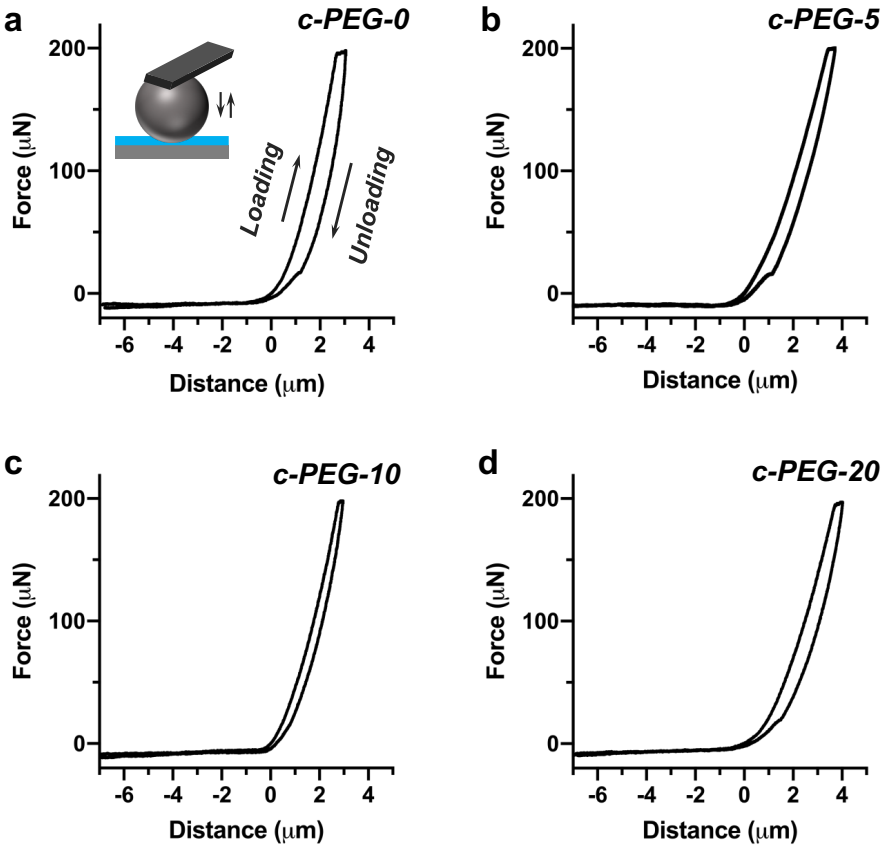

Figure S5.3 Indentation curves of CNT-PEG hydrogel composites with varying CNT content. (a) c-PEG-0, (b) c-PEG-5, (c) c-PEG-10, and (d) c-PEG-20 samples. The elastic modulus of the composites was obtained by fitting the loading curves with the Hertz model.

$$F = \frac{4}{3}\frac{E}{1-\mu^2}\sqrt{R\delta^3}$$

where E is the elastic modulus of the sample, μ is the Poisson's ratio of the sample, R is the radius of the probe, and δ is the indentation depth.

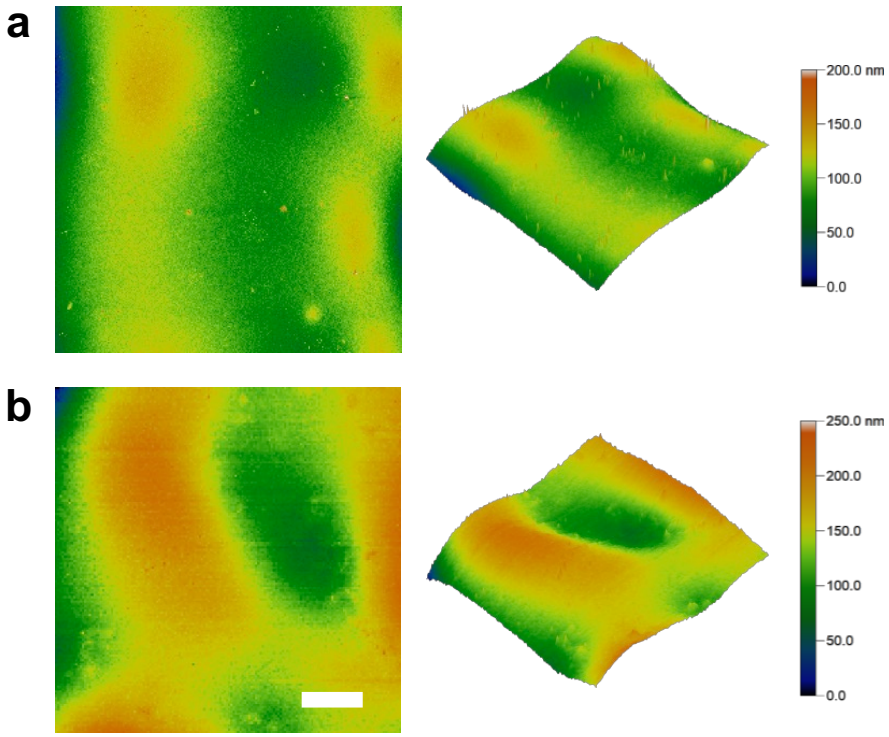

Figure S5.4 2D and 3D topographies of (a) c-PEG-5 and (b) c-PEG-10 samples captured by atomic force microscopy in water. Scale bar: 5 μm.

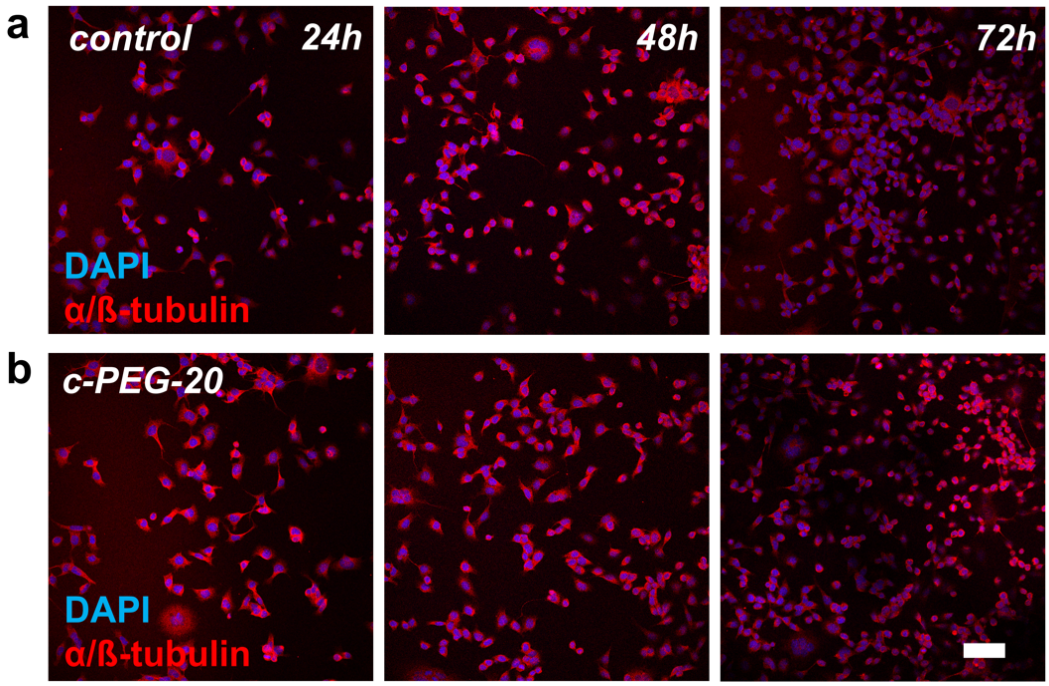

Figure S5.5. Confocal scanning laser microscopy (CLSM) images of PC12 cells cultured on PLL-coated (a) glass substrates and (b) c-PEG-20 samples for 24 h, 48 h, 72 h. Cells were stained with Tubulin antibody (the nuclei were stained with dihydrochloride). Scale bar: 100 μm.

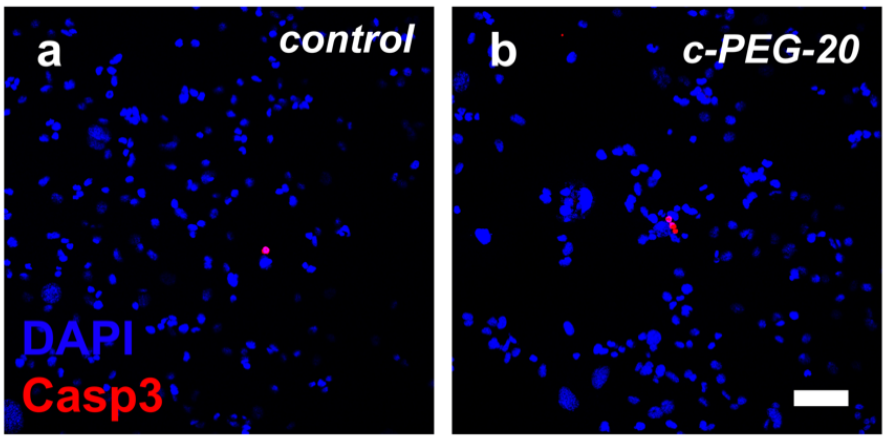

Figure S5.6. CLSM images of PC12 cells cultured on PLL-coated (a) glass substrates and (b) c-PEG-20 samples for 48 h. The nuclei (blue) were stained with dihydrochloride, and the dead cells were marked with cleaved Caspase3 (red). Scale bar: 100 μm.

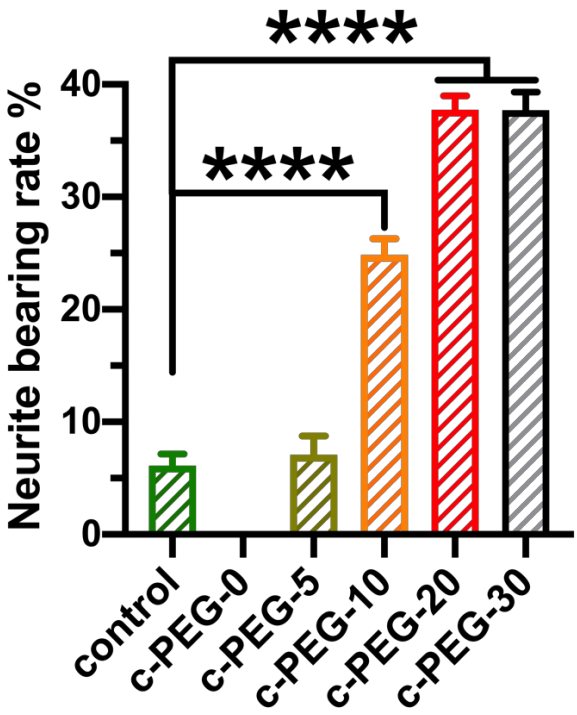

Figure S5.7 Neurite bearing rate of PC12 cells cultured on PLL-coated glass substrates and CNT-PEG hydrogel composites with varying CNT content (n = 5 for PLL-coated glass plates, 3 for c-PEG -0, 3 for c-PEG-5, 8 for c-PEG-10, 16 for c-PEG-20 and 8 for c-PEG-30, one-way ANOVA). Bar graphs show mean ± SEM. ****p < 0.0001.

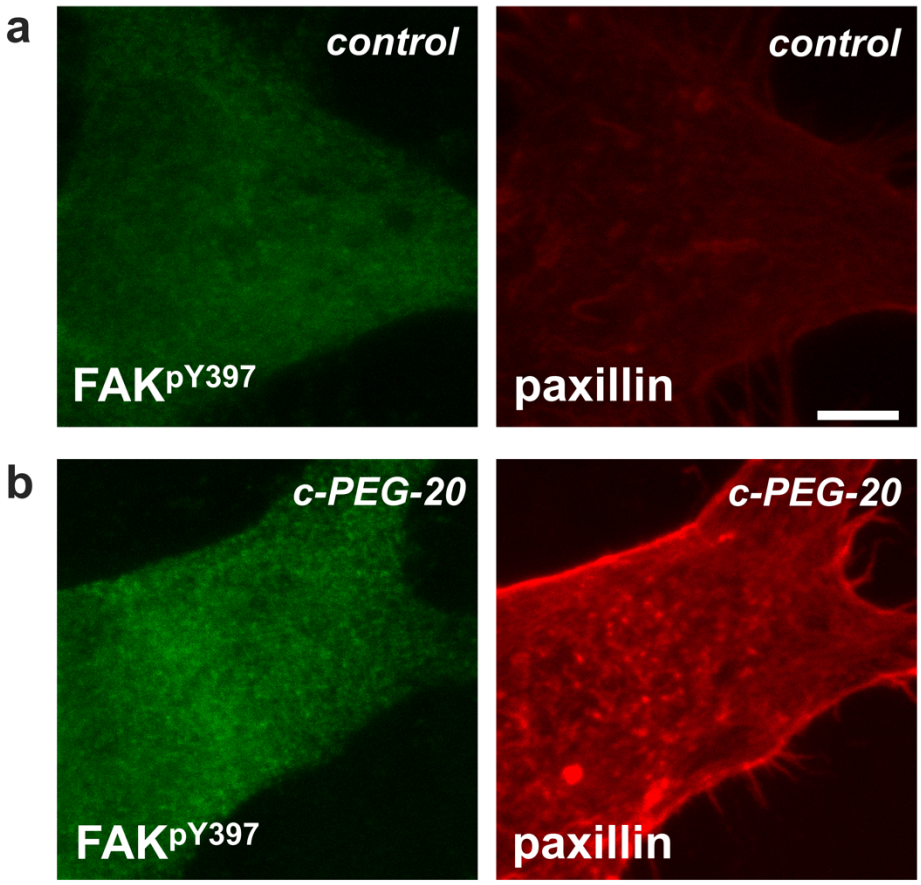

Figure S5.8 CLSM images of PC12 cells cultured on (a) glass substrates and (b) c-PEG-20 samples for 72 h. Cells were stained with Phospho-FAK (Tyr397) Antibody Paxillin antibody. Scale bar: 5 µm.

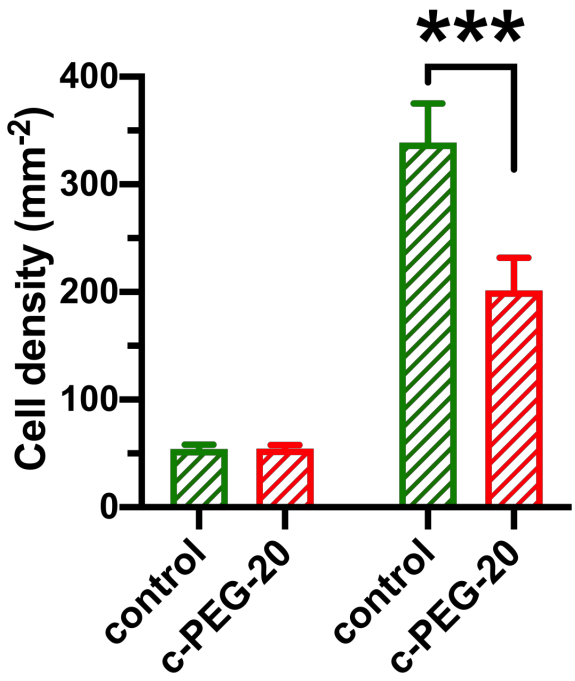

Figure S5.9 Cell density of neuron (left) and astrocyte (right) from NSC differentiated on PLL-coated glass substrates (control) and c-PEG-20 samples (n = 8 for control and 7 for c-PEG-20) ***: $p < 0.0001$, two-sided t-test.

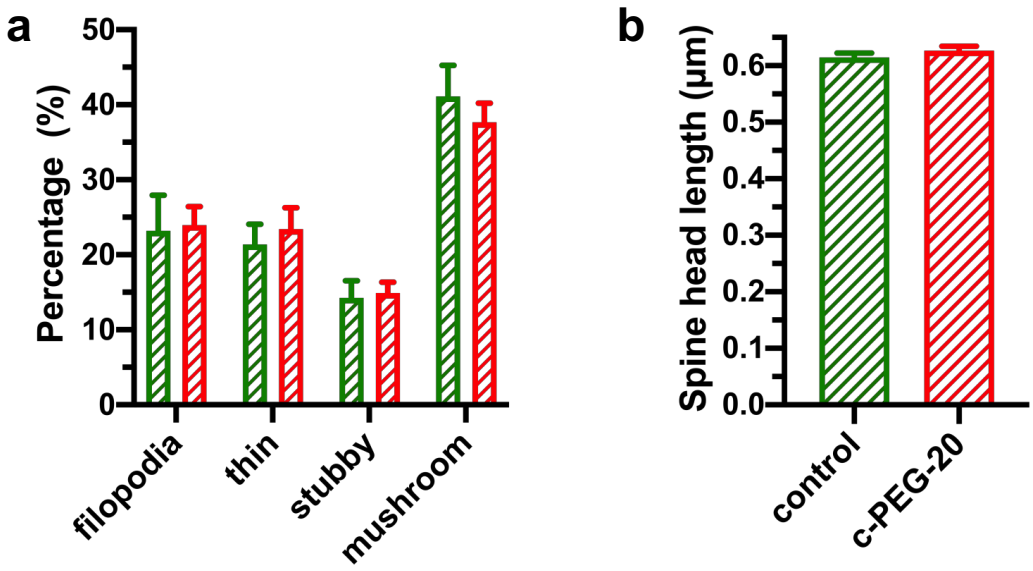

Figure S5.10 Results comparing the morphological classification of dendritic spines by shape (a) and the head length of dendritic spines (b) of neurons derived from NSCs cultured on PLL-coated glass substrates (green) or on c-PEG-20 samples (red) (for a: n = 614 total spine numbers in percent from 11 fields of view for NSC-derived neurons cultured on PLL-coated glass plates and total 534 spine numbers in percent from 14 fields of view for NSC-derived neurons cultured on c-PEG-20 substrates, for b: n = 737 spines from neurons cultured on PLL-coated glass slides and 875 spines from neurons cultured on c-PEG-20 substrates. two-sided t-test).

Chapter 6

Concluding Remarks

This thesis focuses on the development, characterization, and applications of polymer-based biomaterials. Different polymer composites for specific biomedical applications have been developed by incorporating organic salts or inorganic nanoparticles into the polymer matrix. These include: (i) responsive ionogels with a self-replenishing surface for combating biofouling; (ii) mechanically elastic superhydrophobic composite coatings with photocatalytic activity for wound dressing; (iii) carbon nanotube-hydrogel composites for nerve tissue engineering.

A new type of responsive ionogel with renewable antibiofouling properties has been described in the first part of the work (**Chapter 3**). The renewability of the antibiofouling performance relies on the spontaneous migration of ionic liquids infiltrated within polymer scaffolds to the surface. The phase-transition of ionic liquids is used as a 'switch', allowing for reversibly activating the ionogel surface from bactericidal (antimicrobial surface) to biofilm-release (slippery surface) functions. The reversibility of the surface properties enables restoring antimicrobial efficacy after biofilm contamination, tackling the big challenge of irreversible loss of bactericidal functions of traditional antimicrobial surfaces. On the other hand, uncontrollable liquid loss is one of the main drawbacks of traditional slippery surfaces. The on-demand activation of phase transition can minimize the unexpected loss of ionic liquids. I believe this new type of ionogels will be helpful for the long-term stability of combating biofouling. Future work can focus on studying the migration of ionic liquids from polymer gel matrices, which will help better understand the self-replenishing process of the surface and, hopefully, control the process.

The second part of the work is focused on preparing and characterizing a mechanically elastic and photocatalytically active superhydrophobic coating (**Chapter 4**). Due to their non-wetting features, superhydrophobic surfaces serve as a promising candidate for blood-repellent wound dressing, capable of minimizing the loss of blood and the formation of clot-gauze composites. To tackle the poor mechanical properties and biocompatibility, a new strategy for preparing superhydrophobic surfaces based on the self-assembly of titanium nanoparticles with biocompatible polymers has been proposed. The combination of mechanically elastic polymers and photocatalytically active titanium provides robust blood repellency and additional antimicrobial functions of the superhydrophobic coatings. This new strategy may help develop blood repellent wound dressing capable of reducing blood loss, clot-gauze composite formation, and bacterial infections. Future work can focus on studying the possible mechanism of blood clotting on this type of superhydrophobic surface. It will be beneficial for further exploring the capacity of the superhydrophobic coatings to promote rapid blood clotting while maintaining low blood adhesion.

In the last part of the work (**Chapter 5**), a new and versatile method to prepare carbon nanotube-hydrogel composites has been described. The electrical conductivity of such nanocomposite hydrogels has been often assumed to facilitate neuronal differentiation by stimulating neuronal excitability. To obtain deeper understanding of whether the electrical conductivity of nanocomposite hydrogels could actually affect neuronal differentiation and excitability, different cell types with varying behaviors have been used for investigation. It is observed that the nanocomposite hydrogels could indeed facilitate neuronal differentiation while maintaining homeostasis of network activity. The results provide new insights showing that high electrical conductivity by itself is not fundamental for carbon nanotube-based nanocomposites to be used as

artificial nerve grafts. Concurrently, other physicochemical properties, such as surface topography, should also be considered to design biocompatible functional scaffolds for nerve regeneration. Future work can focus on studying neuronal behaviors on the nanocomposite hydrogels under electrical stimulation, which will provide new information beneficial for further exploring the possibility of the nanocomposite hydrogels to be used as neural interface electrodes for signal recording and stimulation.

The surface properties of biomaterials that interact with the biological systems are essential. As proof of concept, the three parts of the work demonstrated that the combination of polymers with tunable physicochemical properties and organic salts and inorganic nanoparticles with diverse functionality could serve as an efficient toolbox for developing advanced biomaterials with specific surface characteristics.

Acknowledgements

[In der elektronischen Fassung aus Datenschutzgründen entfernt]

Bibliography

[1] Jenkins, A. D.; Kratochvíl, P.; Stepto, R. F. T.; Suter, U. W., *Pure Appl. Chem.* **1996,** *68*, 2287.

[2] Rubinstein, M.; Colby, R. H., *Polymer Physics*. OUP Oxford: 2003.

[3] Gentekos, D. T.; Sifri, R. J.; Fors, B. P., *Nat. Rev. Mater.* **2019,** *4*, 761.

[4] Lutz, J.-F.; Lehn, J.-M.; Meijer, E. W.; Matyjaszewski, K., *Nat. Rev. Mater.* **2016,** *1*, 16024.

[5] Vogl, O.; Bartus, J.; Qin, M.; Zarras, P., *J. Macromol. Sci. A* **1994,** *31*, 1329.

[6] Zhu, X.; Zhou, Y.; Yan, D., *J. Polym. Sci., Part B: Polym. Phys.* **2011,** *49*, 1277.

[7] Zhou, Y.; Hsiao, K.-W.; Regan, K. E.; Kong, D.; McKenna, G. B.; Robertson-Anderson, R. M.; Schroeder, C. M., *Nat. Commun.* **2019,** *10*, 1753.

[8] Seo, S. E.; Hawker, C. J., *Macromolecules* **2020,** *53*, 3257.

[9] Whitfield, R.; Truong, N. P.; Messmer, D.; Parkatzidis, K.; Rolland, M.; Anastasaki, A., *Chem. Sci.* **2019,** *10*, 8724.

[10] Brighenti, R.; Li, Y.; Vernerey, F. J., *Front. Mater.* **2020,** *7*.

[11] Leigh, T.; Fernandez-Trillo, P., *Nat. Rev. Chem.* **2020,** *4*, 291.

[12] Daly, A. C.; Riley, L.; Segura, T.; Burdick, J. A., *Nat. Rev. Mater.* **2020,** *5*, 20.

[13] Fahlman, M.; Fabiano, S.; Gueskine, V.; Simon, D.; Berggren, M.; Crispin, X., *Nat. Rev. Mater.* **2019,** *4*, 627.

[14] Lopez, J.; Mackanic, D. G.; Cui, Y.; Bao, Z., *Nat. Rev. Mater.* **2019,** *4*, 312.

[15] Rutten, M. G. T. A.; Vaandrager, F. W.; Elemans, J. A. A. W.; Nolte, R. J. M., *Nat. Rev. Chem.* **2018,** *2*, 365.

[16] Detsch, R.; Will, J.; Hum, J.; Roether, J. A.; Boccaccini, A. R., Biomaterials. In *Cell Culture Technology*, Kasper, C.; Charwat, V.; Lavrentieva, A., Eds. Springer International Publishing: Cham, 2018; pp 91.

[17] Maan, A. M. C.; Hofman, A. H.; de Vos, W. M.; Kamperman, M., *Adv. Funct. Mater.* **2020,** *30*, 2000936.

[18] Ekladious, I.; Colson, Y. L.; Grinstaff, M. W., *Nat. Rev. Drug Discov.* **2019,** *18*, 273.

[19] Mir, M.; Ali, M. N.; Barakullah, A.; Gulzar, A.; Arshad, M.; Fatima, S.; Asad, M., *Prog. Biomater.* **2018,** *7*, 1.

[20] Moon, J.-M.; Thapliyal, N.; Hussain, K. K.; Goyal, R. N.; Shim, Y.-B., *Biosens. Bioelectron.* **2018,** *102*, 540.

[21] Sadtler, K.; Singh, A.; Wolf, M. T.; Wang, X.; Pardoll, D. M.; Elisseeff, J. H., *Nat. Rev. Mater.* **2016,** *1*, 16040.

[22] Arciola, C. R.; Campoccia, D.; Montanaro, L., *Nat. Rev. Microbiol.* **2018,** *16*, 397.

[23] Dobretsov, S.; Abed, R. M. M.; Teplitski, M., *Biofouling* **2013,** *29*, 423.

[24] Geyer, F.; D'Acunzi, M.; Yang, C.-Y.; Müller, M.; Baumli, P.; Kaltbeitzel, A.; Mailänder, V.; Encinas, N.; Vollmer, D.; Butt, H.-J., *Adv. Mater.* **2019,** *31*, 1801324.

[25] Wei, T.; Tang, Z.; Yu, Q.; Chen, H., *ACS Appl. Mater. Interfaces* **2017,** *9*, 37511.

[26] Mi, L.; Jiang, S., *Angew. Chem. Int. Ed.* **2014,** *53*, 1746.

[27] Yang, C.; Ding, X.; Ono, R. J.; Lee, H.; Hsu, L. Y.; Tong, Y. W.; Hedrick, J.; Yang, Y. Y., *Adv. Mater.* **2014,** *26*, 7346.

[28] Epstein, A. K.; Wong, T.-S.; Belisle, R. A.; Boggs, E. M.; Aizenberg, J., *Proc. Natl. Acad. Sci. U. S. A.* **2012,** *109*, 13182.

[29] Zhu, T.; Wu, J.; Zhao, N.; Cai, C.; Qian, Z.; Si, F.; Luo, H.; Guo, J.; Lai, X.; Shao, L.; Xu, J., *Adv. Healthc. Mater.* **2018,** *7*, 1701086.

[30] Jokinen, V.; Kankuri, E.; Hoshian, S.; Franssila, S.; Ras, R. H. A., *Adv. Mater.* **2018**, e1705104.

[31] Sasaki, K.; Tenjimbayashi, M.; Manabe, K.; Shiratori, S., *ACS Appl. Mater. Interfaces* **2016,** *8*, 651.

[32] Quan, K.; Li, G.; Luan, D.; Yuan, Q.; Tao, L.; Wang, X., *Colloid Surf. B-Biointerfaces* **2015,** *132*, 27.

[33] Paven, M.; Papadopoulos, P.; Schottler, S.; Deng, X.; Mailander, V.; Vollmer, D.; Butt, H. J., *Nat. Commun.* **2013,** *4*, 2512.

[34] Kheirabadi, B. S.; Mace, J. E.; Terrazas, I. B.; Fedyk, C. G.; Estep, J. S.; Dubick, M. A.; Blackbourne, L. H., *J. Trauma Acute Care Surg.* **2010,** *68*.

[35] Radomski, A.; Jurasz, P.; Alonso-Escolano, D.; Drews, M.; Morandi, M.; Malinski, T.; Radomski, M. W., *British Journal of Pharmacology* **2005,** *146*, 882.

[36] Subramanian, A.; Krishnan, U. M.; Sethuraman, S., *J. Biomed. Sci.* **2009,** *16*, 108.

[37] Sarker, M.; Naghieh, S.; McInnes, A. D.; Schreyer, D. J.; Chen, X., *Biotechnol. J.* **2018,** *13*, 1700635.

[38] Palispis, W. A.; Gupta, R., Chapter 14 - Biologic Augmentation in Peripheral Nerve Repair. In *Biologics in Orthopaedic Surgery*, Mazzocca, A. D.; Lindsay, A. D., Eds. Elsevier: Philadelphia, 2019; pp 141.

[39] Du, J.; Jia, X., *Neural Regen. Res.* **2019,** *14*, 2073.

[40] Eftekhari, B. S.; Eskandari, M.; Janmey, P. A.; Samadikuchaksaraei, A.; Gholipourmalekabadi, M., *Adv. Funct. Mater.* **2020,** *30*, 1907792.

[41] Burnstine-Townley, A.; Eshel, Y.; Amdursky, N., *Adv. Funct. Mater.* **2019**, 1901369.

[42] Liu, X.; Miller, A. L.; Park, S.; Waletzki, B. E.; Zhou, Z.; Terzic, A.; Lu, L., *ACS Appl. Mater. Interfaces* **2017,** *9*, 14677.

[43] Park, J.; Jeon, J.; Kim, B.; Lee, M. S.; Park, S.; Lim, J.; Yi, J.; Lee, H.; Yang, H. S.; Lee, J. Y., *Adv. Funct. Mater.* **2020**, 2003759.

[44] Lovat, V.; Pantarotto, D.; Lagostena, L.; Cacciari, B.; Grandolfo, M.; Righi, M.; Spalluto, G.; Prato, M.; Ballerini, L., *Nano Lett.* **2005,** *5*, 1107.

[45] Cellot, G.; Cilia, E.; Cipollone, S.; Rancic, V.; Sucapane, A.; Giordani, S.; Gambazzi, L.; Markram, H.; Grandolfo, M.; Scaini, D.; Gelain, F.; Casalis, L.; Prato, M.; Giugliano, M.; Ballerini, L., *Nat. Nanotechnol.* **2009,** *4*, 126.

[46] Young, T., *Philos. Trans. R. Soc. London* **1805,** *95*, 65.

[47] Quéré, D., *Annu. Rev. Mater. Res.* **2008,** *38*, 71.

[48] Wenzel, R. N., *Ind. Eng. Chem.* **1936,** *28*, 988.

[49] Cassie, A. B. D.; Baxter, S., *Trans. Faraday Soc.* **1944,** *40*, 546.

[50] Cassie, A. B. D., *Discuss. Faraday Soc.* **1948,** *3*, 11.

[51] Feng, X. J.; Jiang, L., *Adv. Mater.* **2006,** *18*, 3063.

[52] Hyväluoma, J.; Timonen, J., *Europhys. Lett.* **2008,** *83*, 64002.

[53] Papadopoulos, P.; Mammen, L.; Deng, X.; Vollmer, D.; Butt, H.-J., *Proc. Natl. Acad. Sci. U. S. A.* **2013,** *110*, 3254.

[54] Lam, C. N. C.; Wu, R.; Li, D.; Hair, M. L.; Neumann, A. W., *Adv. Colloid Interface Sci.* **2002,** *96*, 169.

[55] He, B.; Lee, J.; Patankar, N. A., *Colloids Surf. A Physicochem. Eng. Asp.* **2004,** *248*, 101.

[56] Gao, L.; McCarthy, T. J., *Langmuir* **2006,** *22*, 6234.

[57] Law, K.-Y.; Zhao, H., Wetting on Flat and Smooth Surfaces. In *Surface Wetting: Characterization, Contact Angle, and Fundamentals*, Law, K.-Y.; Zhao, H., Eds. Springer International Publishing: Cham, 2016; pp 35.

[58] Pierce, E.; Carmona, F. J.; Amirfazli, A., *Colloids Surf. A Physicochem. Eng. Asp.* **2008,** *323*, 73.

[59] Schellenberger, F.; Encinas, N.; Vollmer, D.; Butt, H.-J., *Phys. Rev. Lett.* **2016,** *116*, 096101.

[60] Miwa, M.; Nakajima, A.; Fujishima, A.; Hashimoto, K.; Watanabe, T., *Langmuir* **2000,** *16*, 5754.

[61] Pan, S.; Guo, R.; Björnmalm, M.; Richardson, J. J.; Li, L.; Peng, C.; Bertleff-Zieschang, N.; Xu, W.; Jiang, J.; Caruso, F., *Nat. Mater.* **2018,** *17*, 1040.

[62] Butt, H.-J.; Berger, R.; Steffen, W.; Vollmer, D.; Weber, S. A. L., *Langmuir* **2018,** *34*, 11292.

[63] Lafuma, A.; Quéré, D., *Nat. Mater.* **2003,** *2*, 457.

[64] Ma, M.; Hill, R. M., *Opin. Colloid Interface Sci.* **2006,** *11*, 193.

[65] Wang, S.; Liu, K.; Yao, X.; Jiang, L., *Chem. Rev.* **2015,** *115*, 8230.

[66] Barthlott, W.; Neinhuis, C., *Planta* **1997,** *202*, 1.

[67] Guo, Z.; Yang, F., Superhydrophobic Surfaces from Nature and Beyond Nature. In *Surfaces and Interfaces of Biomimetic Superhydrophobic Materials*, John Wiley & Sons, Ltd: 2017; pp 25.

[68] Celia, E.; Darmanin, T.; Taffin de Givenchy, E.; Amigoni, S.; Guittard, F., *J. Colloid Interface Sci.* **2013,** *402*, 1.

[69] Herminghaus, S., *Europhys. Lett.* **2000,** *52*, 165.

[70] Manukyan, G.; Oh, J. M.; van den Ende, D.; Lammertink, R. G. H.; Mugele, F., *Phys. Rev. Lett.* **2011,** *106*, 014501.

[71] Tuteja, A.; Choi, W.; McKinley, G. H.; Cohen, R. E.; Rubner, M. F., *MRS Bull.* **2008,** *33*, 752.

[72] Öner, D.; McCarthy, T. J., *Langmuir* **2000,** *16*, 7777.

[73] Pozzato, A.; Zilio, S. D.; Fois, G.; Vendramin, D.; Mistura, G.; Belotti, M.; Chen, Y.; Natali, M., *Microelectron. Eng.* **2006,** *83*, 884.

[74] Feng, J.; Tuominen, M. T.; Rothstein, J. P., *Adv. Funct. Mater.* **2011,** *21*, 3715.

[75] Liu, M.; Li, M.-T.; Xu, S.; Yang, H.; Sun, H.-B., *Front. Chem.* **2020,** *8*.

[76] Qin, D.; Xia, Y.; Whitesides, G. M., *Nat. Protoc.* **2010,** *5*, 491.

[77] Qian, B.; Shen, Z., *Langmuir* **2005,** *21*, 9007.

[78] Teshima, K.; Sugimura, H.; Inoue, Y.; Takai, O.; Takano, A., *Appl. Surf. Sci.* **2005,** *244*, 619.

[79] Qu, M.; Zhang, B.; Song, S.; Chen, L.; Zhang, J.; Cao, X., *Adv. Funct. Mater.* **2007,** *17*, 593.

[80] He, Y.; Jiang, C.; Yin, H.; Chen, J.; Yuan, W., *J. Colloid Interface Sci.* **2011,** *364*, 219.

[81] Liu, T. L.; Kim, C.-J. C., *Science* **2014,** *346*, 1096.

[82] Martines, E.; Seunarine, K.; Morgan, H.; Gadegaard, N.; Wilkinson, C. D. W.; Riehle, M. O., *Nano Lett.* **2005,** *5*, 2097.

[83] Liu, H.; Feng, L.; Zhai, J.; Jiang, L.; Zhu, D., *Langmuir* **2004,** *20*, 5659.

[84] Artus, G. R. J.; Jung, S.; Zimmermann, J.; Gautschi, H. P.; Marquardt, K.; Seeger, S., *Adv. Mater.* **2006,** *18*, 2758.

[85] Teisala, H.; Tuominen, M.; Aromaa, M.; Mäkelä, J. M.; Stepien, M.; Saarinen, J. J.; Toivakka, M.; Kuusipalo, J., *Surf. Coat. Technol.* **2010,** *205*, 436.

[86] Deng, X.; Mammen, L.; Butt, H.-J.; Vollmer, D., *Science* **2012,** *335*, 67.

[87] Teisala, H.; Geyer, F.; Haapanen, J.; Juuti, P.; Mäkelä, J. M.; Vollmer, D.; Butt, H.-J., *Adv. Mater.* **2018,** *30*, 1706529.

[88] Erbil, H. Y.; Demirel, A. L.; Avcı, Y.; Mert, O., *Science* **2003,** *299*, 1377.

[89] Venkateswara Rao, A.; Latthe, S. S.; Nadargi, D. Y.; Hirashima, H.; Ganesan, V., *J. Colloid Interface Sci.* **2009,** *332*, 484.

[90] Li, Y.; Liu, F.; Sun, J., *Chem. Commun.* **2009**, 2730.

[91] Amigoni, S.; Taffin de Givenchy, E.; Dufay, M.; Guittard, F., *Langmuir* **2009,** *25*, 11073.

[92] Sas, I.; Gorga, R. E.; Joines, J. A.; Thoney, K. A., *J. Polym. Sci., Part B: Polym. Phys.* **2012,** *50*, 824.

[93] Darmanin, T.; de Givenchy, E. T.; Amigoni, S.; Guittard, F., *Adv. Mater.* **2013,** *25*, 1378.

[94] Scardino, A. J.; Zhang, H.; Cookson, D. J.; Lamb, R. N.; Nys, R. d., *Biofouling* **2009,** *25*, 757.

[95] Fadeeva, E.; Truong, V. K.; Stiesch, M.; Chichkov, B. N.; Crawford, R. J.; Wang, J.; Ivanova, E. P., *Langmuir* **2011,** *27*, 3012.

[96] Privett, B. J.; Youn, J.; Hong, S. A.; Lee, J.; Han, J.; Shin, J. H.; Schoenfisch, M. H., *Langmuir* **2011,** *27*, 9597.

[97] Zhang, P.; Lin, L.; Zang, D.; Guo, X.; Liu, M., *Small* **2017,** *13*, 1503334.

[98] Hwang, G. B.; Page, K.; Patir, A.; Nair, S. P.; Allan, E.; Parkin, I. P., *ACS Nano* **2018,** *12*, 6050.

[99] Moradi, S.; Hadjesfandiari, N.; Toosi, S. F.; Kizhakkedathu, J. N.; Hatzikiriakos, S. G., *ACS Appl. Mater. Interfaces* **2016,** *8*, 17631.

[100] Sun, T.; Tan, H.; Han, D.; Fu, Q.; Jiang, L., *Small* **2005,** *1*, 959.

[101] Zhao, J.; Song, L.; Yin, J.; Ming, W., *Chem. Commun.* **2013,** *49*, 9191.

[102] Movafaghi, S.; Leszczak, V.; Wang, W.; Sorkin, J. A.; Dasi, L. P.; Popat, K. C.; Kota, A. K., *Adv. Healthc. Mater.* **2017,** *6*.

[103] Li, Z.; Milionis, A.; Zheng, Y.; Yee, M.; Codispoti, L.; Tan, F.; Poulikakos, D.; Yap, C. H., *Nat. Commun.* **2019,** *10*, 5562.

[104] Mulay, S. R.; Herrmann, M.; Bilyy, R.; Gabibov, A.; Anders, H.-J., *Front. Immunol.* **2019,** *10*, 1.

[105] Ilinskaya, A. N.; Dobrovolskaia, M. A., *Nanomedicine* **2013,** *8*, 969.

[106] Bucala, R.; Kawakami, M.; Cerami, A., *Science* **1983,** *220*, 965.

[107] Ruzza, P.; Gatto, C.; Ragazzi, E.; Romano, M. R.; Honisch, C.; Tóthová, J. D. A., *ACS Omega* **2019,** *4*, 13481.

[108] Wong, T.-S.; Kang, S. H.; Tang, S. K. Y.; Smythe, E. J.; Hatton, B. D.; Grinthal, A.; Aizenberg, J., *Nature* **2011,** *477*, 443.

[109] Lafuma, A.; Quéré, D., *Europhys. Lett.* **2011,** *96*, 56001.

[110] Villegas, M.; Zhang, Y.; Abu Jarad, N.; Soleymani, L.; Didar, T. F., *ACS Nano* **2019,** *13*, 8517.

[111] Bohn, H. F.; Federle, W., *Proc. Natl. Acad. Sci. U. S. A.* **2004,** *101*, 14138.

[112] Bauer, U.; Paulin, M.; Robert, D.; Sutton, G. P., *Proc. Natl. Acad. Sci. U. S. A.* **2015,** *112*, 13384.

[113] Smith, J. D.; Dhiman, R.; Anand, S.; Reza-Garduno, E.; Cohen, R. E.; McKinley, G. H.; Varanasi, K. K., *Soft Matter* **2013,** *9*, 1772.

[114] Schellenberger, F.; Xie, J.; Encinas, N.; Hardy, A.; Klapper, M.; Papadopoulos, P.; Butt, H.-J.; Vollmer, D., *Soft Matter* **2015,** *11*, 7617.

[115] Semprebon, C.; McHale, G.; Kusumaatmaja, H., *Soft Matter* **2017,** *13*, 101.

[116] Keiser, A.; Keiser, L.; Clanet, C.; Quéré, D., *Soft Matter* **2017,** *13*, 6981.

[117] Leslie, D. C.; Waterhouse, A.; Berthet, J. B.; Valentin, T. M.; Watters, A. L.; Jain, A.; Kim, P.; Hatton, B. D.; Nedder, A.; Donovan, K.; Super, E. H.; Howell, C.; Johnson, C. P.; Vu, T. L.; Bolgen, D. E.; Rifai, S.; Hansen, A. R.; Aizenberg, M.; Super, M.; Aizenberg, J.; Ingber, D. E., *Nat. Biotechnol.* **2014,** *32*, 1134.

[118] Kim, P.; Kreder, M. J.; Alvarenga, J.; Aizenberg, J., *Nano Lett.* **2013,** *13*, 1793.

[119] Peppou-Chapman, S.; Hong, J. K.; Waterhouse, A.; Neto, C., *Chem. Soc. Rev.* **2020,** *49*, 3688.

[120] Kim, P.; Wong, T.-S.; Alvarenga, J.; Kreder, M. J.; Adorno-Martinez, W. E.; Aizenberg, J., *ACS Nano* **2012,** *6*, 6569.

[121] Sunny, S.; Vogel, N.; Howell, C.; Vu, T. L.; Aizenberg, J., *Adv. Funct. Mater.* **2014,** *24*, 6658.

[122] Dong, Z.; Schumann, M. F.; Hokkanen, M. J.; Chang, B.; Welle, A.; Zhou, Q.; Ras, R. H. A.; Xu, Z.; Wegener, M.; Levkin, P. A., *Adv. Mater.* **2018,** *30*, 1803890.

[123] Kreder, M. J.; Alvarenga, J.; Kim, P.; Aizenberg, J., *Nat. Rev. Mater.* **2016,** *1*, 15003.

[124] Rowthu, S.; Balic, E. E.; Hoffmann, P., *Nanotechnology* **2017,** *28*, 505605.

[125] Sett, S.; Yan, X.; Barac, G.; Bolton, L. W.; Miljkovic, N., *ACS Appl. Mater. Interfaces* **2017,** *9*, 36400.

[126] Preston, D. J.; Song, Y.; Lu, Z.; Antao, D. S.; Wang, E. N., *ACS Appl. Mater. Interfaces* **2017,** *9*, 42383.

[127] Howell, C.; Grinthal, A.; Sunny, S.; Aizenberg, M.; Aizenberg, J., *Adv. Mater.* **2018,** *30*, 1802724.

[128] Deng, R.; Shen, T.; Chen, H.; Lu, J.; Yang, H.-C.; Li, W., *J. Mater. Chem. A* **2020,** *8*, 7536.

[129] Li, J.; Ueda, E.; Paulssen, D.; Levkin, P. A., *Adv. Funct. Mater.* **2019,** *29*, 1802317.

[130] Xiao, L.; Li, J.; Mieszkin, S.; Di Fino, A.; Clare, A. S.; Callow, M. E.; Callow, J. A.; Grunze, M.; Rosenhahn, A.; Levkin, P. A., *ACS Appl. Mater. Interfaces* **2013,** *5*, 10074.

[131] Sunny, S.; Cheng, G.; Daniel, D.; Lo, P.; Ochoa, S.; Howell, C.; Vogel, N.; Majid, A.; Aizenberg, J., *Proc. Natl. Acad. Sci. U. S. A.* **2016,** *113*, 11676.

[132] Amini, S.; Kolle, S.; Petrone, L.; Ahanotu, O.; Sunny, S.; Sutanto, C. N.; Hoon, S.; Cohen, L.; Weaver, J. C.; Aizenberg, J.; Vogel, N.; Miserez, A., *Science* **2017,** *357*, 668.

[133] Adera, S.; Alvarenga, J.; Shneidman, A. V.; Zhang, C. T.; Davitt, A.; Aizenberg, J., *ACS Nano* **2020,** *14*, 8024.

[134] Kreder, M. J.; Daniel, D.; Tetreault, A.; Cao, Z.; Lemaire, B.; Timonen, J. V. I.; Aizenberg, J., *Phys. Rev. X* **2018,** *8*, 031053.

[135] Wexler, J. S.; Jacobi, I.; Stone, H. A., *Phys. Rev. Lett.* **2015,** *114*, 5.

[136] Howell, C.; Vu, T. L.; Johnson, C. P.; Hou, X.; Ahanotu, O.; Alvarenga, J.; Leslie, D. C.; Uzun, O.; Waterhouse, A.; Kim, P.; Super, M.; Aizenberg, M.; Ingber, D. E.; Aizenberg, J., *Chem. Mater.* **2015,** *27*, 1792.

[137] Howell, C.; Vu, T. L.; Lin, J. J.; Kolle, S.; Juthani, N.; Watson, E.; Weaver, J. C.; Alvarenga, J.; Aizenberg, J., *ACS Appl. Mater. Interfaces* **2014,** *6*, 13299.

[138] Yao, X.; Wu, S. W.; Chen, L.; Ju, J.; Gu, Z. D.; Liu, M. J.; Wang, J. J.; Jiang, L., *Angew. Chem. Int. Ed.* **2015,** *54*, 8975.

[139] Urata, C.; Dunderdale, G. J.; England, M. W.; Hozumi, A., *J. Mater. Chem. A* **2015,** *3*, 12626.

[140] Cui, J.; Daniel, D.; Grinthal, A.; Lin, K.; Aizenberg, J., *Nat. Mater.* **2015,** *14*, 790.

[141] Zhao, H.; Sun, Q.; Deng, X.; Cui, J., *Adv. Mater.* **2018,** *30*, 1802141.

[142] Le Bideau, J.; Viau, L.; Vioux, A., *Chem. Soc. Rev.* **2011,** *40*, 907.

[143] Lodge, T. P.; Ueki, T., *Acc. Chem. Res.* **2016,** *49*, 2107.

[144] Marr, P. C.; Marr, A. C., *Green Chem.* **2016,** *18*, 105.

[145] Rogers, R. D.; Seddon, K. R., *Science* **2003,** *302*, 792.

[146] Rogers, R. D.; Voth, G. A., *Acc. Chem. Res.* **2007,** *40*, 1077.

[147] Hayes, R.; Warr, G. G.; Atkin, R., *Chem. Rev.* **2015,** *115*, 6357.

[148] Dong, K.; Liu, X.; Dong, H.; Zhang, X.; Zhang, S., *Chem. Rev.* **2017,** *117*, 6636.

[149] Galiński, M.; Lewandowski, A.; Stępniak, I., *Electrochim. Acta* **2006,** *51*, 5567.

[150] Earle, M. J.; Seddon, K. R., *Pure Appl. Chem.* **2000,** *72*, 1391.

[151] Clarke, C. J.; Tu, W.-C.; Levers, O.; Bröhl, A.; Hallett, J. P., *Chem. Rev.* **2018,** *118*, 747.

[152] Tan, S. S. Y.; MacFarlane, D. R., Ionic Liquids in Biomass Processing. In *Ionic Liquids*, Kirchner, B., Ed. Springer Berlin Heidelberg: Berlin, Heidelberg, 2010; pp 311.

[153] Mahmood, H.; Moniruzzaman, M., *Biotechnol. J.* **2019,** *14*, 1900072.

[154] Ventura, S. P. M.; e Silva, F. A.; Quental, M. V.; Mondal, D.; Freire, M. G.; Coutinho, J. A. P., *Chem. Rev.* **2017,** *117*, 6984.

[155] Passos, H.; Freire, M. G.; Coutinho, J. A. P., *Green Chem.* **2014,** *16*, 4786.

[156] Lewandowski, A.; Świderska-Mocek, A., *J. Power Sources* **2009,** *194*, 601.

[157] Muñoz-Bonilla, A.; Fernández-García, M., *Eur. Polym. J.* **2018,** *105*, 135.

[158] Guan, J.; Wang, Y.; Wu, S.; Li, Y.; Li, J., *Biomacromolecules* **2017,** *18*, 4364.

[159] Ye, Q.; Gao, T.; Wan, F.; Yu, B.; Pei, X.; Zhou, F.; Xue, Q., *J. Mater. Chem.* **2012,** *22*, 13123.

[160] Zhao, L.; Li, Y.; Liu, Z.; Shimizu, H., *Chem. Mater.* **2010,** *22*, 5949.

[161] Zhao, L.; Li, Y.; Cao, X.; You, J.; Dong, W., *Nanotechnology* **2012,** *23*, 255702.

[162] Shang, N. G.; Papakonstantinou, P.; Sharma, S.; Lubarsky, G.; Li, M.; McNeill, D. W.; Quinn, A. J.; Zhou, W.; Blackley, R., *Chem. Commun.* **2012,** *48*, 1877.

[163] Matsumoto, M.; Saito, Y.; Park, C.; Fukushima, T.; Aida, T., *Nat. Chem.* **2015,** *7*, 730.

[164] Guan, J.; Xing, C.; Wang, Y.; Li, Y.; Li, J., *Compos. Sci. Technol.* **2017,** *138*, 98.

[165] MacFarlane, D. R.; Forsyth, M.; Howlett, P. C.; Kar, M.; Passerini, S.; Pringle, J. M.; Ohno, H.; Watanabe, M.; Yan, F.; Zheng, W.; Zhang, S.; Zhang, J., *Nat. Rev. Mater.* **2016,** *1*, 15005.

[166] Susan, M. A. B. H.; Kaneko, T.; Noda, A.; Watanabe, M., *J. Am. Chem. Soc.* **2005,** *127*, 4976.

[167] Rupp, B.; Schmuck, M.; Balducci, A.; Winter, M.; Kern, W., *Eur. Polym. J.* **2008,** *44*, 2986.

[168] Sinawang, G.; Kobayashi, Y.; Zheng, Y.; Takashima, Y.; Harada, A.; Yamaguchi, H., *Macromolecules* **2019,** *52*, 2932.

[169] Lei, Y.; Lodge, T. P., *Soft Matter* **2012,** *8*, 2110.

[170] Noro, A.; Matsushima, S.; He, X.; Hayashi, M.; Matsushita, Y., *Macromolecules* **2013,** *46*, 8304.

[171] Cai, M.; Liang, Y.; Zhou, F.; Liu, W., *J. Mater. Chem.* **2011,** *21*, 13399.

[172] Maršavelski, A.; Smrečki, V.; Vianello, R.; Žinić, M.; Moguš-Milanković, A.; Šantić, A., *Chem. Eur. J.* **2015,** *21*, 12121.

[173] He, Y.; Boswell, P. G.; Bühlmann, P.; Lodge, T. P., *J. Phys. Chem. B* **2007,** *111*, 4645.

[174] Ueki, T.; Nakamura, Y.; Usui, R.; Kitazawa, Y.; So, S.; Lodge, T. P.; Watanabe, M., *Angew. Chem. Int. Ed.* **2015,** *54*, 3018.

[175] Hall, C. C.; Zhou, C.; Danielsen, S. P. O.; Lodge, T. P., *Macromolecules* **2016,** *49*, 2298.

[176] Yeon, S.-H.; Kim, K.-S.; Choi, S.; Cha, J.-H.; Lee, H., *J. Phys. Chem. B* **2005,** *109*, 17928.

[177] Yasuda, T.; Nakamura, S.-i.; Honda, Y.; Kinugawa, K.; Lee, S.-Y.; Watanabe, M., *ACS Appl. Mater. Interfaces* **2012,** *4*, 1783.

[178] Ohno, H.; Yoshizawa, M.; Ogihara, W., *Electrochim. Acta* **2003,** *48*, 2079.

[179] Chen, X.; Put, B.; Sagara, A.; Gandrud, K.; Murata, M.; Steele, J. A.; Yabe, H.; Hantschel, T.; Roeffaers, M.; Tomiyama, M.; Arase, H.; Kaneko, Y.; Shimada, M.; Mees, M.; Vereecken, P. M., *Sci. Adv.* **2020,** *6*, eaav3400.

[180] Wang, P.; Zakeeruddin, S. M.; Comte, P.; Exnar, I.; Grätzel, M., *J. Am. Chem. Soc.* **2003,** *125*, 1166.

[181] Ueno, K., *Polym. J.* **2018,** *50*, 951.

[182] Huang, Y.; Takata, A.; Tsujii, Y.; Ohno, K., *Langmuir* **2017,** *33*, 7130.

[183] Ueno, K.; Hata, K.; Katakabe, T.; Kondoh, M.; Watanabe, M., *J. Phys. Chem. B* **2008,** *112*, 9013.

[184] Ueno, K.; Sano, Y.; Inaba, A.; Kondoh, M.; Watanabe, M., *J. Phys. Chem. B* **2010,** *114*, 13095.

[185] Kopeček, J., *Biomaterials* **2007,** *28*, 5185.

[186] Li, J.; Mooney, D. J., *Nat. Rev. Mater.* **2016,** *1*, 16071.

[187] Du, X.; Zhou, J.; Shi, J.; Xu, B., *Chem. Rev.* **2015,** *115*, 13165.

[188] Fan, H.; Gong, J. P., *Macromolecules* **2020,** *53*, 2769.

[189] Appel, E. A.; del Barrio, J.; Loh, X. J.; Scherman, O. A., *Chem. Soc. Rev.* **2012,** *41*, 6195.

[190] Peppas, N. A.; Hilt, J. Z.; Khademhosseini, A.; Langer, R., *Adv. Mater.* **2006,** *18*, 1345.

[191] Elkhoury, K.; Russell, C. S.; Sanchez-Gonzalez, L.; Mostafavi, A.; Williams, T. J.; Kahn, C.; Peppas, N. A.; Arab-Tehrany, E.; Tamayol, A., *Adv. Healthc. Mater.* **2019,** *8*, e1900506.

[192] Gu, Y.; Zhao, J.; Johnson, J. A., *Angew. Chem. Int. Ed.* **2020,** *59*, 5022.

[193] Zhou, C.; Hillmyer, M. A.; Lodge, T. P., *J. Am. Chem. Soc.* **2012,** *134*, 10365.

[194] Taribagil, R. R.; Hillmyer, M. A.; Lodge, T. P., *Macromolecules* **2010,** *43*, 5396.

[195] Ricardo, N. M. P. S.; Honorato, S. B.; Yang, Z.; Castelletto, V.; Hamley, I. W.; Yuan, X.-F.; Attwood, D.; Booth, C., *Langmuir* **2004,** *20*, 4272.

[196] Stauffer, S. R.; Peppast, N. A., *Polymer* **1992,** *33*, 3932.

[197] Ricciardi, R.; Auriemma, F.; De Rosa, C.; Lauprêtre, F., *Macromolecules* **2004,** *37*, 1921.

[198] Yuan, J.-J.; Jin, R.-H., *Langmuir* **2005,** *21*, 3136.

[199] Agrawal, S. K.; Sanabria-DeLong, N.; Tew, G. N.; Bhatia, S. R., *Macromolecules* **2008,** *41*, 1774.

[200] Lin, S.; Liu, J.; Liu, X.; Zhao, X., *Proc. Natl. Acad. Sci. U. S. A.* **2019,** *116*, 10244.

[201] Thoniyot, P.; Tan, M. J.; Karim, A. A.; Young, D. J.; Loh, X. J., *Adv. Sci.* **2015,** *2*, 1400010.

[202] Dannert, C.; Stokke, B. T.; Dias, R. S., *Polymers* **2019,** *11*.

[203] Clasky, A. J.; Watchorn, J. D.; Chen, P. Z.; Gu, F. X., *Acta Biomater.* **2021,** *122*, 1.

[204] Lavrador, P.; Esteves, M. R.; Gaspar, V. M.; Mano, J. F., *Adv. Funct. Mater.* **2021,** *31*, 2005941.

[205] Wang, C.; Flynn, N. T.; Langer, R., *Adv. Mater.* **2004,** *16*, 1074.

[206] Saravanan, P.; Padmanabha Raju, M.; Alam, S., *Mater. Chem. Phys.* **2007,** *103*, 278.

[207] Murthy, P. S. K.; Murali Mohan, Y.; Varaprasad, K.; Sreedhar, B.; Mohana Raju, K., *J. Colloid Interface Sci.* **2008,** *318*, 217.

[208] Xiang, Y.; Chen, D., *Eur. Polym. J.* **2007,** *43*, 4178.

[209] Varaprasad, K.; Siva Mohan Reddy, G.; Jayaramudu, J.; Sadiku, R.; Ramam, K.; Ray, S. S., *Biomater. Sci.* **2014,** *2*, 257.

[210] Zhao, X.; Ding, X.; Deng, Z.; Zheng, Z.; Peng, Y.; Tian, C.; Long, X., *New J. Chem.* **2006,** *30*, 915.

[211] Castaneda, L.; Valle, J.; Yang, N.; Pluskat, S.; Slowinska, K., *Biomacromolecules* **2008,** *9*, 3383.

[212] Skardal, A.; Zhang, J.; McCoard, L.; Oottamasathien, S.; Prestwich, G. D., *Adv. Mater.* **2010,** *22*, 4736.

[213] Haraguchi, K.; Takehisa, T., *Adv. Mater.* **2002,** *14*, 1120.

[214] Souza, G. R.; Christianson, D. R.; Staquicini, F. I.; Ozawa, M. G.; Snyder, E. Y.; Sidman, R. L.; Miller, J. H.; Arap, W.; Pasqualini, R., *Proc. Natl. Acad. Sci. U. S. A.* **2006,** *103*, 1215.

[215] Wang, Q.; Mynar, J. L.; Yoshida, M.; Lee, E.; Lee, M.; Okuro, K.; Kinbara, K.; Aida, T., *Nature* **2010,** *463*, 339.

[216] Wang, J.; Lin, L.; Cheng, Q.; Jiang, L., *Angew. Chem. Int. Ed.* **2012,** *51*, 4676.

[217] Appel, E. A.; Tibbitt, M. W.; Webber, M. J.; Mattix, B. A.; Veiseh, O.; Langer, R., *Nat. Commun.* **2015,** *6*, 6295.

[218] Li, Q.; Barrett, D. G.; Messersmith, P. B.; Holten-Andersen, N., *ACS Nano* **2016,** *10*, 1317.

[219] Pardo-Yissar, V.; Gabai, R.; Shipway, A. N.; Bourenko, T.; Willner, I., *Adv. Mater.* **2001,** *13*, 1320.

[220] Sheeney-Haj-Ichia, L.; Sharabi, G.; Willner, I., *Adv. Funct. Mater.* **2002,** *12*, 27.

[221] Guo; Hu, J.-S.; Liang, H.-P.; Wan, L.-J.; Bai, C.-L., *Chem. Mater.* **2003,** *15*, 4332.

[222] Mehrali, M.; Thakur, A.; Pennisi, C. P.; Talebian, S.; Arpanaei, A.; Nikkhah, M.; Dolatshahi-Pirouz, A., *Adv. Mater.* **2017,** *29*, 1603612.

[223] Cho, Y.; Borgens, R. B., *J. Biomed. Mater. Res. A* **2010,** *95A*, 510.

[224] Imaninezhad, M.; Pemberton, K.; Xu, F. L.; Kalinowski, K.; Bera, R.; Zustiak, S. P., *J. Neural Eng.* **2018,** *15*, 17.

[225] Zhou, Z.; Liu, X.; Wu, W.; Park, S.; Miller Ii, A. L.; Terzic, A.; Lu, L., *Biomater. Sci.* **2018,** *6*, 2375.

[226] Lee, S.-J.; Zhu, W.; Nowicki, M.; Lee, G.; Heo, D. N.; Kim, J.; Zuo, Y. Y.; Zhang, L. G., *J. Neural Eng.* **2018,** *15*, 016018.

[227] Sun, Y.; Liu, X.; George, M. N.; Park, S.; Gaihre, B.; Terzic, A.; Lu, L., *J. Biomed. Mater. Res. A* **2020**.

[228] Lee, J. H.; Lee, J. Y.; Yang, S. H.; Lee, E. J.; Kim, H. W., *Acta Biomater.* **2014,** *10*, 4425.

[229] Niu, Y.; Chen, X.; Yao, D.; Peng, G.; Liu, H.; Fan, Y., *J. Biomed. Mater. Res. A* **2018,** *106*, 2973.

[230] Shin, J.; Choi, E. J.; Cho, J. H.; Cho, A.-N.; Jin, Y.; Yang, K.; Song, C.; Cho, S.-W., *Biomacromolecules* **2017,** *18*, 3060.

[231] Wu, S.; Duan, B.; Lu, A.; Wang, Y.; Ye, Q.; Zhang, L., *Carbohydr. Polym.* **2017,** *174*, 830.

[232] Shrestha, S.; Shrestha, B. K.; Lee, J.; Joong, O. K.; Kim, B.-S.; Park, C. H.; Kim, C. S., *Mater. Sci. Eng. C Mater. Biol. Appl.* **2019,** *102*, 511.

[233] Homaeigohar, S.; Tsai, T.-Y.; Young, T.-H.; Yang, H. J.; Ji, Y.-R., *Carbohydr. Polym.* **2019,** *224*, 115112.

[234] Pampaloni, N. P.; Lottner, M.; Giugliano, M.; Matruglio, A.; D'Amico, F.; Prato, M.; Garrido, J. A.; Ballerini, L.; Scaini, D., *Nat. Nanotechnol.* **2018,** *13*, 755.

[235] Minsky, M., *Scanning* **1988,** *10*, 128.

[236] Paddock, S. W., *Biotechniques* **1999,** *27*, 992.

[237] Paddock, S. W., *Mol. Biotechnol.* **2000,** *16*, 127.

[238] Pawley, J. B., Fundamental Limits in Confocal Microscopy. In *Handbook of Biological Confocal Microscopy*, Pawley, J. B., Ed. Springer US: Boston, MA, 2006; pp 20.

[239] Koynov, K.; Butt, H.-J., *Opin. Colloid Interface Sci.* **2012,** *17*, 377.

[240] Giessibl, F. J., *Rev. Mod. Phys.* **2003,** *75*, 949.

[241] Alessandrini, A.; Facci, P., *Meas. Sci. Technol.* **2005,** *16*, R65.

[242] Xu, K.; Sun, W.; Shao, Y.; Wei, F.; Zhang, X.; Wang, W.; Li, P., *Nanotechnol. Rev.* **2018,** *7*, 605.

[243] Menard, K. P.; Menard, N., Dynamic Mechanical Analysis. In *Encyclopedia of Analytical Chemistry*, 2017; pp 1.

[244] Tschoegl, N. W., *The Phenomenological Theory of Linear Viscoelastic Behavior: An Introduction*. Springer Science & Business Media: 2012.

[245] Ye, L.; Chen, F.; Liu, J.; Gao, A.; Kircher, G.; Liu, W.; Kappl, M.; Wegner, S.; Butt, H.-J.; Steffen, W., *Macromol. Rapid Commun.* **2019,** *40*, 1900395.

[246] Armbruster, C. R.; Parsek, M. R., *Proc. Natl. Acad. Sci. U. S. A.* **2018,** *115*, 4317.

[247] Oliveira, N. M.; Martinez-Garcia, E.; Xavier, J.; Durham, W. M.; Kolter, R.; Kim, W.; Foster, K. R., *PLoS Biol.* **2015,** *13*, e1002191.

[248] Li, Z.; Lee, D.; Sheng, X.; Cohen, R. E.; Rubner, M. F., *Langmuir* **2006,** *22*, 9820.

[249] El Habnouni, S.; Lavigne, J. P.; Darcos, V.; Porsio, B.; Garric, X.; Coudane, J.; Nottelet, B., *Acta Biomater.* **2013,** *9*, 7709.

[250] Asri, L. A. T. W.; Crismaru, M.; Roest, S.; Chen, Y.; Ivashenko, O.; Rudolf, P.; Tiller, J. C.; Mei, H. C. v. d.; Loontjens, T. J. A.; Busscher, H. J., *Adv. Funct. Mater.* **2014,** *24*, 346.

[251] Kuroki, H.; Tokarev, I.; Nykypanchuk, D.; Zhulina, E.; Minko, S., *Adv. Funct. Mater.* **2013,** *23*, 4593.

[252] Palza, H., *Int. J. Mol. Sci.* **2015,** *16*.

[253] Bos, R.; van der Mei, H. C.; Gold, J.; Busscher, H. J., *FEMS Microbiol. Lett.* **2000,** *189*, 311.

[254] Neu, T. R., *Microbiol. Rev.* **1996,** *60*, 151.

[255] Gristina, A. G., *Science* **1987,** *237*, 1588.

[256] Liu, S. Q.; Yang, C.; Huang, Y.; Ding, X.; Li, Y.; Fan, W. M.; Hedrick, J. L.; Yang, Y.-Y., *Adv. Mater.* **2012,** *24*, 6484.

[257] Kingshott, P.; Wei, J.; Bagge-Ravn, D.; Gadegaard, N.; Gram, L., *Langmuir* **2003,** *19*, 6912.

[258] Ulbricht, J.; Jordan, R.; Luxenhofer, R., *Biomaterials* **2014,** *35*, 4848.

[259] Zhang, X.; Wang, L.; Levänen, E., *RSC Adv.* **2013,** *3*, 12003.

[260] Egorova, K. S.; Gordeev, E. G.; Ananikov, V. P., *Chem. Rev.* **2017,** *117*, 7132.

[261] Frade, R. F. M.; Rosatella, A. A.; Marques, C. S.; Branco, L. C.; Kulkarni, P. S.; Mateus, N. M. M.; Afonso, C. A. M.; Duarte, C. M. M., *Green Chem.* **2009,** *11*, 1660.

[262] Zheng, Z.; Xu, Q.; Guo, J.; Qin, J.; Mao, H.; Wang, B.; Yan, F., *ACS Appl. Mater. Interfaces* **2016,** *8*, 12684.

[263] Dong, Y.-S.; Xiong, X.-H.; Lu, X.-W.; Wu, Z.-Q.; Chen, H., *J. Mater. Chem. B* **2016,** *4*, 6111.

[264] Miranda, D. F.; Urata, C.; Masheder, B.; Dunderdale, G. J.; Yagihashi, M.; Hozumi, A., *APL Mater.* **2014,** *2*, 6.

[265] Galvan, Y.; Phillips, K. R.; Haumann, M.; Wasserscheid, P.; Zarraga, R.; Vogel, N., *Langmuir* **2018,** *34*, 6894.

[266] Bradley, A. E.; Hardacre, C.; Holbrey, J. D.; Johnston, S.; McMath, S. E. J.; Nieuwenhuyzen, M., *Chem. Mater.* **2002,** *14*, 629.

[267] Dunstan, T. D. J.; Caja, J., *ECS Trans.* **2007,** *3*, 21.

[268] Kunze, M.; Jeong, S.; Paillard, E.; Winter, M.; Passerini, S., *J. Phys. Chem. C.* **2010,** *114*, 12364.

[269] Ye, L.; Ye, C.; Xie, K.; Shi, X.; You, J.; Li, Y., *Macromolecules* **2015,** *48*, 8515.

[270] Schultz, J. M., *Front. Chem. China* **2010,** *5*, 262.

[271] Jansen, J. C.; Friess, K.; Clarizia, G.; Schauer, J.; Izak, P., *Macromolecules* **2011,** *44*, 39.

[272] Lee, K. H.; Kang, M. S.; Zhang, S.; Gu, Y.; Lodge, T. P.; Frisbie, C. D., *Adv. Mater.* **2012,** *24*, 4457.

[273] Guan, J.; Li, Y.; Li, J., *Ind. Eng. Chem. Res.* **2017,** *56*, 12456.

[274] Guan, J.; Shen, J.; Chen, X.; Wang, H.; Chen, Q.; Li, J.; Li, Y., *Macromolecules* **2019,** *52*, 385.

[275] Teisala, H.; Schönecker, C.; Kaltbeitzel, A.; Steffen, W.; Butt, H.-J.; Vollmer, D., *Phys. Rev. Fluids* **2018,** *3*, 084002.

[276] H., N. S.; G., T. A., *J. Polym. Sci., Polym. Phys. Ed.* **1980,** *18*, 511.

[277] Wang, Y.; Yao, X.; Wu, S.; Li, Q.; Lv, J.; Wang, J.; Jiang, L., *Adv. Mater.* **2017,** *29*.

[278] Liu, J.; Ye, L.; Sun, Y.; Hu, M.; Chen, F.; Wegner, S.; Mailänder, V.; Steffen, W.; Kappl, M.; Butt, H.-J., *Adv. Mater.* **2020,** *32*, 1908008.

[279] Boateng, J.; Catanzano, O., *J. Pharm. Sci.* **2015,** *104*, 3653.

[280] Fry, D. E.; Pearlstein, L.; Fulton, R. L.; Polk, H. C., Jr., *Arch. Surg.* **1980,** *115*, 136.

[281] Johnson, D.; Bates, S.; Nukalo, S.; Staub, A.; Hines, A.; Leishman, T.; Michel, J.; Sikes, D.; Gegel, B.; Burgert, J., *Ann. Med. Surg.* **2014,** *3*, 21.

[282] Quebbeman, E. J.; Telford, G. L.; Hubbard, S.; Wadsworth, K.; Hardman, B.; Goodman, H.; Gottlieb, M. S., *Ann. Surg.* **1991,** *214*, 614.

[283] Beltrami, E. M.; Williams, I. T.; Shapiro, C. N.; Chamberland, M. E., *Clin. Microbiol. Rev.* **2000,** *13*, 385.

[284] Hall, J. R., *Anesth. Analg.* **1994,** *78*, 1136.

[285] Torabinejad, M.; Higa, R. K.; McKendry, D. J.; Ford, T. R. P., *J. Endod.* **1994,** *20*, 159.

[286] Sun, G.; Xu, X.; Bickett, J. R.; Williams, J. F., *Ind. Eng. Chem. Res.* **2001,** *40*, 1016.

[287] Semler, H. J., *Radiology* **1985,** *154*, 234.

[288] Dong, Y.; Zheng, Y.; Zhang, K.; Yao, Y.; Wang, L.; Li, X.; Yu, J.; Ding, B., *Adv. Fiber Mater.* **2020,** *2*, 212.

[289] Choi Anna, L.; Sun, G.; Zhang, Y.; Grandjean, P., *Environ. Health Perspect.* **2012,** *120*, 1362.

[290] Schellenberger, S.; Hill, P. J.; Levenstam, O.; Gillgard, P.; Cousins, I. T.; Taylor, M.; Blackburn, R. S., *J. Clean. Prod.* **2019,** *217*, 134.

[291] Dalu, A.; Blaydes, B. S.; Lomax, L. G.; Delclos, K. B., *Biomaterials* **2000,** *21*, 1947.

[292] Daniels, A., *Swiss Med. Wkly.* **2012,** *142*.

[293] Shiraishi, K.; Koseki, H.; Tsurumoto, T.; Baba, K.; Naito, M.; Nakayama, K.; Shindo, H., *Surf. Interface Anal.* **2009,** *41*, 17.

[294] Ma, M.; Kazemzadeh-Narbat, M.; Hui, Y.; Lu, S.; Ding, C.; Chen, D. D.; Hancock, R. E.; Wang, R., *J. Biomed. Mater. Res. A* **2012,** *100*, 278.

[295] Cui, C.; Liu, H.; Li, Y.; Sun, J.; Wang, R.; Liu, S.; Greer, A. L., *Mater. Lett.* **2005,** *59*, 3144.

[296] Khorasani, M.; Mirzadeh, H.; Sammes, P., *Radiat. Phys. Chem.* **1999,** *55*, 685.

[297] Fujishima, A.; Rao, T. N.; Tryk, D. A., *J. Photochem. Photobiol. C* **2000,** *1*, 1.

[298] Huang, Z.; Maness, P.-C.; Blake, D. M.; Wolfrum, E. J.; Smolinski, S. L.; Jacoby, W. A., *J. Photochem. Photobiol. A* **2000,** *130*, 163.

[299] Cortese, B.; D'Amone, S.; Manca, M.; Viola, I.; Cingolani, R.; Gigli, G., *Langmuir* **2008,** *24*, 2712.

[300] Jin, M.; Feng, X.; Xi, J.; Zhai, J.; Cho, K.; Feng, L.; Jiang, L., *Macromol. Rapid Commun.* **2005,** *26*, 1805.

[301] Wooh, S.; Encinas, N.; Vollmer, D.; Butt, H.-J., *Adv. Mater.* **2017**, 1604637.

[302] Wooh, S.; Butt, H. J., *Angew. Chem. Int. Ed.* **2017,** *56*, 4965.

[303] Cheng, D. F.; Urata, C.; Yagihashi, M.; Hozumi, A., *Angew. Chem. Int. Ed.* **2012,** *51*, 2956.

[304] Timonen, J. V. I.; Latikka, M.; Ikkala, O.; Ras, R. H. A., *Nat. Commun.* **2013,** *4*, 2398.

[305] Sheng, X.; Liu, Z.; Zeng, R.; Chen, L.; Feng, X.; Jiang, L., *J. Am. Chem. Soc.* **2017,** *139*, 12402.

[306] Li, J.; Chen, G.; Zhu, Y.; Liang, Z.; Pei, A.; Wu, C.-L.; Wang, H.; Lee, H. R.; Liu, K.; Chu, S.; Cui, Y., *Nat. Catal.* **2018,** *1*, 592.

[307] Lima, A. C.; Mano, J. F., *Nanomedicine* **2015,** *10*, 103.

[308] Lima, A. C.; Mano, J. F., *Nanomedicine* **2015,** *10*, 271.

[309] Hrnčíř, E.; Rosina, J., *Physiol. Res.* **1997,** *46*, 319.

[310] Rosina, J.; Kvasnak, E.; Suta, D.; Kolarova, H.; Malek, J.; Krajci, L., *Physiol. Res.* **2007,** *56*, S93.

[311] Gordillo, G. M.; Sen, C. K., *Am. J. Surg.* **2003,** *186*, 259.

[312] Ye, L.; Ji, H.; Liu, J.; Tu, C.-H.; Kappl, M.; Koynov, K.; Vogt, J.; Butt, H.-J., *Adv. Mater.* **2021**, DOI:10.1002/adma.202102981.

[313] Houshyar, S.; Bhattacharyya, A.; Shanks, R., *ACS Chem. Neurosci.* **2019,** *10*, 3349.

[314] Steel, E. M.; Sundararaghavan, H. G., Electrically Conductive Materials for Nerve Regeneration. In *Neural Engineering: From Advanced Biomaterials to 3D Fabrication Techniques*, Zhang, L. G.; Kaplan, D. L., Eds. Springer International Publishing: Cham, 2016; pp 145.

[315] Farrukh, A.; Zhao, S.; del Campo, A., *Front. Mater.* **2018,** *5*, 62.

[316] Fabbro, A.; Prato, M.; Ballerini, L., *Adv. Drug Del. Rev.* **2013,** *65*, 2034.

[317] Oprych, K. M.; Whitby, R. L.; Mikhalovsky, S. V.; Tomlins, P.; Adu, J., *Adv. Healthc. Mater.* **2016,** *5*, 1253.

[318] Mattson, M. P.; Haddon, R. C.; Rao, A. M., *J. Mol. Neurosci.* **2000,** *14*, 175.

[319] Hu, H.; Ni, Y.; Montana, V.; Haddon, R. C.; Parpura, V., *Nano Lett.* **2004,** *4*, 507.

[320] Chao, T. I.; Xiang, S.; Lipstate, J. F.; Wang, C.; Lu, J., *Adv. Mater.* **2010,** *22*, 3542.

[321] Chen, Y. S.; Hsiue, G. H., *Biomaterials* **2013,** *34*, 4936.

[322] Mazzatenta, A.; Giugliano, M.; Campidelli, S.; Gambazzi, L.; Businaro, L.; Markram, H.; Prato, M.; Ballerini, L., *J. Neurosci.* **2007,** *27*, 6931.

[323] Tang, M.; Song, Q.; Li, N.; Jiang, Z.; Huang, R.; Cheng, G., *Biomaterials* **2013,** *34*, 6402.

[324] Capasso, A.; Rodrigues, J.; Moschetta, M.; Buonocore, F.; Faggio, G.; Messina, G.; Kim, M. J.; Kwon, J.; Placidi, E.; Benfenati, F.; Bramini, M.; Lee, G.-H.; Lisi, N., *Adv. Funct. Mater.* **2021,** *31*, 2005300.

[325] Hu, X.; Wang, X.; Xu, Y.; Li, L.; Liu, J.; He, Y.; Zou, Y.; Yu, L.; Qiu, X.; Guo, J., *Adv. Healthc. Mater.* **2020,** *9*, e1901570.

[326] Liedtke, W.; Yeo, M.; Zhang, H.; Wang, Y.; Gignac, M.; Miller, S.; Berglund, K.; Liu, J., *Small* **2013,** *9*, 1066.

[327] Sankaran, S.; Becker, J.; Wittmann, C.; del Campo, A., *Small* **2019,** *15*, 1804717.

[328] Jung, I. Y.; Kim, J. S.; Choi, B. R.; Lee, K.; Lee, H., *Adv. Healthc. Mater.* **2017,** *6*, 1601475.

[329] Villiou, M.; Paez, J. I.; del Campo, A., *ACS Appl. Mater. Interfaces* **2020,** *12*, 37862.

[330] Jia, Z.; Gong, J.; Zeng, Y.; Ran, J.; Liu, J.; Wang, K.; Xie, C.; Lu, X.; Wang, J., *Adv. Funct. Mater.* **2021,** *31*, 2010461.

[331] Koppes, A. N.; Keating, K. W.; McGregor, A. L.; Koppes, R. A.; Kearns, K. R.; Ziemba, A. M.; McKay, C. A.; Zuidema, J. M.; Rivet, C. J.; Gilbert, R. J.; Thompson, D. M., *Acta Biomater.* **2016,** *39*, 34.

[332] Wang, L.; Wu, Y.; Hu, T.; Ma, P. X.; Guo, B., *Acta Biomater.* **2019,** *96*, 175.

[333] Hasanzadeh, E.; Ebrahimi-Barough, S.; Mirzaei, E.; Azami, M.; Tavangar, S. M.; Mahmoodi, N.; Basiri, A.; Ai, J., *J. Biomed. Mater. Res. A* **2019,** *107*, 802.

[334] Ramer, L. M.; Ramer, M. S.; Bradbury, E. J., *Lancet Neurol.* **2014,** *13*, 1241.

[335] Vogt, J.; Kirischuk, S.; Unichenko, P.; Schlüter, L.; Pelosi, A.; Endle, H.; Yang, J.-W.; Schmarowski, N.; Cheng, J.; Thalman, C.; Strauss, U.; Prokudin, A.; Bharati, B. S.; Aoki, J.; Chun, J.; Lutz, B.; Luhmann, H. J.; Nitsch, R., *Cereb. Cortex* **2017,** *27*, 131.

[336] Winkelmann, A.; Maggio, N.; Eller, J.; Caliskan, G.; Semtner, M.; Häussler, U.; Jüttner, R.; Dugladze, T.; Smolinsky, B.; Kowalczyk, S.; Chronowska, E.; Schwarz, G.; Rathjen, F. G.; Rechavi, G.; Haas, C. A.; Kulik, A.; Gloveli, T.; Heinemann, U.; Meier, J. C., *J. Clin. Invest.* **2014,** *124*, 696.

[337] Nelson, Sacha B.; Valakh, V., *Neuron* **2015,** *87*, 684.

[338] Turrigiano, G. G.; Nelson, S. B., *Nat. Rev. Neurosci.* **2004,** *5*, 97.

[339] Gomez, T. M.; Spitzer, N. C., *Nature* **1999,** *397*, 350.

[340] Longair, M. H.; Baker, D. A.; Armstrong, J. D., *Bioinformatics* **2011,** *27*, 2453.

[341] Ferreira, T. A.; Blackman, A. V.; Oyrer, J.; Jayabal, S.; Chung, A. J.; Watt, A. J.; Sjöström, P. J.; van Meyel, D. J., *Nat. Methods* **2014,** *11*, 982.

[342] Fukushima, T.; Kosaka, A.; Ishimura, Y.; Yamamoto, T.; Takigawa, T.; Ishii, N.; Aida, T., *Science* **2003,** *300*, 2072.

[343] Lee, J.; Aida, T., *Chem. Commun.* **2011,** *47*, 6757.

[344] Fdz De Anastro, A.; Porcarelli, L.; Hilder, M.; Berlanga, C.; Galceran, M.; Howlett, P.; Forsyth, M.; Mecerreyes, D., *ACS Appl. Energy Mater.* **2019,** *2*, 6960.

[345] Chaudhuri, O.; Cooper-White, J.; Janmey, P. A.; Mooney, D. J.; Shenoy, V. B., *Nature* **2020,** *584*, 535.

[346] Guilak, F.; Cohen, D. M.; Estes, B. T.; Gimble, J. M.; Liedtke, W.; Chen, C. S., *Cell Stem Cell* **2009,** *5*, 17.

[347] Shin, S. R.; Bae, H.; Cha, J. M.; Mun, J. Y.; Chen, Y.-C.; Tekin, H.; Shin, H.; Farshchi, S.; Dokmeci, M. R.; Tang, S.; Khademhosseini, A., *ACS Nano* **2012,** *6*, 362.

[348] Khademhosseini, A.; Yeh, J.; Jon, S.; Eng, G.; Suh, K. Y.; Burdick, J. A.; Langer, R., *Lab Chip* **2004,** *4*, 425.

[349] Shao, H.; Li, T.; Zhu, R.; Xu, X.; Yu, J.; Chen, S.; Song, L.; Ramakrishna, S.; Lei, Z.; Ruan, Y.; He, L., *Biomaterials* **2018,** *175*, 93.

[350] Convertino, D.; Fabbri, F.; Mishra, N.; Mainardi, M.; Cappello, V.; Testa, G.; Capsoni, S.; Albertazzi, L.; Luin, S.; Marchetti, L.; Coletti, C., *Nano Lett.* **2020,** *20*, 3633.

[351] Liu, X.; Huai, J.; Endle, H.; Schlüter, L.; Fan, W.; Li, Y.; Richers, S.; Yurugi, H.; Rajalingam, K.; Ji, H.; Cheng, H.; Rister, B.; Horta, G.; Baumgart, J.; Berger, H.; Laube, G.; Schmitt, U.; Schmeisser, M. J.; Boeckers, T. M.; Tenzer, S.; Vlachos, A.; Deller, T.; Nitsch, R.; Vogt, J., *Dev. Cell* **2016,** *38*, 275.

[352] Teo, B. K. K.; Wong, S. T.; Lim, C. K.; Kung, T. Y. S.; Yap, C. H.; Ramagopal, Y.; Romer, L. H.; Yim, E. K. F., *ACS Nano* **2013,** *7*, 4785.

[353] Ivankovic-Dikic, I.; Grönroos, E.; Blaukat, A.; Barth, B.-U.; Dikic, I., *Nat. Cell Biol.* **2000,** *2*, 574.

[354] Ceto, S.; Sekiguchi, K. J.; Takashima, Y.; Nimmerjahn, A.; Tuszynski, M. H., *Cell Stem Cell* **2020,** *27*, 430.

[355] Fischer, I.; Dulin, J. N.; Lane, M. A., *Nat. Rev. Neurosci.* **2020,** *21*, 366.

[356] Obernier, K.; Alvarez-Buylla, A., *Development* **2019,** *146*.

[357] Lim, D. A.; Alvarez-Buylla, A., *Cold Spring Harb. Perspect. Biol.* **2016,** *8*.

[358] Clarke, D. L.; Johansson, C. B.; Wilbertz, J.; Veress, B.; Nilsson, E.; Karlström, H.; Lendahl, U.; Frisén, J., *Science* **2000,** *288*, 1660.

[359] Alvarez, V. A.; Sabatini, B. L., *Annu. Rev. Neurosci.* **2007,** *30*, 79.

[360] Kasai, H.; Fukuda, M.; Watanabe, S.; Hayashi-Takagi, A.; Noguchi, J., *Trends Neurosci.* **2010,** *33*, 121.

[361] Matsuzaki, M.; Honkura, N.; Ellis-Davies, G. C.; Kasai, H., *Nature* **2004,** *429*, 761.

[362] McKinney, R. A., *J. Physiol.* **2010,** *588*, 107.

[363] Altman, J.; Bayer, S. A., *J. Comp. Neurol.* **1990,** *301*, 343.

[364] Altman, J.; Bayer, S. A., *J. Comp. Neurol.* **1990,** *301*, 325.

[365] Grienberger, C.; Konnerth, A., *Neuron* **2012,** *73*, 862.

[366] Bacci, A.; Verderio, C.; Pravettoni, E.; Matteoli, M., *Eur. J. Neurosci.* **1999,** *11*, 389.

[367] Murphy, T. H.; Blatter, L. A.; Wier, W. G.; Baraban, J. M., *J. Neurosci.* **1992,** *12*, 4834.

[368] Yang, Y.-M.; Wang, L.-Y., *J. Neurosci.* **2006,** *26*, 5698.

Scientific Contributions

Related to the Ph.D. thesis:

[1] **L. Ye**, H. Ji., J. Liu, C.-H. Tu, M. Kappl, K. Koynov*, J. Vogt*, H.-J. Butt. Carbon Nanotube-Hydrogel Composites Facilitate Neuronal Differentiation While Maintaining Homeostasis of Network Activity. *Adv. Mater*. **2021***,* DOI:10.1002/adma.202102981.

[2] J. Liu, **L. Ye**, Y. Sun, M. Hu, F. Chen, S. Wegner, V. Mailänder, W. Steffen*, M. Kappl, H.-J. Butt*. Elastic Superhydrophobic and Photocatalytic Active Films Used as Blood Repellent Dressing. *Adv. Mater*. **2020**, *32*, 1908008.

[3] **L. Ye**, F. Chen, J. Liu, A. Gao, G. Kircher, W. Liu, M. Kappl, S. Wegner, H.-J. Butt, W. Steffen*. Responsive Ionogel Surface with Renewable Antibiofouling Properties. *Macromol. Rapid Commun*. **2019**, *40*, 1900395.

Others:

[1] A. Gao, J. Liu*, **L. Ye**, C. Schönecker, M. Kappl, H.-J. Butt, W. Steffen*. Control of Droplet Evaporation on Oil-Coated Surfaces for the Synthesis of Asymmetric Supraparticles. *Langmuir* **2019**, *35*, 14042.

[2] K. Xie, J. Shen, **L. Ye**, Z. Liu, Y. Li*. Increased gt Conformer Contents of PLLA Molecular Chains Induced by Li-TFSI in Melt: Another Route to Promote PLLA Crystallization. *Macromolecules* **2019**, *52*, 7065.

[3] J. Liu, **L. Ye**, S. Wooh, M. Kappl, W. Steffen*, H.-J. Butt*. Optimizing Hydrophobicity and Photocatalytic Activity of PDMS-Coated Titanium Dioxide. *ACS Appl. Mater. Interfaces* **2019**, *11*, 27422.

[4] J. Schultze, A. Vagias*, **L. Ye**, E. Prantl, V. Breising, A. Best, K. Koynov*, C. M. Marques*, H.-J. Butt. Preparation of Monodisperse Giant Unilamellar Anchored Vesicles using Micropatterned Hydrogel Substrates. *ACS Omega* **2019**, *4*, 9393.

[5] Z. Li, J. Shen, **L. Ye**, K. Xie, J. You*, Y. Li*. Reversible Transition Between Adhesive and Antiadhesive Performances by Stretching/Recovery on Superhydrophobic TPU/CNTs Composite Membrane Surface. *Appl. Surf. Sci.* **2019**, *471*, 900.

[6] Q. Jiao, J. Shen, **L. Ye**, Y. Li*, H. Chen. Poly(oxymethylene)/Poly(butylene succinate) Blends: Miscibility, Crystallization Behaviors and Mechanical Properties. *Polymer* **2019**, *167*, 40.

[7] J. Shen, **L. Ye**, K. Xie, Z. Li, Q. Jiao, Z. Chen, Y. Li*. Unexpected Brittleness: Does the Major Component in Binary Polymer Blends Always Make Sense? *Polymer* **2019**, *167*, 40.

[8] C. Ye, J. Zhao, **L. Ye**, Z. Jiang, J. You, Y. Li*. Precise Inter-Lamellar/Inter-fibrillar Localization and Consequent Fabrication of Porous Membranes with Crystallization-Modulated Pore-Size. *Polymer* **2018**, *142*, 48.

[9] **L. Ye**, J. Shen, K. Xie, Z. Li, Y. Li* Replicated Banded Spherulite: Microscopic Lamellar-Assembly of Poly(L-lactic acid) Crystals in the Poly(oxymethylene) Crystal Framework. *Chin. J. Polym. Sci.* **2018**, *36*, 385.

[10] Z. Li, **L. Ye**, J. Shen, K. Xie, Y. Li*. Strain-Gauge Sensoring Composite Films with Self-Restoring Water-Pepellent Properties for Monitoring Human Movements. *Compos. Commun*. **2018**, *7*, 23.

[11] J. Guan, Y. Wang, C. Xing, **L. Ye**, Y. Li, J. Li*. Semicrystalline Polymer Binary-Phase Structure Templated Quasi-Block Graft Copolymers. *J. Phys. Chem. B* **2017**, *12*, 7508.

[12] **L. Ye**, J. Guan, Z. Li, J. Zhao, C. Ye, J. You, Y. Li*. Fabrication of Superhydrophobic Surfaces with Controllable Electrical Conductivity and Water-Adhesion. *Langmuir* **2017**, *33*, 1368.

[13] **L. Ye**, C. Ye, K. Xie, X. Shi, J. You, Y. Li*. Morphologies and Crystallization Behaviors in Melt-Miscible Crystalline/Crystalline Blends with Close Melting Temperatures but Different Crystallization Kinetics. *Macromolecules* **2015**, *48*, 8515

[14] K. Lu, **L. Ye**, Q. Liang, Y. Li*. Selectively Located Aluminum Hydroxide in Rubber Phase in a TPV: Towards to a Halogen-Free Flame Retardant Thermoplastic Elastomer with Ultrahigh Flexibility. *Polym. Compos.* **2015,** *36*, 1258.

[15] **L. Ye**, C. Ye, X. Shi, H. Zhao, K. Xie, D. Chen, Y. Li*. Block-assembling: A New Strategy for Fabricating Conductive Nanoporous Materials from Nanocomposites based on a Melt-Miscible Crystalline/Crystalline Blend and MWCNTs. *J. Mater. Chem. C* **2015,** *3*, 8510

[16] **L. Ye**, C. Ye, X. Shi, H. Wang, H. Zhao, Xi. Cao, J. You, Y. Li*, Y. Liang. Nanohybrid Polymeric Nucleating Agents: In Situ Decorated Carbon Nanotubes and Serial Nucleation Behaviors in a Melt-Miscible Crystalline/Crystalline Blend. *Macromol. Chem. Phys.* **2015**, *216*, 1801.

[17] **L. Ye**, X. Shi, C. Ye, Z. Chen, M. Zeng, J. You, Y. Li*. Crystallization-Modulated Nanoporous Polymeric Materials with Hierarchical Patterned Surfaces and 3D Interpenetrated Internal Channels. *ACS Appl. Mater. Interfaces* **2015,** *7*, 6946.

[18] **L. Ye**, J. Qiu, T. Wu, X. Shi, Y. Li*. Banded Spherulite Templated Three-Dimensional Interpenetrated Nanoporous Materials. *RSC Adv.* **2014,** *4*, 43351.